NTNU

Norwegian University of
Science and Technology

Introduction of rhenium into porous supports

Joakim Tafjord

Chemistry
Submission date: May 2017
Supervisor: Karina Mathisen, IKJ

Norwegian University of Science and Technology
Department of Chemistry

Acknowledgements

The work of this thesis was carried out at the Department of Chemistry, Norwegian University of Science and Technology (NTNU). I would like to thank the staff of the Swiss-Norwegian Beamlines (SNBL) at the European Synchrotron Radiation Facility (ESRF) for their assistance during my stay, and Sparebanken Midt-Norges gavefond til Norges teknisk-naturvitenskapelige universitet for economic coverage of my travel expenses. Thanks to Kristin Høydalsvik Wells and Magnus Rotan for assisting me with XRD, Elin Harboe Albertsen with surface area measurements and Syverin Lierhagen for doing the ICP-MS analysis.

My biggest thanks goes to my supervisor Karina Mathisen for her fantastic guidance and support. Thankfully she kept my spirits up, especially when rhenium was giving me headaches. Post.doc Tina Kristiansen Voss and the Ph.D candidates Stian Forselv, Karsten Kirste and Guro Sørli has always been of great help when theoretical and technical aid was required, thank you. Both former and current members of the structural chemistry group have made these two years very entertaining, with weekly group meetings, social gatherings or simply by singing one-hit wonders form the 90's in the lab. Thank you all.

Thanks to my friends for their support and help. Especially Sondre, who has been my study partner in crime since day one. My parents deserve much gratitude for always believing in me, and showing that they are proud of me no matter what. And last, but not least, thanks to my dear Stine for always pushing me and making me believe I can do anything I set my mind to.

Sammendrag

Formålet med denne masteroppgaven var å syntetisere porøse katalysatorer som inneholder nanopartikler av metallisk rhenium. Hovedmålene var å introdusere rhenium i porene til porøse bærerer på en kontrollert måte og evaluere hvordan forskjellige poresystemer påvirker den resulterende partikkelstørrelsen til rhenium. De porøse bærerene som ble syntetisert i denne oppgaven var SAPO-34, AlPO-34, AlPO-5, SAPO-5 og SBA-15. Nye metoder for å syntetisere AlPO-34 uten flussyre ble også forsøkt, der komposisjonen av organiske templater og krystallisasjonstid ble variert, men dette resulterte ikke i faserent produkt. Rhenium(VII)oksid ble introdusert i de syntetiserte faserene bærerene ved to forskjellige introduksjonsmetoder, ionebytting og incipient wetness. Ionebytting i vann var ikke vellykket, men med etanol som løsemiddel ble 1,9 vektprosent rhenium introdusert i SAPO-34. Den sistnevnte metoden kunne ikke introdusere i nærheten like mye rhenium i de andre bærerene. Incipient wetness ble utført på SAPO-34, SAPO-5 og SBA-15, som resulterte i en vektprosent på over 2,3. Prøver med rheniuminnhold over 1,0 vektprosent ble redusert med to forskjellige varmebehandlinger. I den ene ble prøvene direkte redusert i H_2 ved 600°C i 2 timer, mens i den andre ble prøvene kalsinert i luft ved 700°C i 3 timer før reduksjonstrinnet i H_2 ble utført.

Røntgendiffraksjon (XRD) ble brukt til å bekrefte krystalliniteten til bærerene og identifisere rheniumfaser, overflatemålinger (BET, BJH) ble benyttet for å måle overflateareal og for å validere poresystemet til SBA-15, og elementærsammensetning ble analysert med ICP-MS. Diffus reflektans infrarød fourier transformert spektroskopi (DRIFTS) ble brukt for å undersøke om det var Brønsted surhet i SBA-15 syntetisert med aluminiumforløper, og scanning elektronmikroskopi (SEM) ble brukt for å avbilde SAPO-34 før og etter ionebytting

i etanol. *Ex situ* røntgenabsorbsjons spektroskopi (XAS) ble benyttet for å finne redusert fraksjon av rhenium og partikkelstørrelsen av metallisk rhenium. Det ble konkludert med at SAPO-34 og SBA-15, hvor rhenium var introdusert med incipient wetness og deretter direkte redusert, hadde rheniumpartikler av en størrelse som kunne befinne seg i porene til de respektive bærerene. Kalsineringssteget i det andre reduksjonsprogrammet førte til et stort massetap av rhenium.

Summary

This thesis is concerned with the synthesis of porous catalysts containing metallic rhenium nanoparticles. The goals of this work were to evaluate alternative introduction methods to the currently employed incipient wetness, and to evaluate the effect of different porous support properties, such as pore size and pore dimensionality. The porous support materials SAPO-34, AlPO-34, AlPO-5, SAPO-5 and SBA-15 were synthesized successfully. Novel routes to synthesize AlPO-34 without hydrofluoric acid were also attempted, where different compositions of structure directing agents and crystallization times were investigated, but did not result in any phase-pure products. The synthesized phase-pure supports were subjected to introduction of rhenium(VII)oxide by two different procedures: ion-exchange and incipient wetness. The introduction through ion-exchange was unsuccessful in aqueous solutions, but with ethanol as solvent a loading of 1.9 wt.% was achieved for SAPO-34. However, this method did not achieve appreciable loadings over 1 wt.% for any of the other supports. Incipient wetness was only performed on SAPO-34, SAPO-5 and SBA-15, where all resulted in loadings over 2.3 wt.%. Two different heat treatment programs were used for reduction. The first treatment was by reduction in H_2 at 600°C for 2 hours. In the second treatment a calcination step in air was performed at 700°C for 3 hours before the aforementioned reduction in H_2.

X-ray diffraction (XRD) was performed to verify phase-purity of the zeotypes, and also to detect rhenium phases. Surface measurements (BET, BJH) verified the surface area and validated the SBA-15 pore system, while elemental composition was analyzed by ICP-MS. Diffuse Reflectance Infrared Fourier Transform Spectroscopy (DRIFTS) investigated the presence of Brønsted acidity in SBA-15 samples synthesized with an aluminum precursor. Scanning Electron Microscopy (SEM) was used to image SAPO-34 before and after ion-exchange in

ethanol. *Ex situ* XAS was performed to investigate the fraction of reduced rhenium and the metallic particle sizes. By comparing the resulting metallic rhenium particle size to the pore size of the support material, the success of growth limitations of rhenium were evaluated. Growth limitations were achieved for SAPO-34 and mesoporous SBA-15 with rhenium introduced through incipient wetness, followed by direct reduction. Metallic rhenium particles supported in SAPO-34 has not been reported yet. The calcination step in the second heat treatment resulted in large rhenium mass loss for all samples.

Contents

Abbreviations

BET	Brunauner-Emmet-Teller
BJH	Barrett-Joyner-Halenda
CBU	Composite Building Unit
CHA	Chabazite
CTAB	Cetyl Trimethylammonium Bromide
DEA	Diethylamine
DRIFTS	Diffuse Reflectants Infrared Fourier Transformed Spectroscopy
DSC	Differential Scanning Calorimetry
EG	Ethylene Glycol
EXAFS	Extended X-ray Absorption Fine Structure
FCC	Face Centered Cubic
HCP	Hexagonal Close-Packing
HF	Hydrofluoric acid
ICP-MS	Inductively Coupled Plasma Mass Spectroscopy
IUPAC	International Union of Pure and Applied Chemistry
IZA	International Zeolite Association
Mor	Morpholine
PBU	Primary Building Unit
PEO	Polyethyleneoxide
PPO	Polypropyleneoxide
PXRD	Powder X-Ray Diffraction

SBU	Secondary Building Unit
SDA	Structure Directing Agent
SEM	Scanning Electron Microscopy
STP	Standard Temperature and Pressure
TEA	Tetraethylamin
TEAOH	Tetraethyl Ammonium Hydroxide
TEM	Transmissions Electron Microscopy
TEOS	Tetraethyl orthosilicate
TGA	Thermogravimetric Analysis
TPR	Temperature Programmed Reduction
XANES	X-ray Absorption Near-Edge Structure
XAS	X-ray Absorption Spectroscopy
XRD	X-ray Diffraction

Chapter 1

Introduction

Following the industrial revolution in the 1800s there was an immense need for food to sustain the seemingly endless population growth. [1] The solution to this great demand was mass production of fertilizers, which are made up by fixated nitrogen, potassium and phosphorus. The biggest challenge was to fixate N_2 into species that might be used as nutrient for fertilizers, such as nitrate, NO_3^-, or ammonia, NH_3.

The two Norwegians Kristian Birkeland and Sam Eyde were successful in fixating nitrogen into nitric oxide by blowing air through a plasma, but this required immense amounts of energy. [2] The work of Fritz Haber and Carl Bosch, the ”Haber-Bosch process”, led to a more energy efficient route by combining hydrogen and nitrogen into ammonia. Originally an osmium catalyst was used for this reaction, but it was quickly replaced by a catalyst made of iron, which is far more abundant and much less expensive. [3]

Currently the ammonia synthesis is one of the largest energy-consuming processes in industry, using approximately 1% of the world's produced energy. [4] However, the production of hydrogen from hydrocarbons through steam reforming is a major part of the ammonia plant. Steam reforming will not be considered in this work, only the formation of ammonia from pure nitrogen and hydrogen. Nonetheless, a lot of energy can be saved by mildening the reaction conditions for the synthesis of ammonia from H_2 and N_2, and also by reducing the number of purification steps for the precursor gases. The latter could be achieved by using a catalyst which is more resistant to catalyst poisons.

In today's industry the iron-catalyst is still the far most predominant catalyst for the ammonia synthesis. [5] A contender is the Kellogg Advanced Ammonia Process (KAAP), which employs ruthenium, a very rare metal relative to iron, supported on graphite. This catalyst has a much higher surface area, milder reaction conditions, and reports state that it is 10 to 20 times more active than the iron catalyst. [5]

Catalysts containing rhenium show potential for the synthesis of ammonia. [6] Research on rhenium has mainly been performed on its bulk phase, but investigation of supported rhenium is still needed. [6, 7] If the use of ruthenium in an industrial catalyst can be justified, this might also be the case for rhenium. In this thesis attempts were made to support rhenium on porous materials in order to achieve high surface-to-volume ratios for rhenium.

Chapter 2

Theory

2.1 Rhenium as a catalyst

Rhenium was discovered in 1925 as the last stable, non-radioactive and naturally occurring element, but it was not until several years later that it was extracted in reasonable amounts. [8] Today, most of the world's rhenium is used in superalloys in jet engines and in catalysis, such as Re-Co catalysts for hydrogenation of CO, Re_2O_7 catalysts for olefin metathesis and ReO_x in zeolites for selective oxidation of benzene to phenol. [9, 10] Rhenium catalysts are very resistant to chemical poisons such as phosphorous and sulphur. This property is especially useful for hydrogenation reactions, as the feedstock often contain these catalyst poisons. [11]

Bulk metallic rhenium is an active catalyst for the ammonia synthesis, but the activity is much lower than the commercial self-supported iron magnetite catalyst, Fe_3O_4. [7] The rate-determining step for both catalysts is dissociation of adsorbed N_2. For metallic rhenium, higher surface roughness and openness increases the reaction rate significantly. [12] Rhenium nitride, Re_3N, seems to have a slightly higher activity, but deactivates over time by being gradually converted to metallic rhenium. [7]

Kojima et al. attempted to improve the stability of the nitride phase by combining rhenium with different transitions metals. [7] The most active combination was cobalt and rhenium in a 1:4 molar ratio, which was reported to consist of rhenium metal, rhenium nitride and cobalt metal. The formation rate of NH_3 at 31 bars and 350°C was 2372 μmol h^{-1} g^{-1},

surpassing the industrial magnetite catalyst at these conditions. [7]

The $CoRe_4$ catalyst exhibit a surface area lower than 0.5 m^2g^{-1}, while the magnetite catalyst has a surface area of 14-20 m^2g^{-1}. [7] If the reaction is catalyzed through a surface reaction, increasing the surface area of $CoRe_4$ could improve its yield per gram catalyst even further. As metal particles decrease in size, the surface-to-volume ratio increases, and this extremely high surface area per mass makes nanoparticles exceptional in catalysis. [13] However, nanoparticles have a driving force towards reduction of surface area and hence must be stabilized, e.g. in a porous support.

This is what Kojima et al. [14] attempted when they supported Re on γ-Alumina with a surface area of 100 m^2g^{-1}, with wet impregnation resulting in 20 wt.% Re. In this experiment however, Co was not included, but they wanted to observe the effect of the alkali promoter cesium. The experiment without cesium resulted in Re particles of 33 nm after reduction, and activity on level with bulk metallic Re. With Cs:Re ratio of 1:1, the Re particles after reduction had a size of 110 nm, but with an activity equal to the $CoRe_4$ bulk catalyst at the previously stated conditions.

These results show promise for supported rhenium nanoparticles. However, as there are little to no reports of introduction of rhenium into porous support materials with size control. Size control means controlled introduction of rhenium into the pores, and will be one of the goals of this work. Growth limitations will be the second goal. This means that growth of rhenium is prevented during reduction due to constraints by the pore system, and it is also a measure of successful size control. This will be evaluated by observing how different pore sizes and dimensionalities in the support materials affect the metallic rhenium particle size.

2.2 Porous support materials

The porous supports that were subjected to introduction of rhenium are described in this section. Porous systems are classified by size. Microporous systems have pore diameters less than 2 nm, mesoporous systems have diameters between 2 and 50 nm and macroporous systems have diameters larger than 50 nm. [15]

2.2.1 Zeotypes

Zeotypes and zeolites are microporous and crystalline structures. Zeolites are defined as aluminosilicates, while zeotypes have zeolitic behaviour but may contain other elements than silicon and aluminum, e.g. phosphor, germanium, gallium and boron. [16, 17] The building blocks are corner sharing tetrahedra, e.g. $[AlO_4]^{5-}$, $[PO_4]^{3-}$ and $[SiO_4]^{4-}$, and are called primary building units (PBU). The order of which they are placed is not arbitrary. Löevenstein's rule states that the structure cannot be composed of Al-O-Al, which sets an upper limit to aluminum-content. [18] The tetrahedrically coordinated cations are aptly called T-atoms, and the oxygens function as bridges between them.

The size of the pores are defined by the ring-sizes, where 8-rings are defined as small, 10-rings are medium and 12-rings are large. [19] The driving force for formation of the pores and cages with different sizes are the addition of the so-called structure directing agents (SDA), which are large organic molecules, very often amines and quaternary ammonium. [20] The SDAs are still contained within the pores of the as-synthesized product, but are removed by calcination, which is heating a sample to high temperatures in air or oxygen. [21]

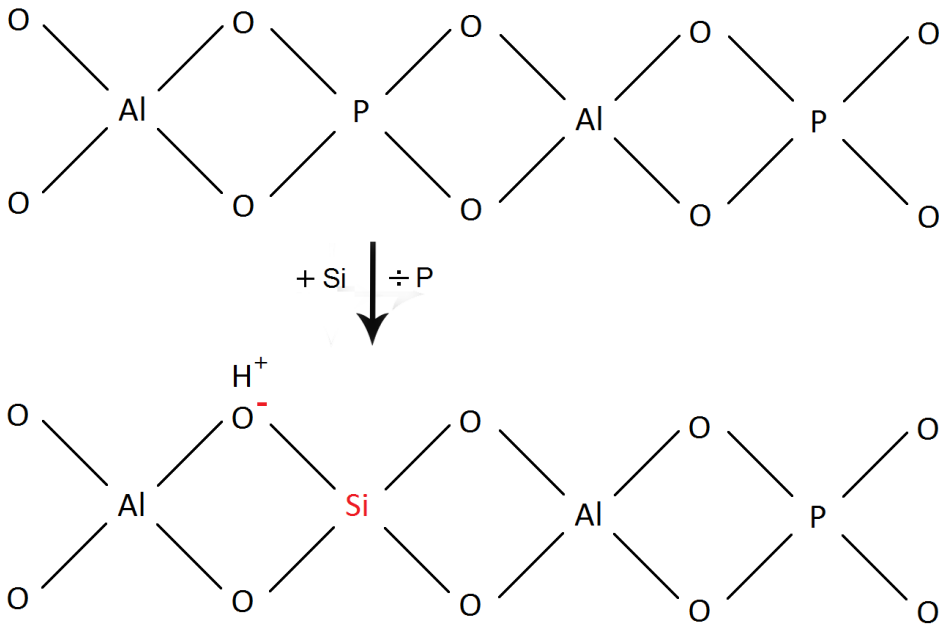

Figure 2.1: Illustration of the formation of Brønsted acidity when a phosphor in a neutral repeating structure of aluminophosphate is substituted by a silicon, to form a silicoaluminophosphate.

Due to the difference in valencies and the composition of T-atoms, charge imbalances may occur in the structure, which must be compensated by an external ion. For example if a Si substitutes P in the neutral Al and P alternating structure, this will result in a negative charge in the network, as illustrated in Figure 2.1. The negative charge is placed on the oxygen located between the Si and Al, which is called a Brønsted acidic site while the compensating cation is a proton. [22] The proton is exposed to the inner surface, and might be accessed by molecules inside the pores or cavities. The acidic strength of the Brønsted seat may also vary bond angles [23] and with the composition of atoms in the surrounding structure. [24]

SAPO-34 and AlPO-34

AlPO-34 is a zeotype containing Al, P and O, while SAPO-34 is the acidic analogy where Si has been substituted into the framework. [25, 26] Both share topology with the mineral chabazite (CHA), which has its structure illustrated in Figure 2.2. The 8-ring pores (small) has a diameter of 3.8 nm, while the elliptical cages has a diameter of 6.7 x 10 Å. [27] This results in a 3-dimensional structure, where the pores are not straight. Since these cages are larger than the pores, it gives the material shape-selectivity of reactants, intermediates and products. [28, 29]

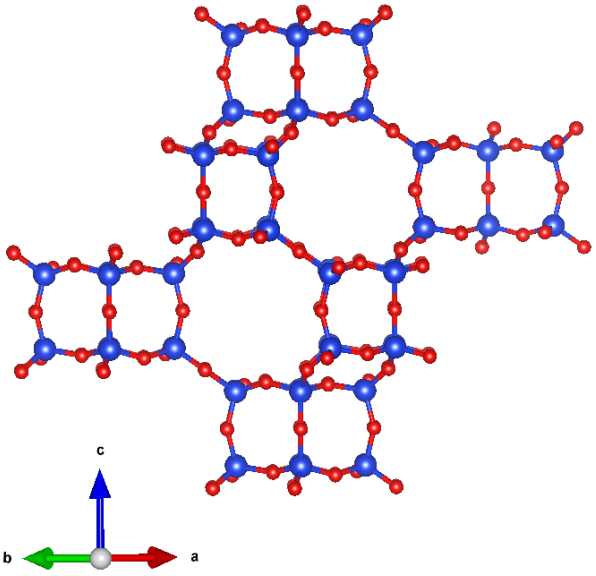

Figure 2.2: The CHA-structure modeled in VESTA, where blue atoms represent T-atoms, and red atoms are bridging oxygens.

SAPO-34 is more frequently employed than AlPO-34, and is very popular in the conversion from methanol to light olefins (MTO) due to its acidic properties, aforementioned shape-selectivity and small pores. [30] Its acidity can also be utilized by introducing metal ions via ion-exchange of protons at Brønsted sites. SAPO-34 is also very hydrothermally stable, and at over 1000°C the structure is intact and retains water adsorbing properties. [31]

Synthesizing AlPO-34 by standard MeAPO-34 or SAPO-34 synthesis routes is challenging. In order to stabilize the structure hydrofluoric acid (HF) is commonly added, which leads to two F^- bridging two Al, forming 4-rings which connect the double 6-rings of the structure. [25] After calcination the fluorine will be removed from the structure, and the structure should be that of CHA. However, in air and at 25°C the structure will be hydrated and reversibly transformed to triclinic CHA. [32]

One of the goals of this work will be to synthesize AlPO-34 without the use of HF. This is due to the hazards related to working with HF, and because halides act as poisons for some catalyst. [33] In an attempt to achieve this, already established routes for SAPO-34 were employed, but the addition of silicon was neglected. [34, 35, 36]. In addition to this, an attempt was performed on a reported procedure for fluorine-free AlPO-34 where the addition of ethylene glycol (EG) replaced HF. [37]

For the purpose of this work CHA is interesting due to its small pores, which can allow stabilization of very small nanoparticles. The 3-dimensional cages could also aid the retention of rhenium by trapping larger molecules or the metallic particles, which is a property the other support materials do not exhibit.

SAPO-5 and AlPO-5

SAPO-5 and AlPO-5 are zeotypes that has the same PBU as SAPO-34 and AlPO-34, but has a different structure. The pores are formed by 12-rings (large), and has a diameter of 7.3 Å, [19, 38] The pore framework is 1-dimensional, meaning the pores are straight and run parallel to each other. An illustration of AFI is shown in Figure 2.3. This pore system is quite different from CHA, as there are no cages, and with a pore aperture that is about twice as large.

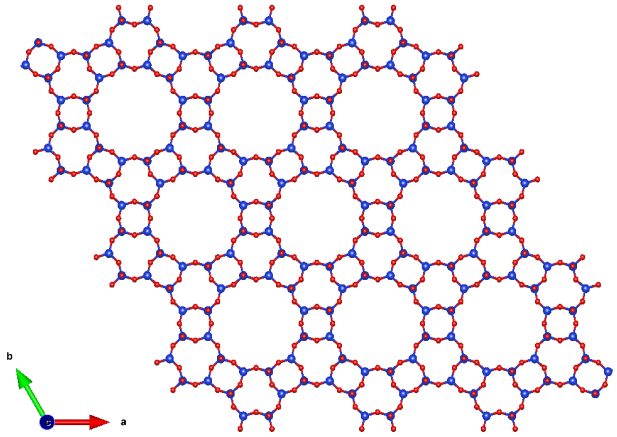

Figure 2.3: The AFI-structure modeled in VESTA, where blue atoms represent T-atoms, and red atoms are bridging oxygens.

2.2.2 Ordered mesoporous silica

SBA-15

SBA-15 is a highly ordered mesoporous silica (SiO_2) with surface areas ranging from 600 to 1000 m^2/g, and pore diameters typically in the range of 40 to 300 Å. [39] The use of surfactants and tri-block co-polymers yields uniform cylindrical pores and thick pore walls. These properties give the material a very high mechanical and hydrothermal stability. [40] An illustration of the structure is shown in Figure 2.4. SBA-15 is quite different from the two aforementioned microporous systems. The mesoporous silicia is quite different than the previously described zeotypic systems, and is an interesting comparison in terms of introduction, due to having a framework that might interact differently with rhenium, and subsequent growth limitations, due to having much larger pores.

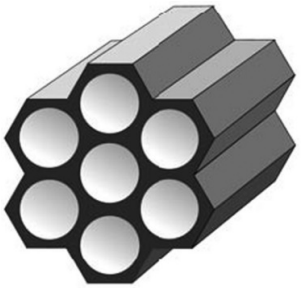

Figure 2.4: An illustration of the mesoporous silica SBA-15. [41]

All the support materials in this work are summarized in Table 2.1. They will allow for evaluation of how different support material properties affect the introduction of rhenium and the growth limitations during reduction. Properties that will be investigated are pore size, pore system and dimensionality.

Table 2.1: Summary of pore size, dimensionality and Brønsted acidity in the support materials that will be investigated.

Name	Pore system	Pore size [Å]	Dimensionality	Brønsted acidity	Reference
SAPO-34	Micro (small)	3.8	3D	✓	[26]
AlPO-34	Micro (small)	3.8	3D	X	[25]
SAPO-5	Micro (large)	7.5	1D	✓	[42]
AlPO-5	Micro (large)	7.5	1D	X	[43]
SBA-15	Meso	40-300	1D	X	[39]

2.3 Powder X-ray Diffraction (PXRD)

Powder X-ray diffraction (PXRD) aims monochromatic X-rays at a powder or micro-crystalline sample to be examined, while single crystal X-ray diffraction requires a single well-ordered crystal. When these beams diffract from the sample, some diffracting beams may cancel each other out through destructive interference, while the ones that amplify each other through constructive interference may be detected. This is determined by Bragg's law:

$$2d\,sin\,\theta = n\lambda \tag{2.1}$$

where d is the spacing between diffracting planes, θ is the incident angle, n is an integer, and λ is the wavelength of the beam. The principle of X-ray diffraction is illustrated in Figure 2.5.

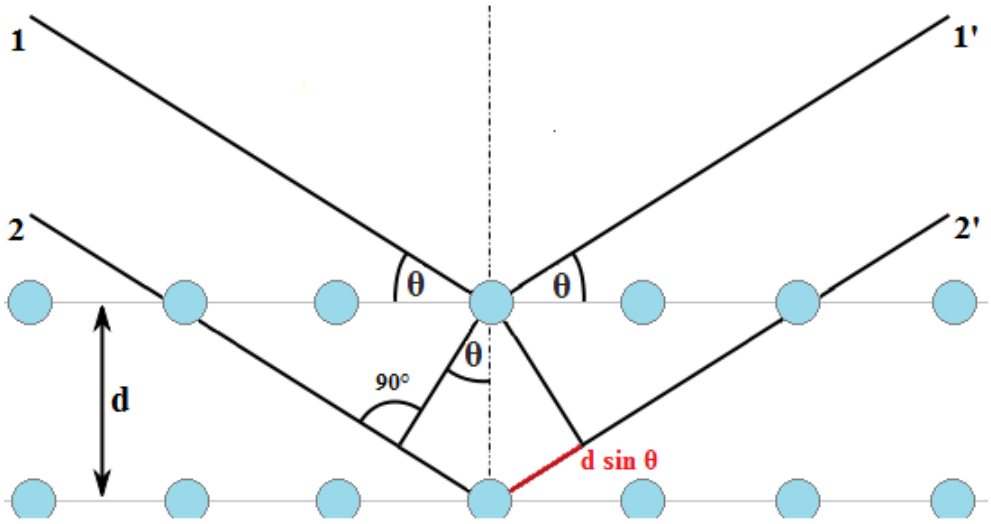

Figure 2.5: Illustration of the principle of X-ray diffraction. If the path length between to planes (2d sin θ) is equal to an integer (n) multiplied by λ, constructive interference can be observed.

The constructive interference will arise when the path length of the X-rays between the diffracting planes are equal. By measuring the angles, 2θ, of the constructively interfering X-rays that leave the crystal, Bragg's law (2.1) can be applied to find the corresponding lattice spacings, which are unique for a distinct compound. This technique is limited to samples with long range ordering, as one cannot have clear diffraction peaks without it. This can be convenient as the shape of the diffraction peaks contains information about dimension of the crystal planes, with perfect crystals resulting in narrow peaks. [15]

In this work XRD will be used to identify and confirm the phase of the synthesized zeotypes. The calculated diffractograms from the Atlas of Zeolites framework types for CHA and AFI are shown in Figure 2.6, [44] along with triclinic CHA as calculated by A. Tuel et al. [32] It will also be used to detect crystalline rhenium particles if the long-range ordering is high enough, and if the sizes are above 20 Å. [45] Diffractogram of rhenium references are shown in Figure 2.7

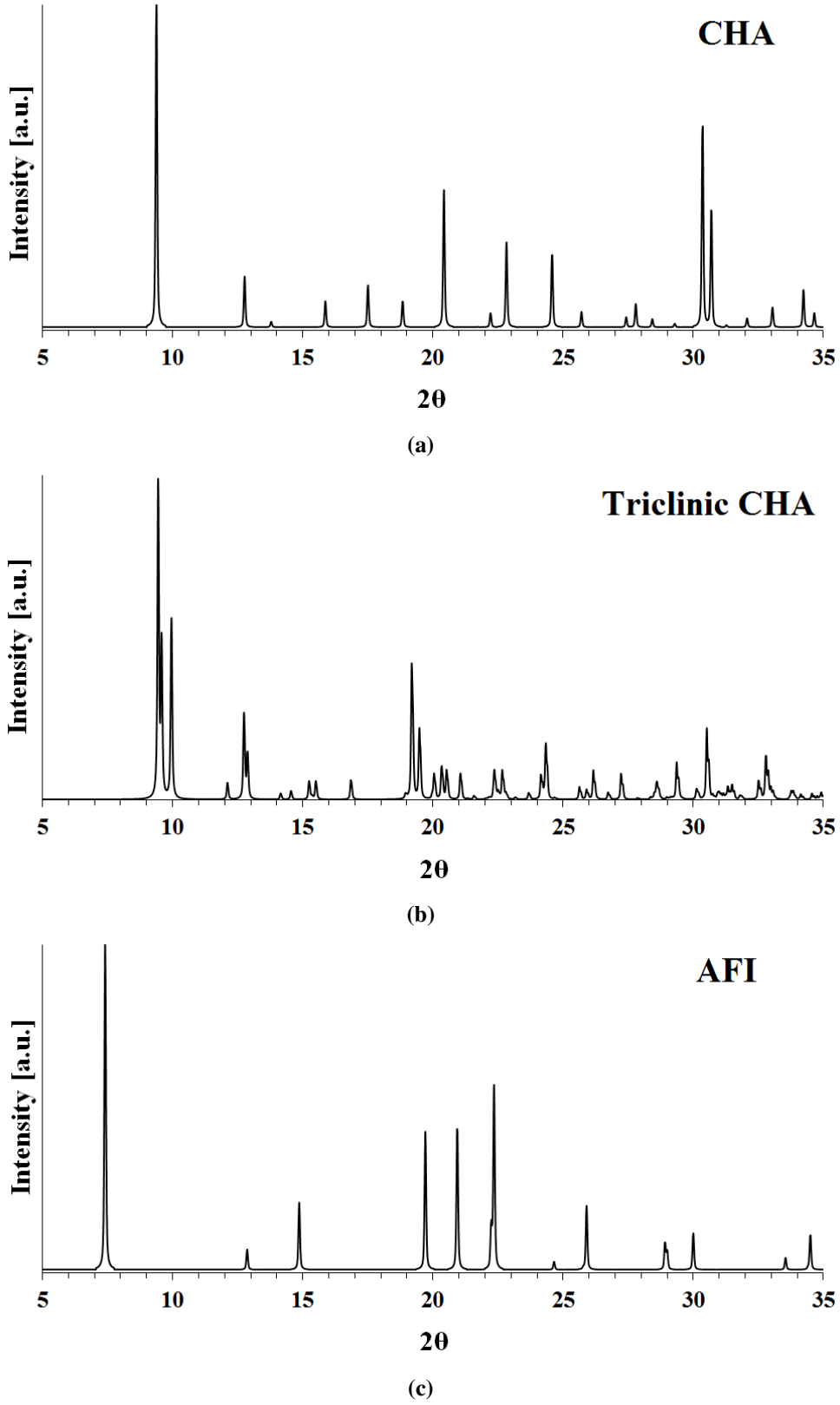

Figure 2.6: Calculated diffractogram (a) CHA and (c) AFI from the Atlas of Zeolites framework types, [44] and (b) triclinic CHA from A. Tuel et al. [32].

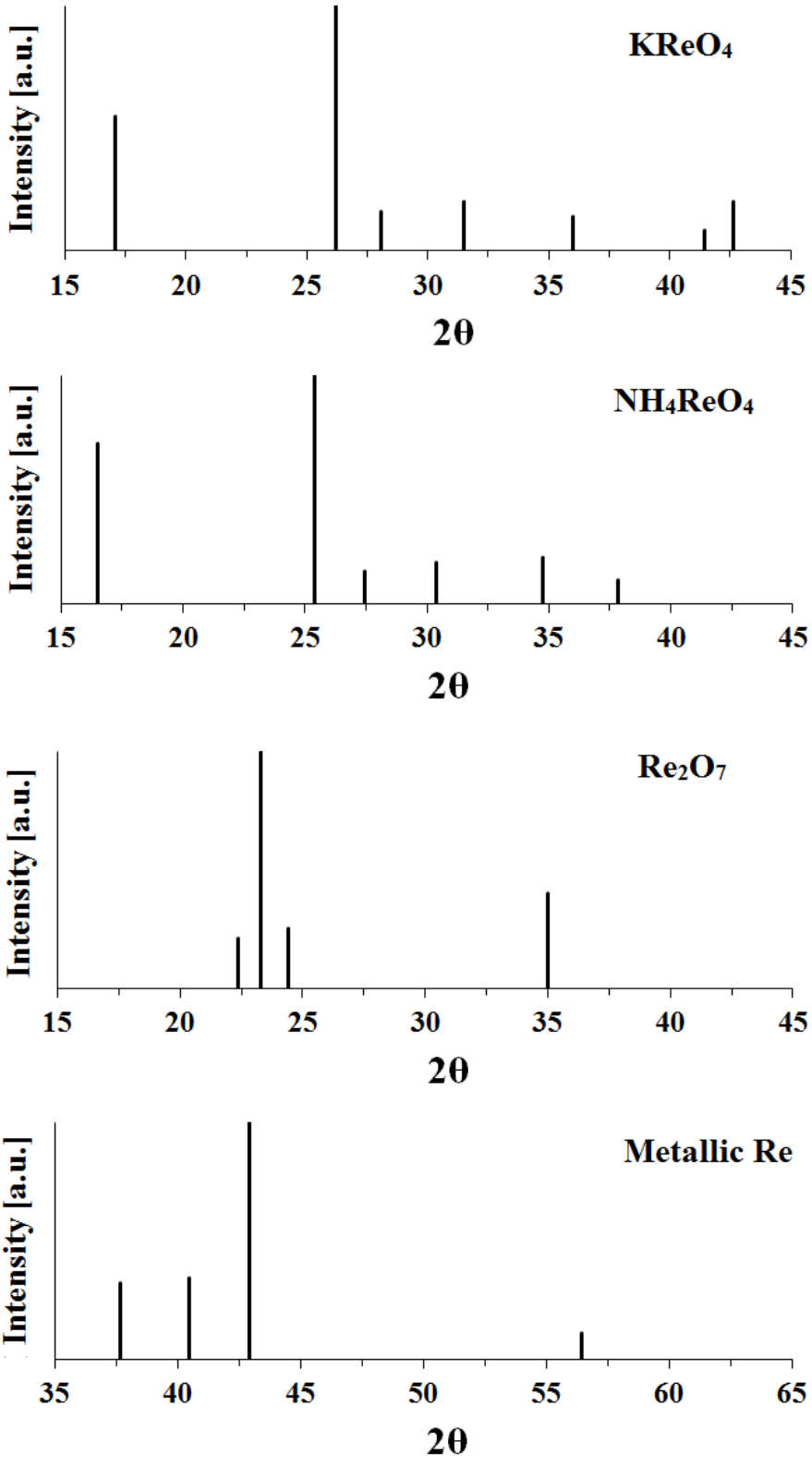

Figure 2.7: Calculated diffractogram of $KReO_4$ [46], NH_4ReO_4 [47], Re_2O_7 [48] and metallic Re [49] in the range where the most intense peaks are found.

2.4 BET

Micro- and mesoporous materials often have high surface areas. Brunauer, Emmett and Teller (BET) theory can be applied to determine the specific surface area of porous materials by physisorption of an inert gas. The inert gas is most commonly N_2, and the experiments is conducted at a temperature of 77 K, which is the condensation temperature of N_2 at atmospheric pressures. An adsorbed gas-molecule covers a known area, and by recognizing the pressure range of monolayer adsorption, the surface area of the sample can be calculated. [15]

The resulting isotherm from the surface measurement will vary, depending on pore size and pore composition of the material being analyzed. These are classified by IUPAC, [50] and are shown in Figure 2.8.

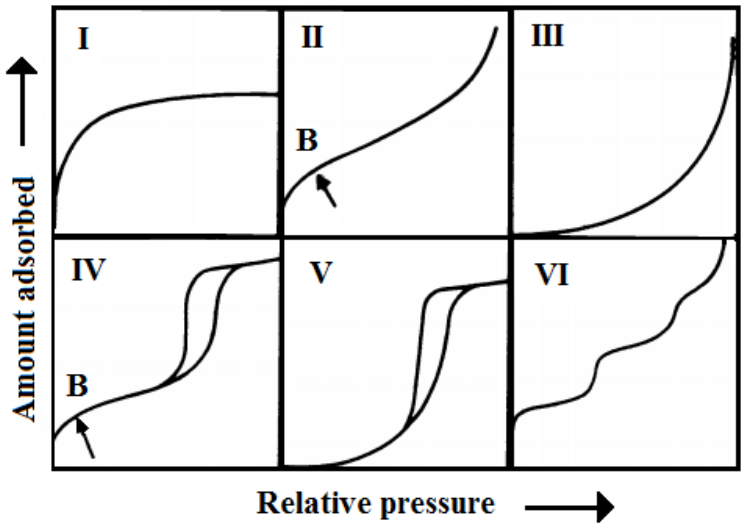

Figure 2.8: The different adsorption isotherms, as classified by IUPAC. [50]

Only isotherms relevant for the materials in this work will be considered here. For zeotypes a type I isotherms is expected, which is common for microporous materials with small external surfaces, monolayer adsorption and limited uptake governed by accessible micropore volume. Type IV appears in mesoporous materials such as SBA-15, and the hysteresis loop is due to capillary condensation. Point B indicates the stage at which the monolayer is complete, and multilayer adsorption begins.

Reported surface areas for the support materials in this work are listed in Table 2.2.

Table 2.2: Expected surface areas for the support materials in this work, based on reports in literature.

Support	BET surface area [m^2g^{-1}]	Reference
SAPO-34 and AlPO-34	400-700	[36]
SAPO-5 and AlPO-5	300-400	[51]
SBA-15	600-1050	[39]

A hysteresis loop appears due to capillary condensation and can exhibit a variety of shapes. These are also classified by IUPAC, and are shown in Figure 2.9. [50] H1 is common when the pore distribution is narrow and the mesopores are uniform. The H2 type is difficult to interpret, and has been attributed to different mechanisms in pores with narrow necks and wide bodies, but network effects must also be taken into account. H3 does not exhibit a limit in adsorption at high relative pressures, and is often observed in plate-like particles which yield slit-shaped pores. The H4 type often also have slit-shaped pores, but in the case of type I shape it is indicative of micropores.

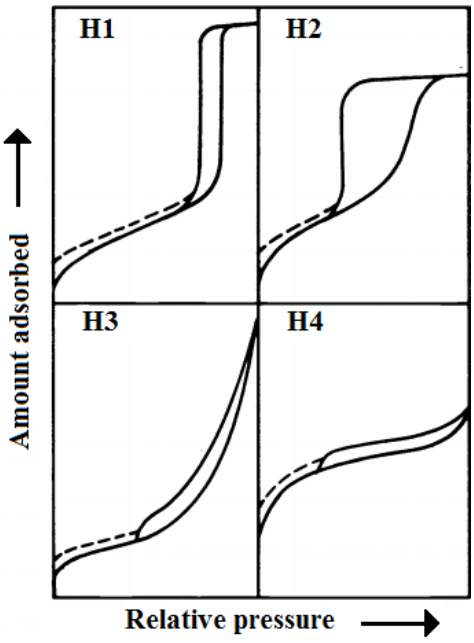

Figure 2.9: Different shapes of hysteresis loops in surface measurements of mesoporous materials, as classified by IUPAC. [50]

Pore size distribution of mesopores, and small macropores, can be found through the physisorption model by Barrett, Joyner and Halanda (BJH). [52] The Kelvin equation is used to find the pore width through information of the curvature of the condensed gas in the pores. The most predominant pore width can be found through the derivative of the BJH adsorption. This can be used to determine the pore size and distribution in the synthesized SBA-15, as these properties can vary with synthesis parameters.

2.5 Diffuse Reflectance Infrared Fourier Transform Spectroscopy

Diffuse Reflectance Infrared Fourier Transform Spectroscopy (DRIFTS) is an infrared spectroscopy technique which can be used for observing absorption of IR by vibration of bonds between atoms in molecules. [53] Two different bonds will be investigated in this work, the O-H bond stretching from silanols, which are OH-groups in structures with terminal silicons (-Si-OH), and the O-H bonds that arise from Brønsted sites. Absorbance of IR for silanols is observed around 3750 cm^{-1}, while Brønsted sites are at around 3600 cm^{-1}. [54, 55] Figure 2.10 shows a DRIFTS-spectrum of an acidic ZMS-5 zeolite with Si/Al ratio of 15. This illustrates at which positions the peaks for silanols and Brønsted acidity are expected.

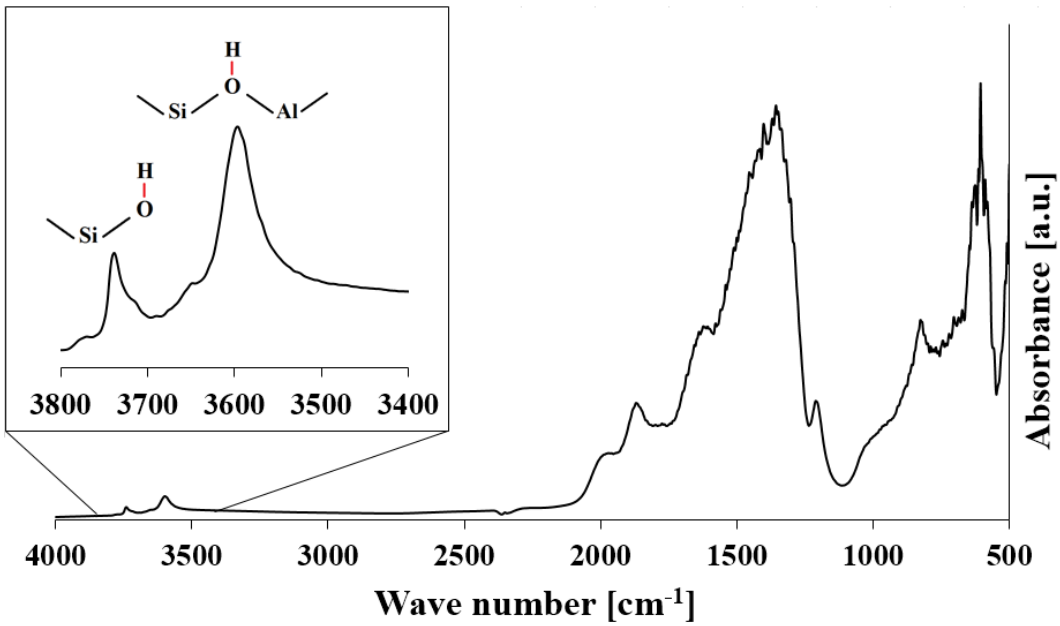

Figure 2.10: DRIFTS spectra of a ZMS-5 zeolite with Si/Al ratio of 15, at 350°C in synthetic air.

2.6 Metal introduction

A major goal in this work is to introduce rhenium into the support materials that were reviewed in the previous section. Some common methods of metal introduction into porous materials are ion-exchange, wet and dry impregnation, incorporation, chemical vapour deposition (CVD) and physical mixing. Here the focus will be on ion-exchange and dry impregnation by incipient wetness.

2.6.1 Ion-exchange

The type of ion-exchange that will be regarded here is cation exchange. At Brønsted acidic sites the H^+ can be exchanged for a metal cation. When a solution containing the desired metal cations penetrate the pores of the support, the metal cations can then exchange with the cation on the material surface. [56] Diffusion is the main transport mechanism of cations into the pores of the support, as illustrated in Figure 2.11.

The ion-exchange procedure ensures size control by washing, where excess ions are removed, and the remaining ions should be those with an ionic attraction to the material surface. During reduction the metallic species should then have growth limitations imposed by the pore system. [57] When the pore dimensions of the material are known, successful growth limitations are achieved if the metallic particle size is equal to or smaller than the pore or cage dimensions. [58]

2.6.2 Dry impregnation by incipient wetness

Incipient wetness impregnation aims to utilize capillary forces to transport the solute into the pores of the support. The precursor is dissolved in a small amount of solvent, but is not required to be ionic as with ion-exchange. In order to take advantage of the capillary forces, the solvent volume must be smaller than the pore volume of the support. [59] At higher metal loading the precursor might not have high enough solubility to be performed in one step, in which case several successive impregnation step must be performed. [60] With incipient wetness the solvent is transported through the pore system much faster than methods such as ion-exchange. [59] The transport mechanisms in incipient wetness is illustrated in Figure 2.12.

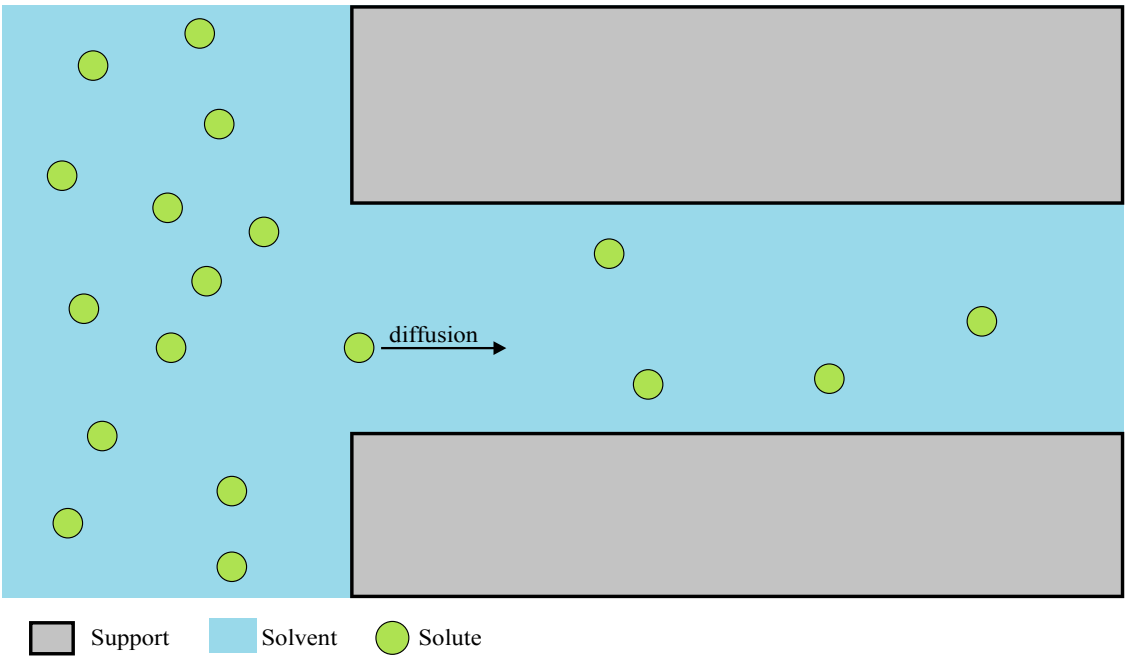

Figure 2.11: Illustration of diffusion of solute in a typical ion-exchange procedure.

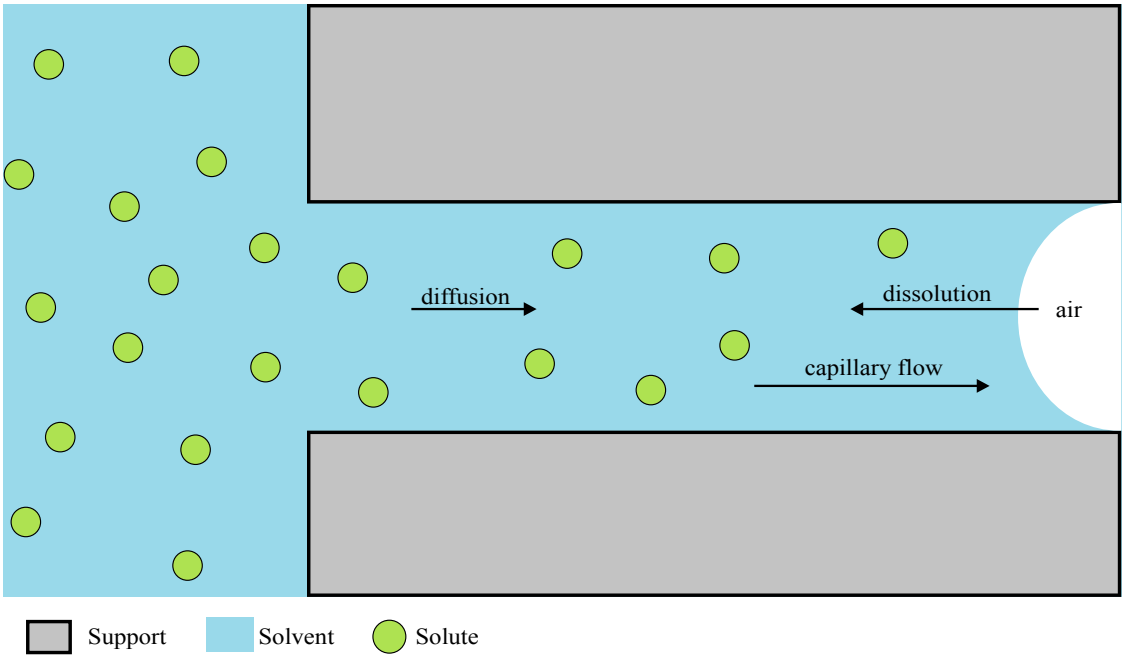

.

Figure 2.12: Illustration of transport mechanisms, mainly capillary flow, of solute in incipient wetness, which is achieved when the solvent is not in excess.

The incipient wetness procedure does not have a washing step, as that would likely lead to removal of the majority of introduced metal species. Therefore there is no assurance that the solute reside within the pores or cages. Subsequent reduction will therefore likely lead to a multimodal size distribution of the resulting metal clusters, because species in the pores will form small clusters due to growth limitations, while the species on the outside the pore system are allowed to grow. [56]

2.6.3 The rhenium problem

In literature the introduction of rhenium is only performed with methods *without* control of growth limitations. The most popular technique is incipient wetness, but there are also some reports of wet impregnation, CVD and physical mixing. [61] The most used support materials are 2-dimensional mesoporous materials, especially alumina and silica, [61, 62, 63] while 3-dimensional zeotypic systems are not well studied. As very few reports have been made regarding methods that allow size control of rhenium in porous support materials, this is as mentioned one of the major goals of this work.

A solution to the size control problem could have been to ion-exchange rhenium with protons in the support materials with Brønsted acidity. Unfortunately, when rhenium salts are dissolved in water they form oxyanions, not cations. [64] The rhenium precursor in this work was rhenium(VII)oxide, Re_2O_7, which forms perrhenic acid, $H^+[ReO_4]^-$, when dissolved in water. This precursor was chosen due to its high water solubility. [65]

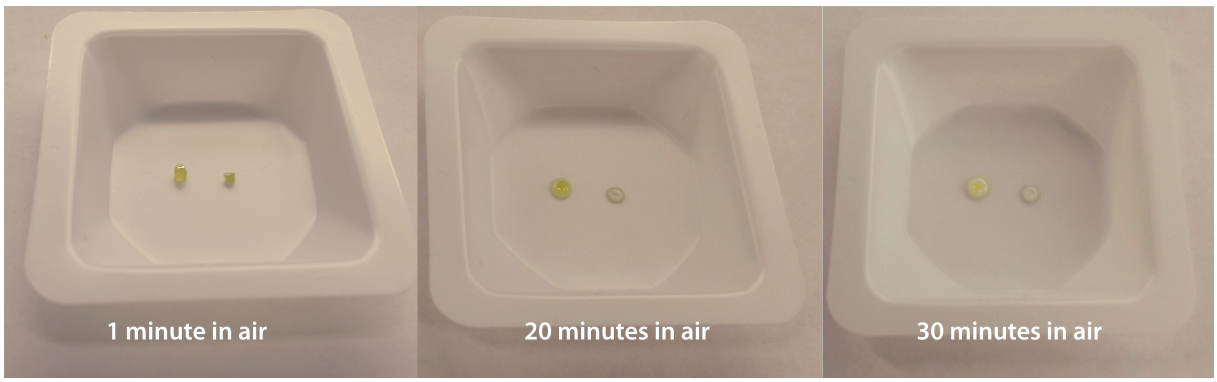

Figure 2.13: Illustration of Rhenium(VII)oxide, Re_2O_7, hygroscopic nature. The image shows crystals exposed to air for 1, 20 and 30 minutes.

Re_2O_7 is extremely hygroscopic, [65] to the extent where its crystals absorbs water from the air and are completely dissolved within 30 minutes, as illustrated in Figure 2.13. Thus, it is not only incapable of ion-exchange with cations in aqueous solutions, but it also has a very high preference for the water phase due to its hygroscopic nature. Washing with water will therefore likely remove the majority of the rhenium after an introduction step.

Alternative methods are therefore needed in order to introduce rhenium with size control. One option is to utilize rhenium's affinity for amines, which have been utilized in liquid-liquid extraction of perrhenate. [66] The SDAs used in the synthesis of the zeotypes and the surfactant in SBA-15 contain amine groups, but these molecules are removed during calcination. Therefore such experiments must be performed on as-synthesized or partially calcined support materials. Another option is to change the solvent for the ion-exchange procedure. This could give a different dissolved state of rhenium, and this state could potentially have a positive charge, which would allow interactions with the surface of acidic supports.

The form of introduced Re_2O_7 in the supports in this work is not known. For γ-Al_2O_3 some report that this can be dependent on loading, moisture and temperature, where ReO_4 tetrahedras are observed at lower loadings, while above 10 wt.% Re_2O_7 is also present. [67] While the interaction between rhenium oxides and the alumina support can be relatively strong, [62] it cannot be assumed that it is the same for the support materials regarded here. Therefore the precursor form after the introduction was not asserted on beforehand.

2.7 Inductively Coupled Plasma - Mass Spectroscopy (ICP-MS)

Inductively Coupled Plasma-Mass Spectroscopy (ICP-MS) is a technique where a dissolved sample is ionized by atomizing it in a high temperature plasma source, which is subsequently introduced into a mass spectrometer for analysis. [68] ICP-MS is a superior method at yielding elemental composition of samples, and its importance in this thesis is its detection limit of metal species introduced in the porous supports, which can be down to parts-per trillion (ppt, 10^{-12}).

2.8 Scanning Electron Microscopy (SEM)

Scanning Electron Microscopy (SEM) is an imaging technique. The resolution is dependent on the instrument, and can be anywhere between 1 and 100 nm. An electron beam is scanned across the surface of the sample, and secondary electrons and back-scattered electrons are detected and used to form an image. [69] The sample must be conductive and grounded in order to avoid charging of the sample. If it is non-conductive, as is the case with the samples regarded in this work, a coating of a conductive material must be applied, often gold or graphite. The interest of SEM in this work will be to observe changes to the support particles before and after introduction of rhenium.

2.9 X-ray Absorption Spectroscopy (XAS)

X-ray Absorption Spectroscopy (XAS) is the study of X-rays absorbed by matter. [70] It is an element specific bulk technique, and is very useful for determining oxidation states, coordination numbers and chemical environment. XAS is primarily performed at a synchrotron, as it requires a very intense and energy tunable X-ray source. The synchrotron radiation is obtained when electrons at near relativistic speeds are subjected to magnetic fields. Bending magnets bend the trajectory of the electrons and insertions devices, sets of magnets with alternating polarities, make the electrons undulate (wiggle/oscillate), which produces electromagnetic radiation along the electron path. Before this radiation can be subjected to the sample, the beam must pass through several slits and monochromators in order to obtain an X-ray with known size and energy.

The parameter of interest in XAS is the X-ray absorption coefficient, μ, and it is found by measuring the intensity of the incident and the transmitted radiation. This follows Lambert's law:

$$I_t = I_0 e^{-\mu(E)x} \tag{2.2}$$

where I_t is the intensity of the transmitted beam, I_0 is the intensity of the incident beam, μ(E) is the X-ray absorption coefficient as a function photon energy E, and x is the thickness of the sample.

An important feature is the absorption edge, a sharp increase in the X-ray absorption coefficient. The energy at the position of this sharp edge is labeled E_0, and it is the threshold energy for the absorption of X-rays. This coincides with the ionization of core electrons, in other words; the incident X-rays have the same energy as the binding energy of the core electrons. When an electron is ejected from the material it is known as the photoelectric effect, and the ionized electron is called a photoelectron. When the energy is higher than the threshold energy the photoelectron has a kinetic energy of $E_k = (E-E_0)$. Figure 2.14 shows the mass attenuation coefficient as a function of photon energy for rhenium. [71] For heavier elements the K or L edges are often measured, and for rhenium it is usually the L_{III}-edge. E_0 for the metallic Re-foil at the L_{III}-edge is tabulated at 10535 eV at the inflection point of the absorption edge. [72]

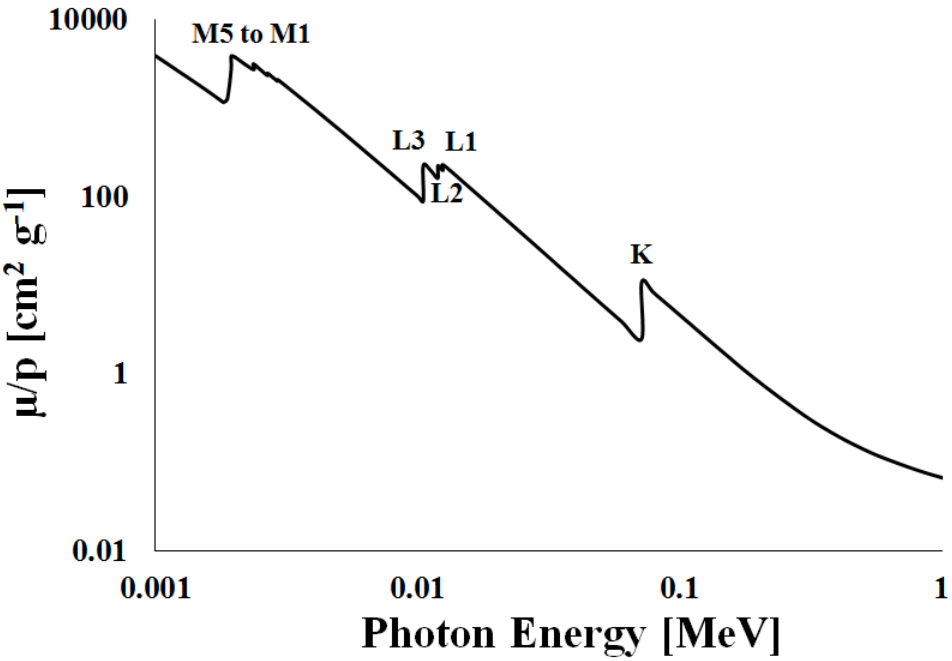

Figure 2.14: Rhenium mass attenuation coefficient (μ/p) as a function of photon energy for rhenium (Z=75). [71]

The XAS spectrum is divided into two regions. The X-ray Absorption Near-Edge Spectroscopy (XANES) studies an area of 30 eV within the absorption edge, depending on the edge features. The Extended X-ray Absorption Fine Structure (EXAFS) examines the spectrum from 50 eV after the absorption edge and up to 1000 eV after the absorption edge. This is illustrated with a rhenium foil sample in Figure 2.15.

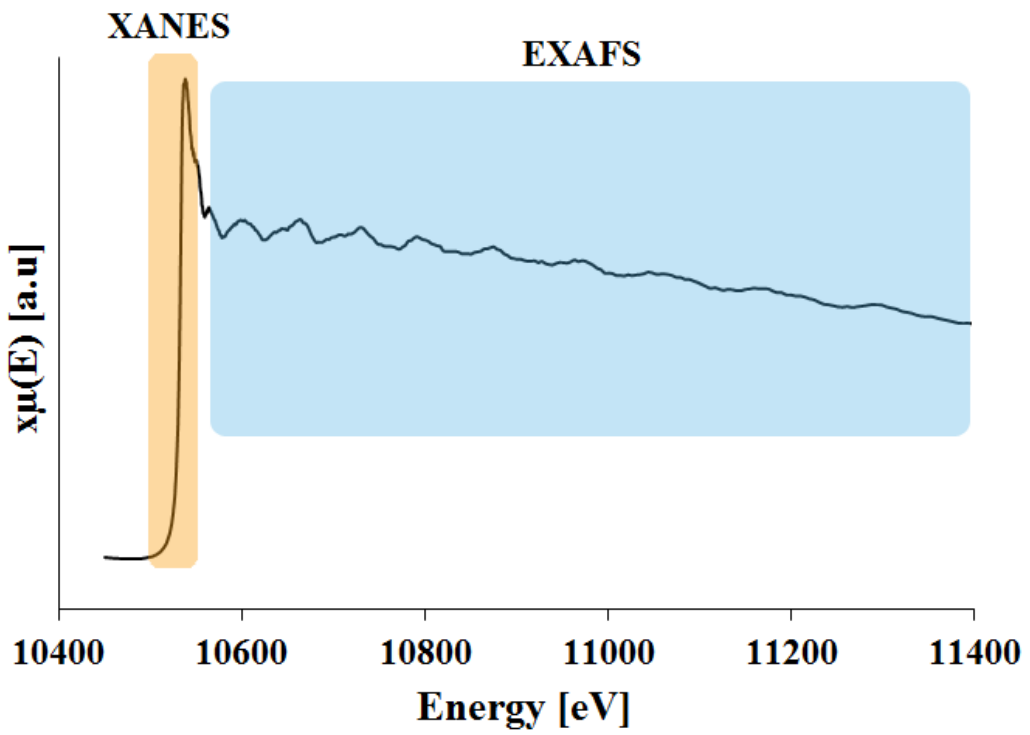

Figure 2.15: The division of XAS into the XANES and EXAFS region, with a rhenium foil spectrum as example.

2.9.1 X-ray Absorption Near Edge Structure (XANES)

XANES for rhenium is normally studied 5-10 eV before the absorption edge, and around 35 eV past the main absorption edge. Changes in electronic states will be reflected in this region, which are the oxidation state and the environment of the atom in question. There are no absorption pre-edges present for the Re L_{III}-edge, thus the phenomenon will not be discussed in this thesis. The XANES of some rhenium references are illustrated in Figure 2.16.

The shift in the energy of the absorption edge, E_0, can often be explained by effective nuclear charge. With increasing oxidation state the shielding effect on the higher orbital electrons will decrease, effectively increasing their attraction to the nucleus. Thus, more energy is required to excite these core electrons to a high energy state, resulting in E_0 being shifted to higher energies. For transition metals in the first d-block ($3d$), the K-edge often have a very clear shift in energy due to oxidation state. However, for rhenium and other elements in the third d-block ($5d$) the L_{III}-edge shift is much less pronounced. This is explained by the fact that the final $5d$ states are far less localized than the final $3d$ states, thus a smaller shift in energy with increasing oxidation state is observed. [73]

Figure 2.17 illustrates the correlation between E_0 and oxidation state of the references from Figure 2.16. There is no linear increase in E_0 as the oxidation state increases, as both ReO_2 and ReO_3 has a lower E_0 than the Re foil. It is therefore difficult to use the shift ni E_0 as a method to determine the oxidation state at the Re-L_{III} edge. However, literature reports that an increasing intensity, or integrated area, of the white line is an indication of increasing oxidation state. [73, 74] The increase in the intensity is explained by an increase in electron deficiency in the d-orbital at higher oxidation states. [74] For the references in Figure 2.16 there is an increase in intensity with increasing oxidation state, but the trend is not linear as ReO_3, Re(VI) has higher intensity than all Re(VII) references.

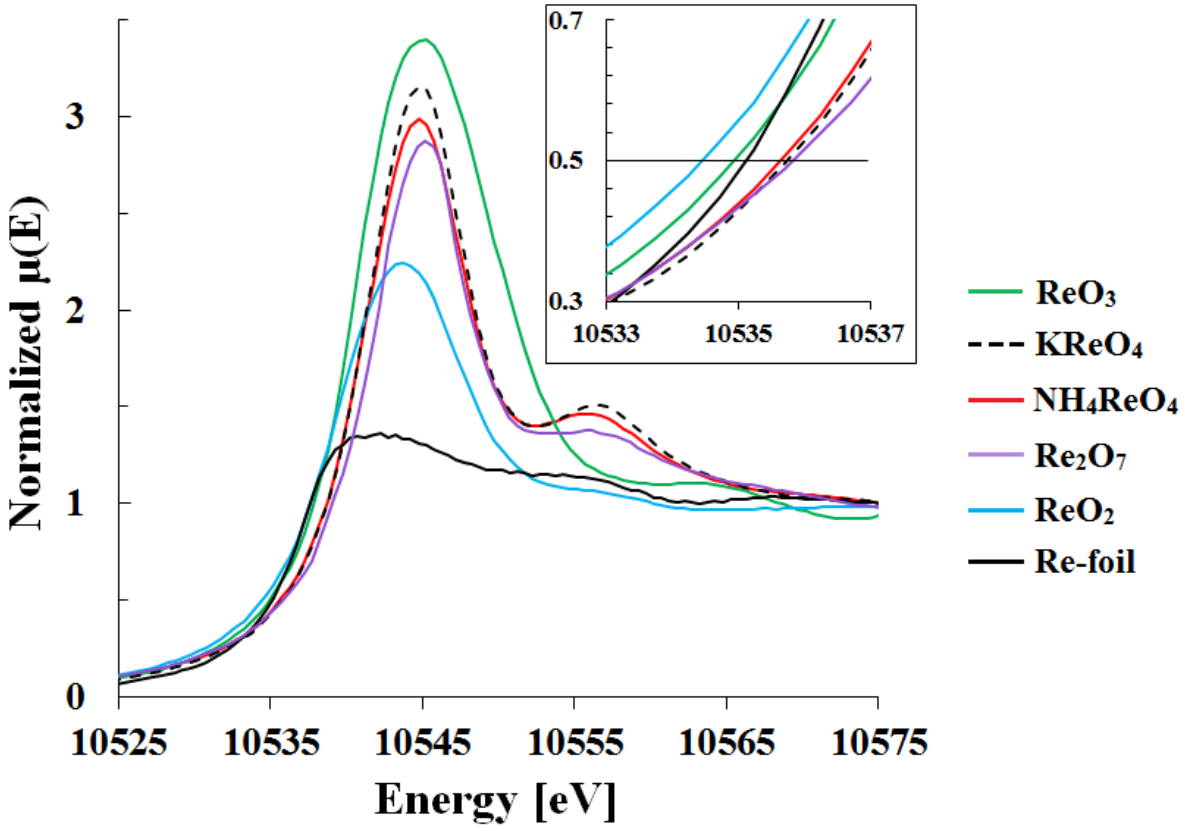

Figure 2.16: The normalized XANES of a selection of rhenium references, here Re-foil (0), ReO_2(+IV), ReO_3(+VI), $KReO_4$ (+VII), NH_4ReO_4(+VII) and Re_2O_7(+VII). The area around 0.5 up the normalized plot is zoomed in, in order to see the difference in E_0.

The XANES of the references do not have many distinct features, but one of them is the peak after the absorption edge, around 10558 eV, which is present in the Re(VII) references. This peak is also present in the Re-foil, but with lower intensity.

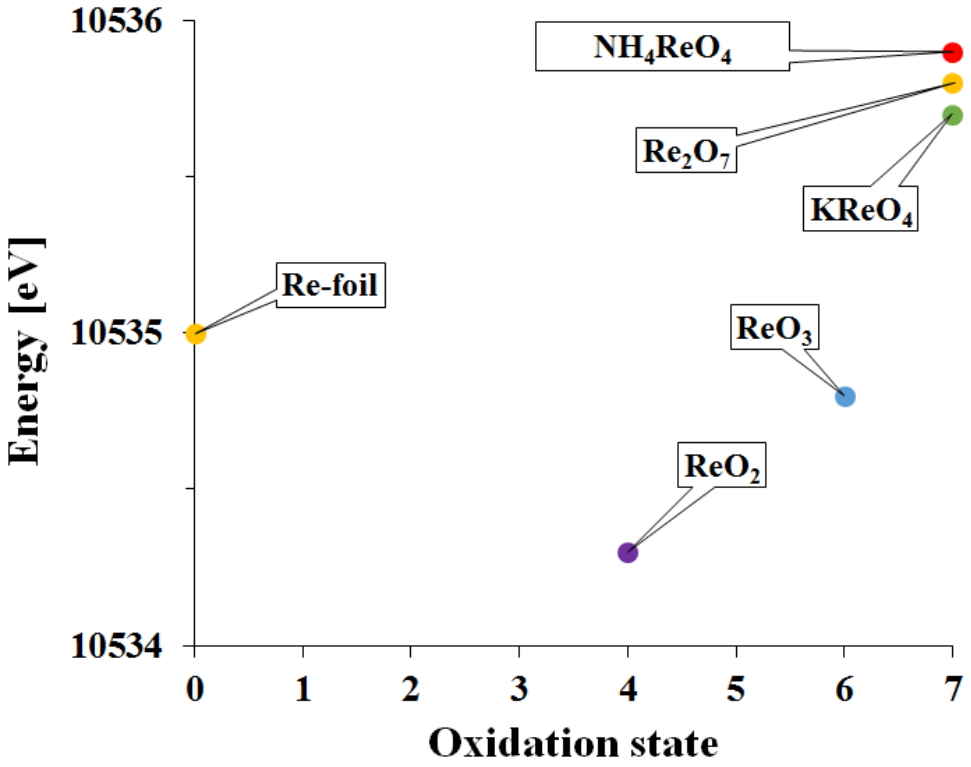

Figure 2.17: The E_0 value chosen at 0.5 up the normalized μ(E) for the rhenium references Re-foil (0), ReO_2(+IV), ReO_3(+VI), $KReO_4$ (+VII), NH_4ReO_4(+VII) and Re_2O_7(+VII).

The reducibility of rhenium supported on alumina has been a topic for discussion for several decades, revolving around the amount of rhenium being reduced. [75] If both metallic rhenium and rhenium oxides are present, this will lead to contribution of both to the XANES, and also the EXAFS. In the XANES these contributions can be singled out by a method such as least-square linear combination. This is performed by a software that uses references and combines them with varying degrees of contribution in order to obtain the best fit with the sample. This can for example be used to determine how large the reduced fraction of rhenium is in a reduced sample, by linear combination of metallic rhenium and rhenium oxide references.

2.9.2 Extended X-ray Absorption Fine Structure (EXAFS)

EXAFS ranges from the end of XANES, and up to about 1000 eV from the absorption edges. In this region the energy is high enough to excite an electron to continuum, emitting a photoelectron. The photoelectron travels from the core as wave with kinetic energy, E_k, and when it hits a neighbouring atom the wave it is back-scattered. When an outgoing photoelectron wave interacts with a back-scattered wave, interference between them causes an oscillating wave to be observed in the XAS spectrum. Constructive interference will give an increase in the absorption coefficient, while destructive interference will decrease it. The interference between these waves will depend on the type of neighbouring atoms and their bond distance, as well as thermal and structural disorder which may dampen the signal.

The scattering atoms are often to referred to as shells. A shell contains only one type of atom and is positioned at a fixed length from the absorber, also called bond length or interatomic distance. The number of atoms in the shell is referred to as the multiplicity or the coordination number.

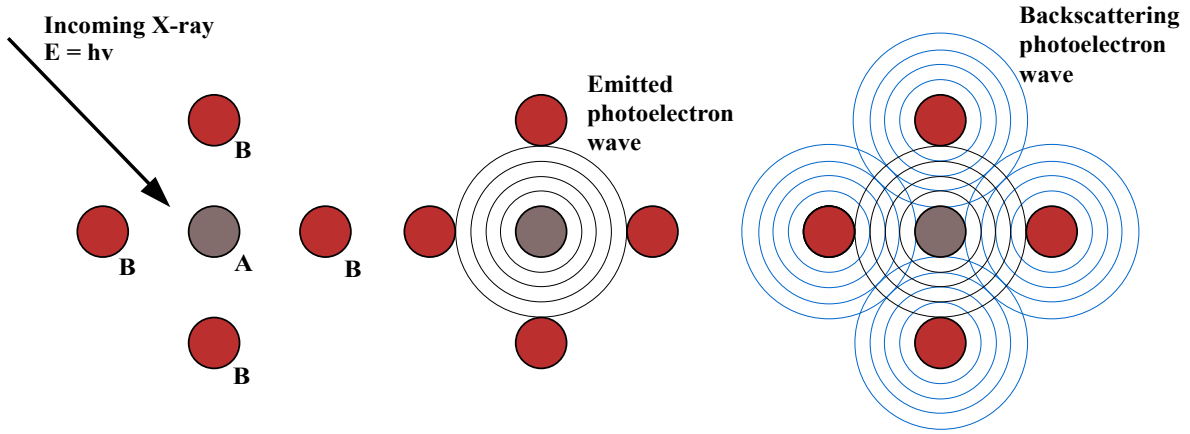

Figure 2.18: An illustration showing the interaction between an emitted photoelectron wave as a result of absorbed X-rays, and backscattered photoelectron waves.

To extract the fine structure oscillations in the XAS, the EXAFS fine-structure function χ(E) is extracted from the measured μ(E). This is performed by subtracting atomic absorption and normalizing the data with the absorption jump value to eliminate sample density:

$$\chi(E) = \frac{\mu(E) - \mu_0(E)}{\Delta\mu_0(E)} \tag{2.3}$$

where χ(E) is the normalized EXAFS data, μ(E) is the measured X-ray absorption coefficient at a given X-ray energy, μ_0(E) is the background function represented by the absorption of an isolated atom and $\Delta\mu_0$(E) is the absorption jump at the threshold energy E_0. As the photoelectron will be considered a wave, it is common to convert the energy to the wave number, k. This is performed through Equation 2.4, where m is the mass of the photoelectron, (E-E_0) is the kinetic energy of the photoelectron and $\hbar$ is the reduced Plank constant.

$$k = \sqrt{\frac{2m(E - E_0)}{\hbar^2}} \tag{2.4}$$

In order to extract information from the experimental χ_i^{exp}(k), the theoretical expression called the EXAFS equation is used. The EXAFS equation is based on the plane-wave single scattering approximation. [76] The plane-wave approximation assumes that the atomic radii is much smaller than the interatomic distances, and thus the curvature of the photoelectron wave is ignored. This approximation is only valid for higher k-values (k>3Å). Single scattering assumes that the electron path is directly between the absorber and the back-scatterer.

To find the aforementioned information from the fine structure, a fit is made between the experimental χ_i^{exp}(k)-curve and the theoretical χ_i^{th}(k)-curve resulting from user suggested values of the j number of shells. These values should reflect the expected local atomic structure. The software inserts these values into the EXAFS equation, Equation 2.5, and refines the suggested values by using a least-square approach in an attempt to minimize the difference between the modeled fit and the experimental data. The calculation for the statistical fit-parameter R is shown in Equation 2.6. [77]

$$\chi(k) = \sum_{j=1}^{Shells} \frac{N_j}{kR_j^2} S_0^2 F_j(k) e^{-2k^2\sigma_j^2} e^{\frac{2R_j}{\lambda(k)}} sin[2kR_j - \phi_j(k)] \tag{2.5}$$

- j: The j^{th} neighbour shell.
- N_j: The coordination number of the j^{th} shell.
- k: The wavenumber converted from energy.
- R_j: The distance between the absorbing atom and the j^{th} shell.
- S_0: The amplitude reduction factor. Corrects relaxation effects in the emitting atom.
- $F_j(k)$: Elemental specific back-scattering factor of the j^{th} shell.
- σ_j: The Debye-Waller factor of the j^{th} shell.
- λ: The inelastic mean free path of the electron.
- $\phi_j(k)$: The total phase-shift of the photoelectron
- $e^{\frac{-2r}{\delta}}$: Exponential attenuation of the electron.
- $e^{-2k^2\sigma_j^2}$: Reduction factor for static and dynamic disorder in the solid.

$$R = \sum_{i}^{N} \left[\frac{1}{\sigma_i} |\chi_i^{exp} - \chi_i^{th}| \right] \times 100\% \tag{2.6}$$

χ(k) is weighted by k^n (n = 1, 2 or 3) to make up for the loss of EXAFS signal in the high k region. A higher weighting can prevent the lighter elements, which scatters mainly at low k-values, from dominating the signal over the heavier elements, which scatter at high k-values. A Fourier transform is performed on the k^n-weighted χ(k), which transforms the function to R-space (Å), where each peak corresponds to a coordination shell.

Interatomic distances and multiplicities for the first coordination shell in bulk metallic Re, ReO_3 and NH_4ReO_4 are shown in Table 2.3. [62]

Table 2.3: Interatomic distances, R, and multiplicities, N, for the first coordination shell in metallic rhenium, ReO_3 and NH_4ReO_4. [62]

Compound	Scatterer	R[Å]	N
Re foil	Re	2.74	12
ReO_3	O	1.87	6
NH_4ReO_4	O	1.74	4

2.9.3 EXAFS and metallic nanoparticles

In this work the goal was to introduced rhenium into the pore system of the porous support, followed by reduction to yield metallic rhenium nanoparticles with growth limitation imposed by the pore system. If this is performed successfully, the metallic nanoparticles should have sizes smaller to the sizes of the pores in the support material it was introduced in. [57, 58] The pore sizes for SBA-15 are verified by BET and BJH, while the zeotypes must be verified as phase-pure by XRD to have the pore size of their corresponding topologies. In this work EXAFS will be used to investigate the size of metallic rhenium nanoparticles.

The multiplicity from EXAFS can be used to approximate the size of the metallic rhenium clusters. When metal clusters reduce in size an increasing fraction of atoms will reside on the surface. Atoms at the surface will have fewer neighbouring atoms than the atoms in the center of the cluster. Thus, reducing the particle size will decrease the average multiplicity. [13] However, a more quantitative approach is desirable. De Graaf et al. introduced platinum nanoparticles in a zeolite, and related the size of the Pt particles with the first coordination shell by combining results from EXAFS, chemisorption and transmission electron microscopy (TEM). [78] By assuming that the platinum nanoparticles were spherical they computed the number of atoms, and related it to the platinum particle size.

Metallic Pt is face centered cubic (FCC) with Pt-Pt bond length of 2.78 Å, while metallic Re is hexagonal close-packed (HCP) with Re-Re bond length of 2.74 Å. [62] Both have close-packing with 12 nearest neighbours while in bulk, but the geometry of the two packings are different. However, these results were used as an approximation to relate the multiplicity of metallic rhenium to the metallic rhenium particle size.

The relation between coordination and particle size was extracted from De Graaf et al. [78], and corrected for the difference in bond length, R, in rhenium and platinum as shown in Equation 2.7. A relation between particle size and the multiplicity, N, can be used to create a polynomial function.

Figure 2.19 shows the the plot with the polynomial function, which is corrected for the bond length of Re.

$$\text{Bond length correction} = \frac{R_{Re-Re}}{R_{Pt-Pt}} = \frac{2.74}{2.78} = 0.986 \tag{2.7}$$

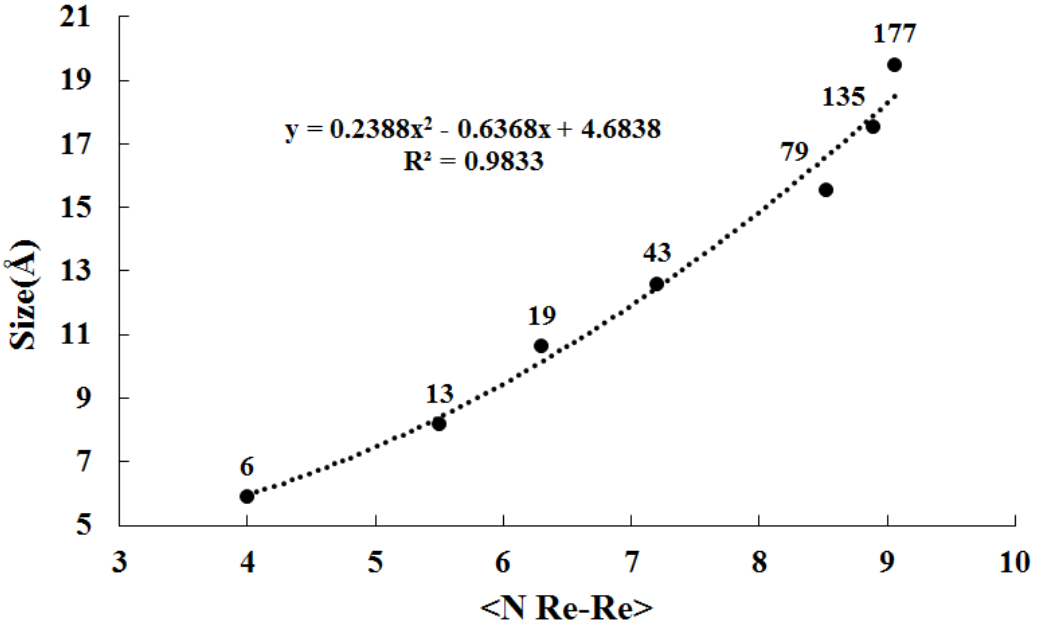

Figure 2.19: Relating multiplicity and number of atoms to the size of Re nanoparticles. Data based on De Graaf et al., and corrected for Re-Re bond length. [78]

If samples investigated by EXAFS have a Re-Re shell at around 2.74 Å, the multipilcity of this shell can be inserted into the polynomial equation in Figure 2.19, which will result in an approximation of the rhenium nanoparticle size. However, there are some limitations to this method due to the fact that the polynomial function is created for multiplicities between 4 and 9.1. EXAFS will therefore not be appropriate for determining metal particle sizes with multiplicities above 10. Also, if the uncertainty in the multiplicities are large, it will have a severe effect on the certainty of the approximated particle size.

Another concern while using this calculation arises if samples are not completely reduced, meaning a mixture of metallic and oxide rhenium is present. As XAS is a sum of the sample in the cross section of the beam, presence of rhenium oxide will give an apparent coordination of Re-Re which is lower than what the metallic clusters realistically have. If the reduced fraction of rhenium, F_{red}, is calculated, the multiplicity can be corrected to a more realistic value. The equation for this correction is shown in Equation 2.8, where a corrected multiplicity, N_{corr} can be found by dividing the multiplicity from EXAFS, N_{EXAFS}, by the reduced fraction of rhenium.

$$N_{corr} = \frac{N_{EXAFS}}{F_{Red}} \tag{2.8}$$

Chapter 3

Experimental

3.1 Synthesis

3.1.1 AlPO-34 and SAPO-34

The general procedure for synthesis of AlPO-34 and SAPO-34 without addition of HF will be described here. In the different proecures there are some variations in the molar ratios and the composition of the SDAs, which are detailed in Table 3.1. The procedures of SAPO-34 and AlPO-34 with TEAOH as SDA is a modification of a BASF patent [34], while the procedure with 3 SDAs and 4 SDAs are modifications of the work of Masoumi et al. [35] and Najafi et al. [36] respectively.

Orthophosphoric acid (H_3PO_4,85%, 8.7 g) was added to deionized water (41.9 g), followed by slow addition of aluminum isopropoxide ($Al[OCH(CH_3)_2]_3$, 98%, 15.3 g), which was stirred until homogeneous. For SAPO-34 AS-40 Ludox (SiO_2, 40% colloidal suspension in H_2O) was added, and subsequently the organic SDA(s) were added dropwise. The different organic SDAs used were tetraethylammonium hydroxide (TEAOH, 35%), tetraethylamine (TEA, $\geq$ 99%), diethylamine (DEA, $\geq$ 99.5%) and morpholine (Mor, $\geq$ 99%). The suspension was stirred until it was homogeneous, and then in some cases aged. Ageing means that the homogeneous suspension was left without any agitation for a longer period of time.

The suspension was then transferred to a stainless steel autoclave with a Teflon liner. Hydrothermal synthesis was performed by heating the autoclave to 190 °C, and crystallized for the durations listed in Table 3.1 The solid product formed by the hydrothermal synthesis was rapidly cooled to room temperature by placing the hot autoclave in cold water. The product was then centrifuged and washed with deionized water several times, before being dried at 70°C over night. The dried product was mortared and then calcined at 550°C for 6 hours in order to remove organic SDAs from the pores.

Table 3.1: All AlPO-34 and SAPO-34 samples without addition of HF listed with molar ratios with respect to Al and P being 1.0, duration of the hydrothermal synthesis and duration of ageing. The Crystallization temperature was 190°C for all procedures.

Sample name	Si	TEAOH	Mor	TEA	DEA	H_2O	Cryst. time [h]	Ageing [h]
SAPO-34/1	0.2	0.9	-	-	-	28	72	-
SAPO-34/2	0.3	0.9	-	-	-	28	72	-
SAPO-34/3	0.4	0.9	-	-	-	28	72	-
SAPO-34/4	0.9	0.9	-	-	-	28	72	-
AlPO-34/1	-	0.9	-	-	-	28	72	-
AlPO-34/2	-	0.9	-	-	-	28	168	-
AlPO-34/3	-	0.5	0.25	0.25	-	35	24	8
AlPO-34/4	-	0.5	0.25	0.25	-	35	132	8
AlPO-34/5	-	0.2	0.3	0.1	0.4	35	14	8
AlPO-34/6	-	0.2	0.3	0.1	0.4	35	24	8
AlPO-34/7	-	0.2	0.3	0.1	0.4	35	96	8
AlPO-34/8	-	0.2	0.3	0.1	0.4	35	168	8

The synthesis of AlPO-34 by already established routes followed the procedure of Wang et al. [79] for addition of hydrofluoric acid (HF), and Wu et al. [37] for ethylene glycol (EG). Both these procedures follow the general procedure described above, except for the addition of HF and EG. For AlPO-34EG ethylene glycol (EG, $\geq$ 99%) was added added after the aluminum isopropoxide, prior to the SDAs. For AlPO-34HF hydrofluoric acid (HF, 40%) was added as the last precursor followed by 45 minute stirring. The molar ratios for the precursors and the temperature and duration of the hydrothermal synthesis are listed in Table 3.2, while the procedures are illustrated in Figure 3.1.

Table 3.2: AlPO-34 samples synthesized with addition of hydrofluoric acid (HF) or ethylene glycol(EG). Listed are the molar ratios being with respect to Al and P being 1.0, and the temperatures and durations of the hydrothermal syntheses.

Sample name	Mor	HF	EG	H_2O	Cryst. temp. [°C]	Cryst. time [hours]
AlPO-34HF	4.5	0.06	-	12.5	190	120
AlPO-34EG	3.0	-	4.05	50	185	192

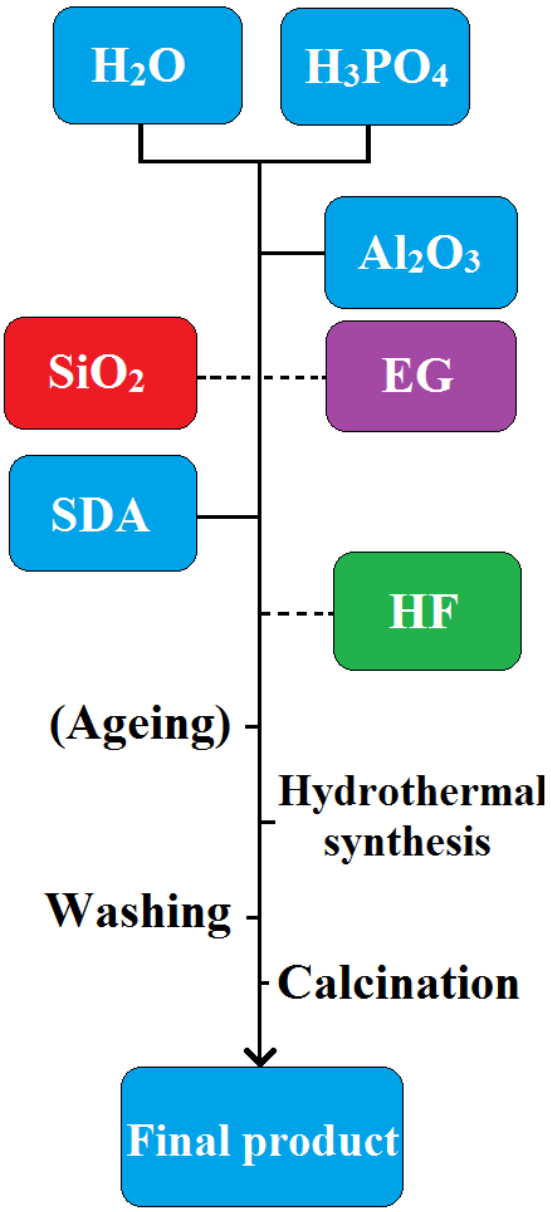

Figure 3.1: Illustration of the general procedure of SAPO-34 and AlPO-34. The blue boxes are components added for all syntheses, while the other boxes with dashed lines are the additions used in SAPO-34 (SiO_2), AlPO-34 with ethylene glycol (EG) and AlPO-34 with hydrofluoric acid (HF). Ageing is in parenthesis due to only being used in some syntheses.

3.1.2 AlPO-5 and SAPO-5

The procedure for synthesis of AlPO-5 and SAPO-5 are very similar, and in terms of precursors they differ only by the fact that SiO_2 is added for SAPO-5. Deionized water (48.5g) and orthophosphoric acid (H_3PO_4, 85 wt%, 11.5g) were mixed, and pseudo-boehmite (Al_2O_3, 71.6 wt.%, 7.07g) was added slowly, and then stirred until the mixture was homogeneous. AS-40 Ludox (SiO_2, 40% colloidal suspension in H_2O, 3.0 g) for SAPO-5, and tetraethylamine (TEA, $\geq$99 wt.%, 6.07g), were added drop-wise, followed by stirring for 30 minutes. This yielded the theoretical gel composition Al: P: x Si: 0.6 TEA: 35.2 H_2O.

The resulting gel was poured into a Teflon-lined autoclave, which was heated at 200C° for the duration listed in Table 3.3. The resulting powder was washed and centrifuged several times, before being dried at 70°C over night. The as-synthesized material was calcined at 650°C for 16 hours to remove the organic SDA.

Table 3.3: SAPO-5 and AlPO-5 samples with Si molar ratio and crystallization time.

Sample name	Si(x)	Crystallization time [h]
SAPO-5/1	0.2	48
AlPO-5/1	-	48
AlPO-5/2	-	72

3.1.3 SBA-15

For the synthesis of SBA-15 two quite different procedures were used, the conventional route with hydrochloric acid (HCl) and cetyltrimethylammonium bromide (CTAB), [80] and a halide-free approach with H_3PO_4 and aluminum isopropoxide, a modified version of the work of Wang et al. [81]. The two procedures will be described individually. The rinsing of the as-synthesized product were similar for both procedures, where the as-synthesized SBA-15 was filtered through a Büchner funnel with a Whatman® quantitative ashless Grade 589/3 blue ribbon filter paper. Firstly the as-synthesized powder was rinsed 2 times with ethanol, then 5 times with water, followed by 2 times with ethanol to allow faster drying. After being dried, the product was calcined at 550°C for 12 hours.

The reagents in these procedure were poly(ethylene glycol)-block-poly(propylene glycol)-block-poly(ethylene glycol) (Pluronic P123, average M_n ~5,800), cetyltrimethylammonium bromide (CTAB, $\geq$ 99%), tetraethyl orthosilicate ($Si(OC_2H_5)_4$, TEOS, 98 wt.%), orthophosphoric acid (H_3PO_4, 85%), hydrochloric acid (HCl, 1.5M) and ethanol (CH_3CH_2OH, 100%).

SBA-15 with HCl and CTAB

P123 Pluronic (0.5g) was dissolved in hydrochloric acid (60 mL). In a separate container CTAB (0.6g) was dissolved in deionized water (25 mL). After both P123 and CTAB were dissolved, the two solutions were mixed and heated to 35°C. Ethanol (20 mL) was then added, followed by dropwise addition of TEOS (9.4 g), and stirred at 35°C for 45 minutes. The solution was then split evenly into two 80 mL stainless steel autoclaves, and heated at 80°C for 17 hours. Hydrothermal synthesis was then performed by increasing the temperature to 100°C for one parallel, and 140°C for the second parallel, for 5 hours. The as-synthesized product was rinsed and calcined.

SBA-15 with phosphoric acid and aluminum

P123 Pluronic (0.5g) was dissolved in 100% ethanol (9.48 g). In a separate container deionized water (30 mL), H_3PO_4 (6.75g) and aluminum isopropoxide (0.27g) was mixed and stirred for 3 hours. The solution from the first container was added dropwise to the second, which was then stirred for 20 hours at 60°C. After this TEOS (1.1g) was added dropwise to the solution, which was stirred for another 20 hours at 60°C. The solution was then heated and kept at 90°C for 48 hours in a centrifuge bottle with a stopper to keep it sealed. The as-synthesized product was then rinsed, followed by calcination.

An illustration of the two procedures are shown in Figure 3.2, and summarized in Table 3.4.

Table 3.4: Crystallization time and temperature for the three SBA-15 samples.

Sample name	Description	Cryst. temp [°C]	Cryst. time [hours]
SBA-15/100	Conventional	100	5
SBA-15/140	Conventional	140	5
SBA-15/Al-P	Halide-free	90	48

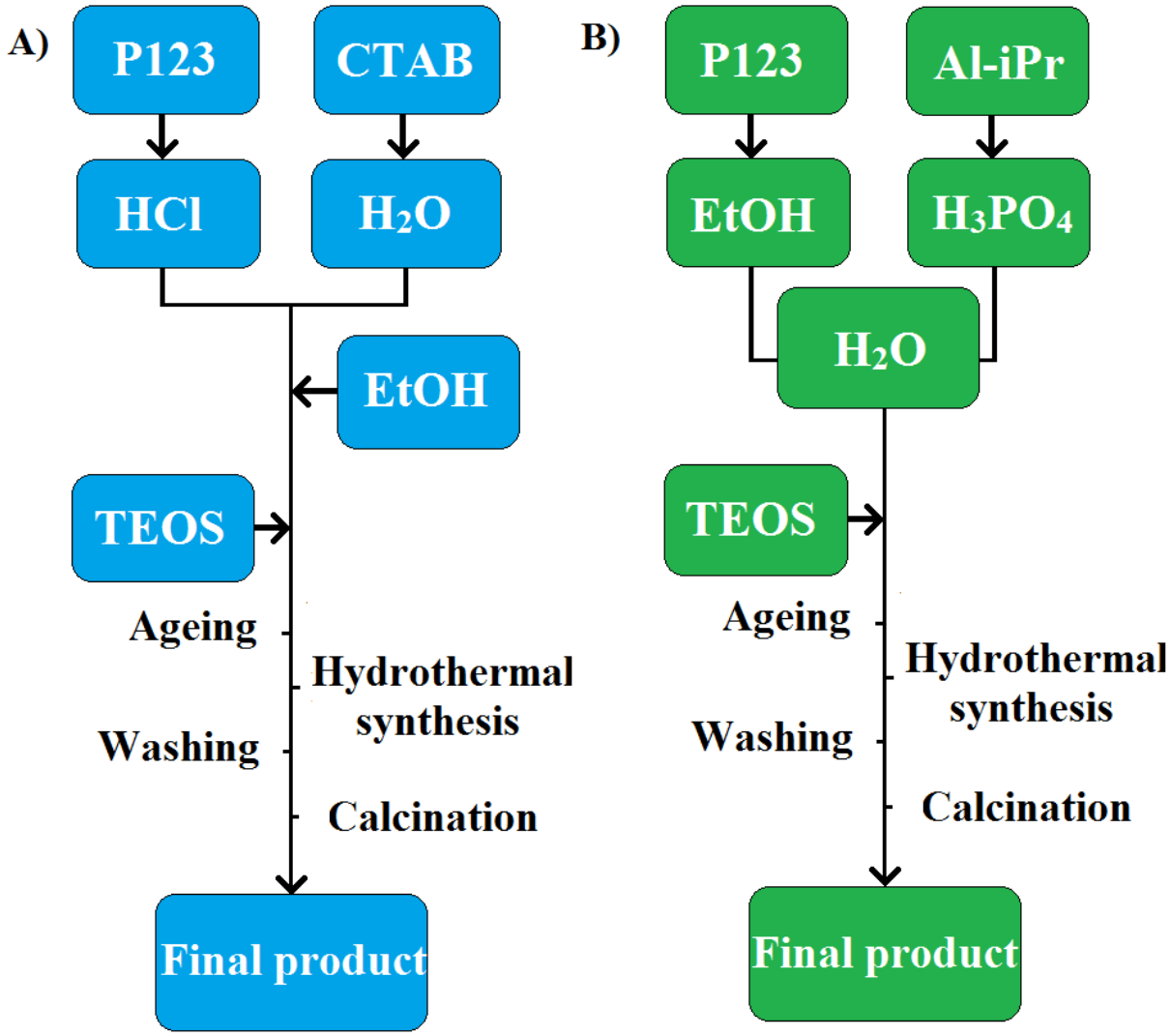

Figure 3.2: An illustration of the procedure for the synthesis of SBA-15 where A) shows the conventional route, and B) the halide-free route.

All the syntheses of the porous support materials are summarized in Table 3.5. Here each type of support is listed along with a short description of the performed procedures, in addition to the varied parameter for that procedure. The procedures that was performed once, will have the variation listed as ”None”.

Table 3.5: Summary of all synthesized support materials, along with a short description and the varied parameter for each procedure. If only one synthesis was performed, the variation is ”None”.

Support	Synthesis description	Varied parameter
SAPO-34	1 SDA	Si-content
AlPO-34	1 SDA	Crystallization time
	3 SDAs	Crystallization time
	4 SDAs	Crystallization time
	HF	None
	EG	None
SAPO-5	1 SDA	None
AlPO-5	1 SDA	Crystallization time
SBA-15	Halide-free	None
	Conventional	Crystallization temperature

3.2 XRD

All of the diffractograms were recorded with a Bruker D8 Advance DaVinci X-Ray Diffractometer with Cu Kα radiation. The diffractometer used a constant slit opening of 1mm and step size of 0.1 seconds per step and angles measurements from 5 to 75 2θ of for the support materials. For detection of rhenium the divergence slit was set to open automatically such that the illuminated length on the sample always remained 6 mm. The angle measurements were in the range of 20-90 2θ for metallic rhenium and 15-75 2θ for rhenium oxide.

3.3 Surface area measurements

BET and BJH measurements were performed by using a Micromeritics Tristar 3000 Surface Area and Porosity Analyzer. In advance of measurements, samples weighing between 0.01 and 0.03 g were degassed in vacuum at 250°C for 24 hours. A filler rod was used in the sample holder. Samples were cooled to 77 K with liquid nitrogen, and N_2 gas was used as the adsorbate gas. The specific surface area was calculated using the BET equation. [82] Pore volume and pore size distribution was calculated using the BJH method. [52] Micropores are not measured for the BJH method, and therefore these results will not be reported for the zeotypes.

3.4 DRIFTS

Samples were pressed to wafers and subsequently crushed and sieved to obtain a particle size between 425 and 212 µm. The sieved particles were filled in a small porous ceramic cup, and the surface of the particles were smoothed. Samples were heated in synthetic air at 550°C, before recording spectra with a Bruker VERTEX 80 spectrometer.

3.5 Metal introduction

3.5.1 Ion-exchange

For the conventional ion exchange procedure 0.48 g Re_2O_7 (99.9%) was dissolved in 20 mL deionized water, forming a solution with a concentration of 0.1 M Re. 0.3 g dry porous support material was then added to the solution, which was stirred for 24 hours. The dry supports were in this case as-synthesized or calcined SAPO-34. The resulting suspension was then washed and centrifuged 3 times with the water. The resulting sample was dried in a Petri dish overnight at 110°C.

Partial calcination prior to ion-exchange

As-synthesized supports were weighed out and calcined individually at temperatures between 200 and 500 °C, with a ramp rate of 2°C per minute, and dwelled at a given temperature for 3 hours. The partially calcined samples were then subject to the ion-exchange procedure with water described above, but with a 25 mL 0.03 M Re-solution from Re_2O_7 (99.9%), and 0.4 g partially calcined support. After 1 day of stirring the sample was washed and centrifuged 3 times, then dried in a Petri dish overnight at 110°C. Some samples were calcined at 550°C for 6 hours to remove the remaining organic SDAs after drying.

Ion-exchange with ethanol and acetone

The same procedure as conventional ion-exchange was performed, but with different solvents. Re_2O_7 (99.9%) was dissolved in 20 mL ethanol (CH_3CH_2OH, 100%) or acetone ($CH_3(CO)CH_3$, 100%) to give a Re concentration of 0.01 or 0.1 M. Quickly after dissolution of the rhenium salt, 0.3 g of the support was added, then stirred for 1 or 2 days. The samples were washed with the ion-exchange solvent and centrifuged 3 times. As the low density of SBA-15 made it unsuitable for centrifugation, the powder was instead filtered in a Büchner funnel with a Whatman® quantitative ashless Grade 589/3 blue ribbon filter paper, and rinsed several times with the solvent used in the ion-exchange.

3.5.2 Impregnation by Incipient wetness

0.0195 g Re_2O_7 (99.9%) was weighed out in a weighing ship and dissolved in a small amount of water. The volume of water depends on the support pore volume, and was typically 0.25 ml per gram SAPO-34 and AlPO-34, 0.15 mL per gram AlPO-5 and SAPO-5, and 1.2 ml per gram SBA-15. This amount of Re_2O_7 was calculated to yield 3.0 wt.% Re for the impregnated sampled. 0.5 g of the support was weighed out in a narrow crucible, a few drops were dropped onto a glass rod placed in the crucible, followed by stirring. This was performed in order to spread the solution into the support more effectively. This was repeated until all of the solution was employed. The crucible was then heated at 110°C for 12 hours.

The experiment was also attempted by placing the support in a narrow column, and adding the concentrated Re-solution. The solution only penetrated the top layer of the support, and it did not wet the bottom part. Therefore this method was discarded, and the crucible method was employed instead. Figure 3.3 shown an illustration of two different introduction procedures, ion-exchange and incipient wetness.

XRD was performed in order to detect rhenium after rhenium had been introduced and the sample was dried. The procedure and settings for these measurements were described in Section 3.2.

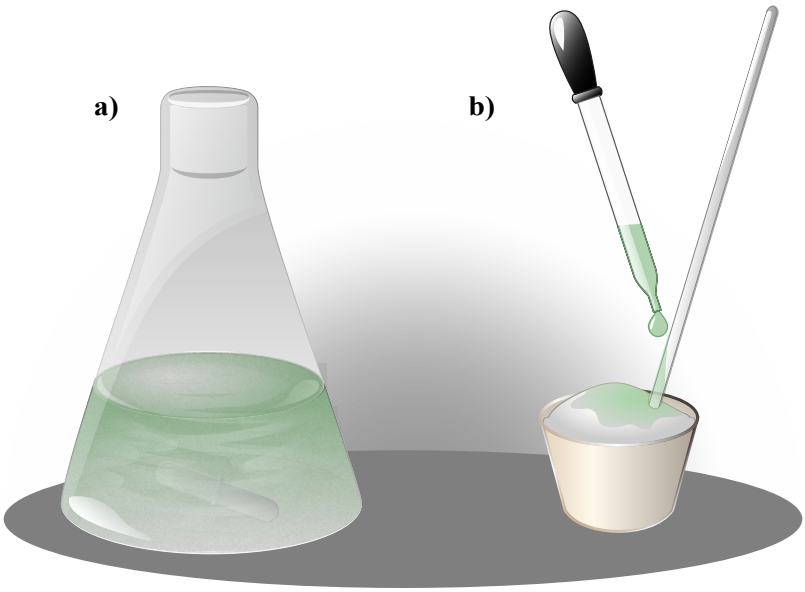

Figure 3.3: An illustration showing the difference between the two procedures of introducing rhenium. a) solution containing the support during ion-exchange b) the procedure used to perform incipient wetness impregnation.

3.6 ICP-MS

In preparation for the ICP-MS elemental analysis, 10-20 mg of samples were weighed out in a 25 mL Teflon tubes. 1.5 mL concentrated nitric acid (HNO_3) and 0.5 mL 40% hydrofluoric acid (HF) were added to decompose the samples. This solution was transferred to a 250 mL Teflon tube, and diluted with deionized water to a total volume of 216.6 mL. The diluted solution was transferred to a 16 mL teflon tube, and sent for analysis along with three blank samples, which were ultimately subtracted from the final results.

The ICP-MS elemental analysis itself was performed by Syverin Lierhagen (IKJ, NTNU), using a High Resolution Inductively Coupled Plasma ELEMENT 2 connected to a mass spectrometer.

3.7 SEM

Scanning Electron Microscopy (SEM) was performed on a Hitachi S-3400N. Samples were prepared by placing a carbon tape on a sample holder, followed by carefully adding small amounts of sample onto the tape. Air was blown at the sample holder in order to remove excess sample, followed by coating with carbon using low-vacuum sputtering. The sample holder was thereby mounted inside the Hitachi S-3400N, and the sample chamber was evacuated before starting the analysis. Medium (1.0k eV) and high magnification (5.0k eV) were used to capture the images.

3.8 Temperature programs for reduction of rhenium

Samples with rhenium loading over 1 wt.% rhenium were reduced, then stored in glass sample tubes up to three weeks prior to XAS measurements. Two different temperature programs were employed for reduction, and the difference is whether the sample was subjected to a calcination step before being reduced or not. The calcination was performed in air, where the sample was placed in a furnace and heated at a rate of 10°C min^{-1} up to 700°C, where it dwelled for 3 hours before being cooled to room temperature. Calcination is performed prior to reduction on the bulk $CoRe_4$ catalyst, and here it was performed to see what effect calcination has on the supported Re. [6]

For reduction the sample were pressed into a wafer, mortared and sieved to sizes below 212 µm. 50 mg of the sieved sample was transferred to a quartz tube reactor, with quartz wool on both sides of the sample. The tube reactor was placed in a horizontal furnace, and connected to a gas line. The gas passing through the reactor contained 75% H_2 and 25% Ar, with a feed rate of 19.43 mL min^{-1}, corrected for a 15 ml min^{-1} basis of Helium. The furnace was heated with a ramp rate of 10° min^{-1} to 600°C, where it dwelled for 2 hours. The reactor was then cooled to room temperature before collecting the reduced sample. The two different temperature programs are illustrated in Figure 3.4.

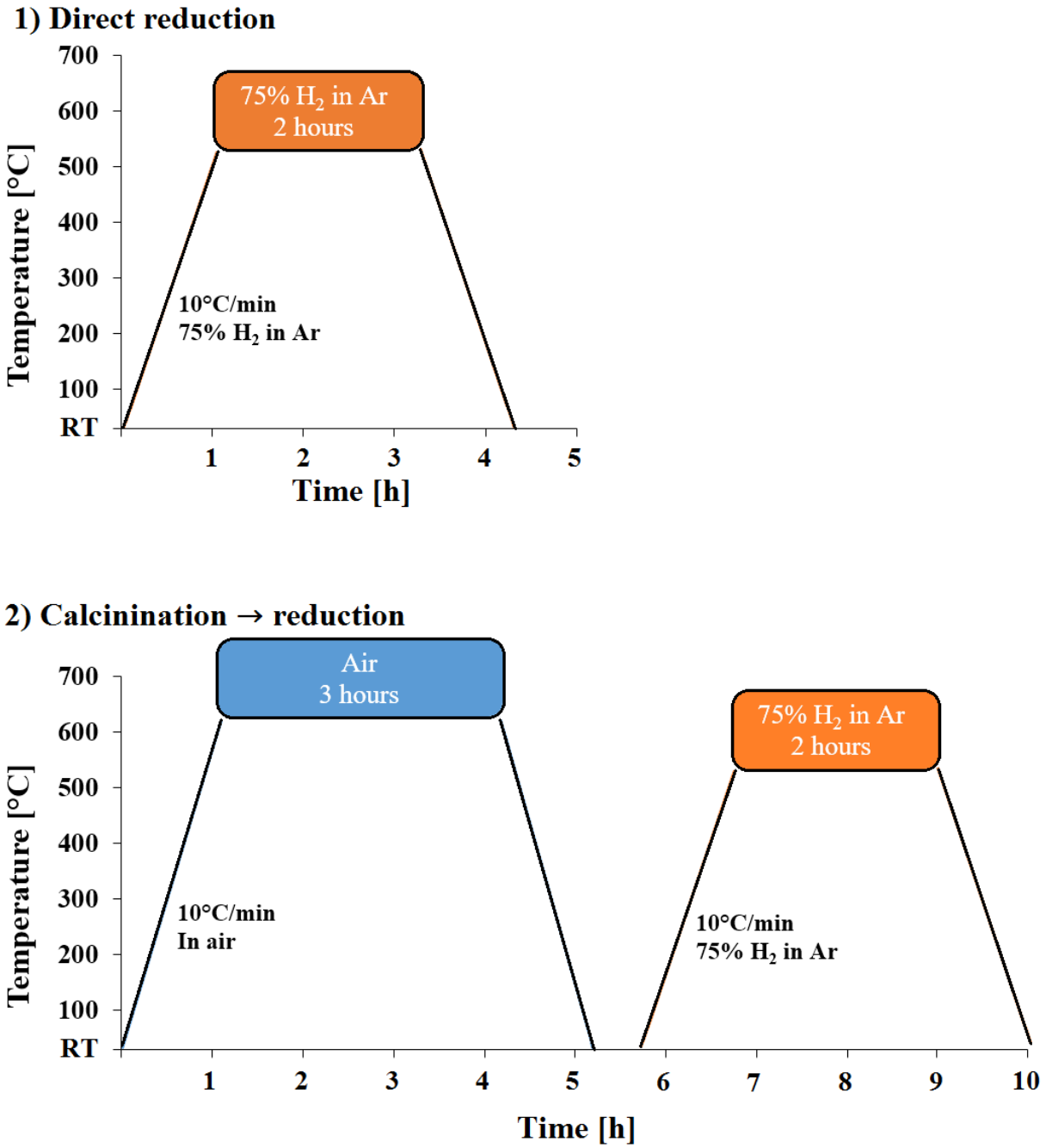

Figure 3.4: Temperature program for samples that were reduced directly, and calcined before reduction. Calcination was performed in an furnace without gas flow, while reduction was performed in tube reactor with 75% H_2 in Ar flow rate of 19.43 ml min^{-1}

After heat treatment samples were analyzed with XRD in order to detect rhenium metallic rhenium. The procedure and settings for these measurements were described in Section 3.2.

3.9 XAS

3.9.1 XAS measurements

XAS was performed at the Swiss-Norwegian Beam Lines (SNBL) at the European Synchrotron Radiation Facility (ESRF) in transmission mode. The data was collected in the multibunch filling mode with a maximum current of 200 mA, and beam energy of 6 GeV. The white beam is collected from the storage ring to the beamline by using a bending magnet. The monochromator was a Si(111) double crystal. The detectors in the beam line were mounted as seen in Figure 3.5. The incident intensity was measured in the first ion chamber I_0 and was filled with 100% N_2, while transmitted intensities in I_1 and I_2 contained a gas mixture of 60% N_2 and 40% Ar.

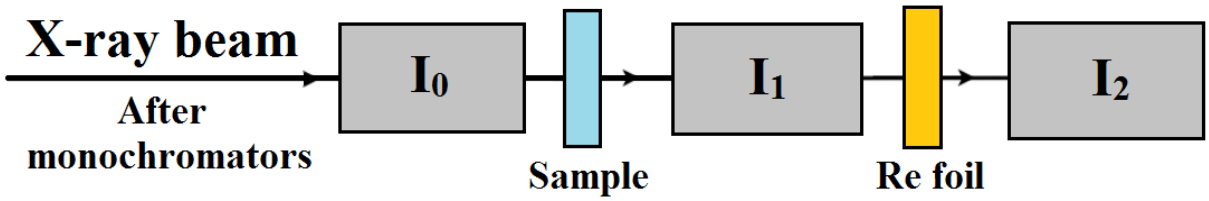

Figure 3.5: An illustration of how the X-ray moves through different samples, detectors and references.

The data was collected in transmission mode at the Re L_{III} edge, with step scans collected between 10350 eV to 11500 eV, with a step size of 0.5 eV and counting time of 200 ms. All samples and references were collected *ex situ*, and references were mixed with boron nitride for optimum absorption. The samples and references were placed in aluminum sample holders, and held in place with Kapton® tape.

3.9.2 Data analysis

The raw data was opened in the Athena software, where the background was substracted. [83] The initial data is plotted as intensity vs. energy, and the software can then transform the energy into k-space, χ(k), which can be further Fourier transformed into R-space, χ(R), with the radial distribution of the different scattering shells. The data was loaded by utilizing Equation (2.2), where I_t is the intensity in ion chamber I_1, and the incident intensity is I_0. The data was also rebinned in order to reduce the number of data points in the EXAFS region.

A k^3-weighting was used, and by observing the χ(k)-plot, the data was truncated where the curve stopped having an oscillating signal. Data points that had sudden and intense energy jumps originating from defects in the monochromator, also called glitches, were removed. After this data from the same samples were merged. For XANES the normalization range was set to 30-150 eV and for EXAFS from 150 eV to the end of the spectra.

The metallic reference for E_0 was a rhenium foil, but due to low counts the intensity of the white line is unresolved. This might be because the foil is too thick, and therefore a metallic sample was used when a white line reference was needed. The metallic sample is compared to the rhenium foil in Figure 3.6.

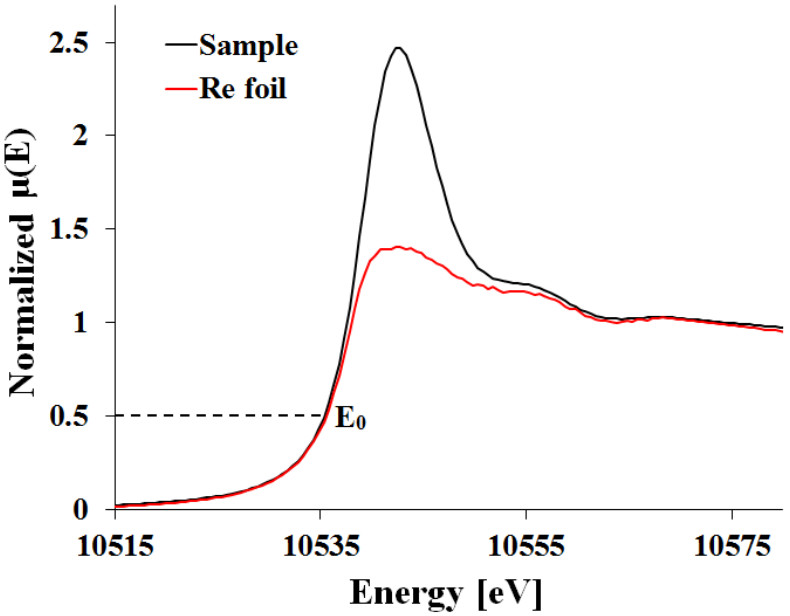

Figure 3.6: The Re-foil compared to the metallic sample which was used as a white-line reference.

For the Re(VII) reference it would be natural to use Re_2O_7, as that was the rhenium precursor in the introduction experiments. However, $KReO_4$ was used in XANES as it had the best resemblance with samples containing rhenium oxide.

The E_0 was set to 0.5 up the normalized μ(E) for all samples and references, after the normalization for both XANES and EXAFS. The energy correction was performed by correcting the rhenium foil to an E_0 of 10535 eV. Three different methods were used in an attempt to extract quantitative data from the XANES. The two first methods rely on a metallic and Re(VII) reference, which was the metallic sample and $KReO_4$, in order to determine the reduced fraction, F_{red} of rhenium in the samples. The third method was least squares linear combination, where the references were the metallic sample, ReO_3 and $KReO_4$. The three methods used in an attempt to determine the reduced fraction of rhenium are summarized below:

- **E_0 value.** The E_0 of the sample was compared to the E_0 of the two references. The reduced fraction was calculated by using the following equation:

$$F_{red} = \frac{E_{0,\text{sample}} - E_{0,\text{ metallic}}}{E_{0,KReO_4} - E_{0,\text{ metallic}}} \tag{3.1}$$

- **Energy at top of the white.** Similar to the previous method, but the energy at the top of the white line was used instead of E_0, and was calculated by the following equation:

$$F_{red} = \frac{E_{\text{Top, sample}} - E_{\text{Top, metallic}}}{E_{\text{Top, }KReO_4} - E_{\text{Top, metallic}}} \tag{3.2}$$

- **Linear combination.** The Athena software uses a least-square linear combination of the XANES of two or more references, and calculates how much each reference must contribute to form the best fit with the sample. A maximum of 3 references were used. The fit was performed 5 eV below the absorption edge of the sample, and 35 eV past it. E_0 was allowed be fitted, but only within $\pm$ 2 eV of the previously determined E_0 value. The goodness of fit was reported as R = Σ(data-fit)^2/ Σ(data)^2. The reduced fraction equaled to the fraction the metallic sample contributed to the fit.

To analyze the EXAFS data the χ^{exp}(k) from Athena was exported to the DL_EXCURVE software. [84] This software refines the EXAFS data by generating a theoretical χ^{th}(k) which is fitted to the experimental χ^{exp}(k)-curve from Athena by the use a least squares refinement. For calculations the software applies the curved wave theory, ab initio phase-shifts and backscattering amplitude for the atoms defined by the user. k^3-weighting was used, with k-space range (Δk) starting at 4 $Å^{-1}$ for all samples, and ending at values between 10 and 16 $Å^{-1}$, depending on the quality of signal.

The EXAFS reference compound for Re(0) and Re(VII) was the rhenium foil and NH_4ReO_4 respectively. The two references have known multiplicities (N) that were kept constant, while the Debye Waller factor ($2\sigma^2$), coordination shell distance (R), Fermi Energy (E_F), which is a correction factor for E_0 from Athena, were refined. The amplitude reduction factor (AFAC, S_0^2) was refined by itself. These two refinements were alternated until they converged at stable values.

For the samples $2\sigma^2$, N, R and E_F were refined. The AFAC-value was not refined for the samples, but transferred from the reference it resembled the most. This was determined by utilizing the reduced fraction extracted from the XANES. The AFAC value for the rhenium foil was used if the reduced fraction was over 0.5, while the AFAC value for NH_4ReO_4 was used if it was under 0.5.

Chapter 4

Results

4.1 XRD

In this section the results from the powder X-ray diffraction was used to determine the crystalline phase(s) of the synthesized zeotypes. The detection of crystalline phases of rhenium will be presented later. In the diffractograms the samples will have the suffix ”U” for as-synthesized and ”C” for calcined.

4.1.1 AlPO-34 and SAPO-34

SAPO-34 and AlPO-34 without HF addition should yield the same diffraction pattern as CHA, as shown in Figure 2.6a, while AlPO-34 with HF should yield triclinic CHA as shown in Figure 2.6b.

SAPO-34 and AlPO-34 with one SDA

The diffractograms of all calcined SAPO-34 synthesized with TEAOH as SDA are shown in Figure 4.1, while the as-synthesized results are in the appendix, Figure A.1. All samples are phase pure as their diffractogram correspond to CHA, but the SAPO-34/4C sample with theoretical Si/Al ratio of 0.9 has very low intensity peaks compared to the others, likely due to high silicon content. The results are summarized in Table 4.1.

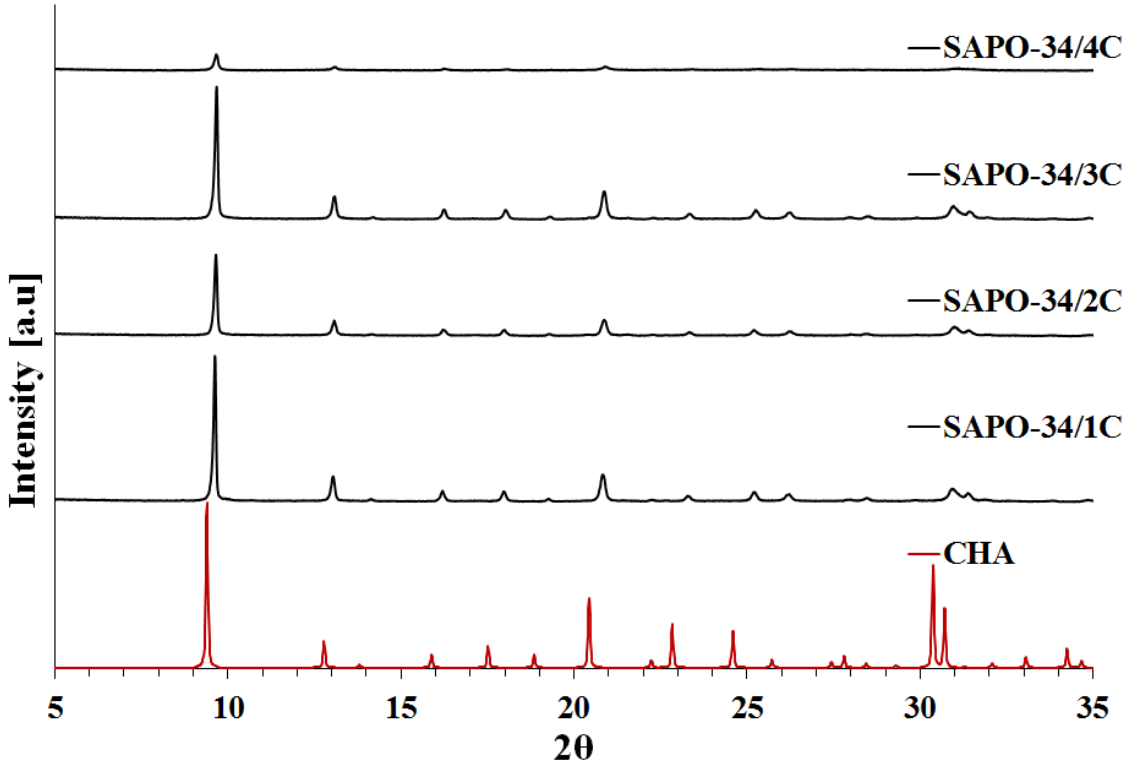

Figure 4.1: XRD diffractogram of calcined (C) SAPO-34 samples synthesized with TEAOH as SDA.

Table 4.1: XRD results of SAPO-34 samples, using TEAOH as SDA. All samples were crystallized for 72 hours at 190°C.

Sample name	Theoretical Si/Al	Topology	Phase-pure
SAPO-34/1	0.2	CHA	✓
SAPO-34/2	0.3	CHA	✓
SAPO-34/3	0.4	CHA	✓
SAPO-34/4	0.9	CHA	✓

From the diffractograms in Figure 4.2 it is evident that AlPO-34/1U and ALPO-34/1C are amorphous, and that 3 days of crystallization time was not enough for it to crystallize. AlPO-34/2 with crystallization time of 7 days resulted in a crystalline product. The most intense peak in the CHA diffractogram is found around 9.4 2θ and is also detected in this sample, but other AlPO zeotypes also have their most intense peak around 9.4 2θ, e.g. AlPO-18 (AEI) and AlPO-52 (AFT). [44] As some peaks corresponding to CHA appear to be missing, and impurities are present, it is not phase-pure CHA. The presence of several crystalline phases makes it difficult to distinguish and identify them. The results are summarized in Table 4.2.

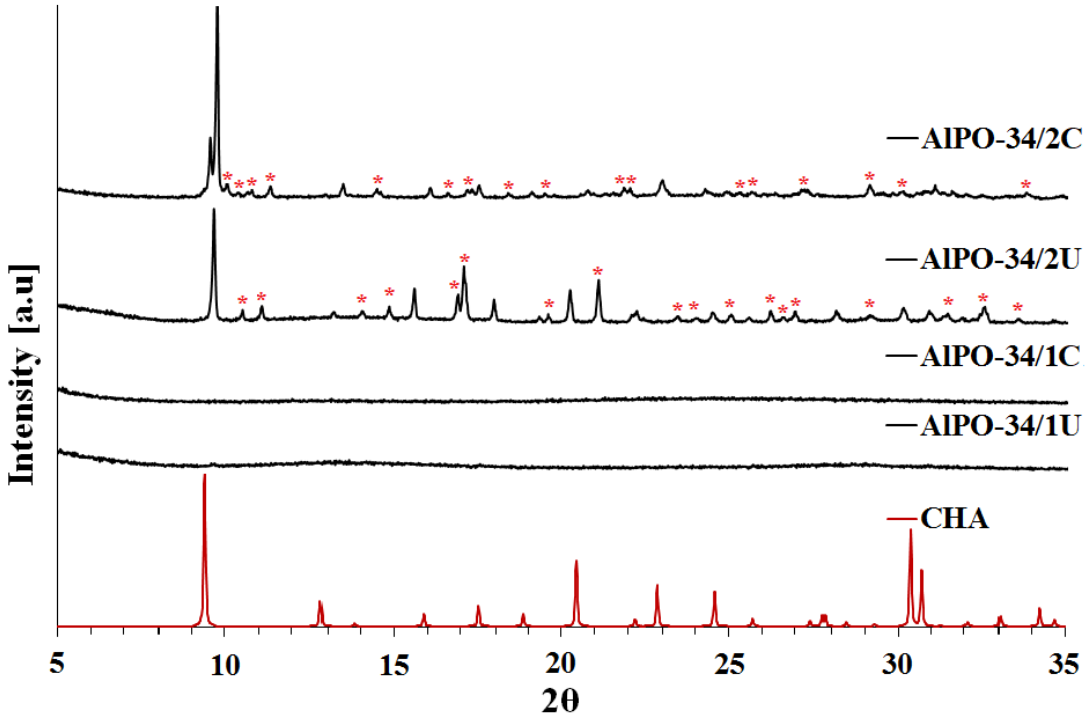

Figure 4.2: XRD diffractogram of as-synthesized (U) and calcined (C) AlPO-34 samples synthesized with TEAOH as SDA. Red asterisks indicate peaks not originating from CHA. "Unknown mix" implies the presence of several different phases which are hard to distinguish.

Table 4.2: XRD results of AlPO-34 samples, using TEAOH as SDA. All samples were crystallized at 190°C for the specified amount of time. "Unknown mix" implies the presence of several different phases which are hard to distinguish.

Sample name	Cryst. time [h]	Topology	Phase-pure
AlPO-34/1	72	Amorphous	X
AlPO-34/2	168	CHA + unknown mix	X

AlPO-34 with three SDAs

The diffractograms of AlPO-34 samples synthesized with the three SDAs TEAOH, TEA and Mor are shown in Figure 4.3. These results are similar to AlPO-34/2, where peaks corresponding to CHA can be found, but with a few also missing. Many different phases appear to be present in these samples as well, thus distinguishing them is difficult. AlPO-34/3 had 24 hours of crystallization and AlPO-34/4 132 hours, still none of these seemed to favour the formation of phase-pure CHA. The results are summarized in Table 4.3.

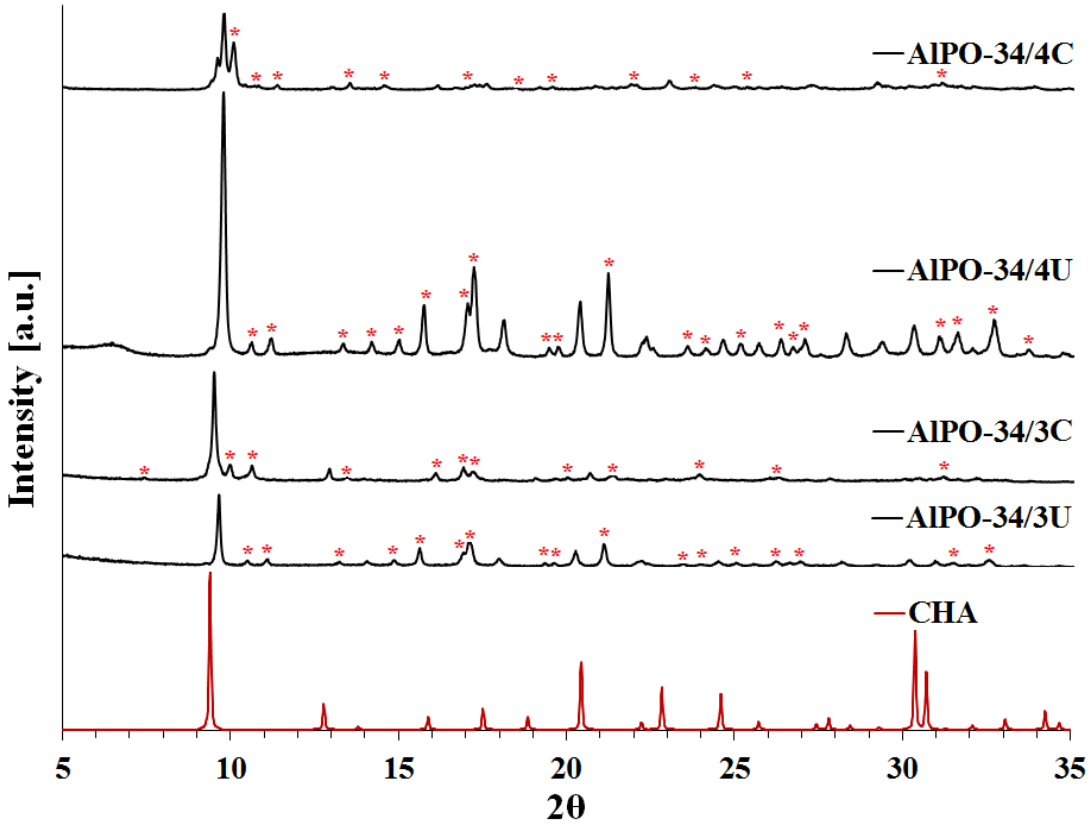

Figure 4.3: XRD diffractogram of as-synthesized (U) and calcined (C) AlPO-34 samples using 3 SDAs. Red asterisks indicate peaks not corresponding to CHA.

Table 4.3: XRD results of AlPO-34 samples using TEAOH, TEA and Mor as SDAs. All samples were crystallized at 190°C for the specified amount of time. ”Unknown mix” implies the presence of several different phases which are hard to distinguish.

Sample name	Cryst. time [h]	Topology	Phase-pure
AlPO-34/3	24	Unknown mix	X
AlPO-34/4	132	Unknown mix	X

AlPO-34 with four SDAs

The diffractogram of AlPO-34 samples synthesized with the use of the four SDAs TEAOH, TEA, DEA and Mor are shown in Figure 4.4. All diffractograms seem to contain mostly AFI, which is not the goal in these syntheses, but as it is the major phase, the peaks not originating from AFI will be indicated with red asterisks in this figure. The diffractogram of the as-synthesized samples are found in the appendix, Figure A.2.

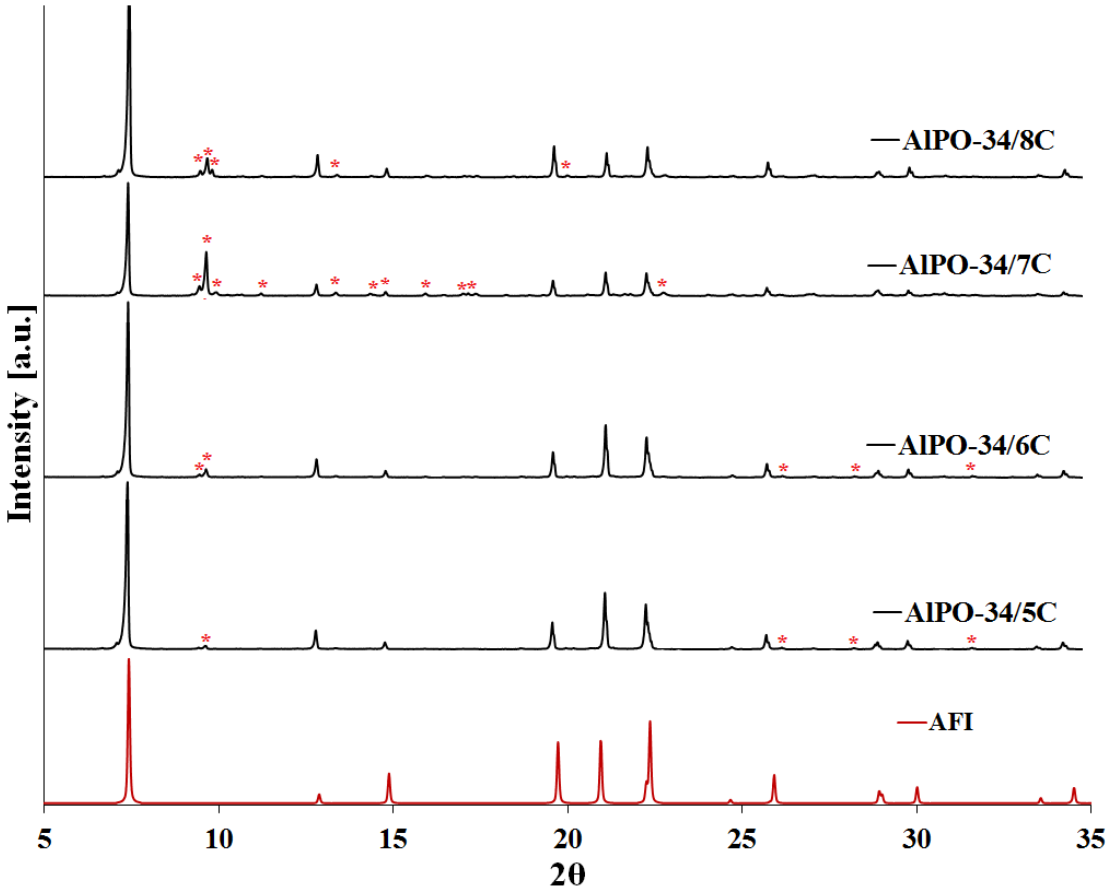

Figure 4.4: XRD diffractogram of as-synthesized (U) and calcined (C) AlPO-34 samples using 4 SDAs. Red asterisks indicate peaks not corresponding to AFI.

In addition to AFI there are some peaks corresponding to CHA, but the intensity of the peaks are very low. Especially in AlPO-34/7 there appears to be several other phases than AFI and CHA present. The goal of these experiments was to vary crystallization time in order to favour formation of CHA. The crystallization time was varied over a relatively large interval, but as very little CHA was detected this does not seem to be a route worth pursuing with this procedure. The results are summarized in Table 4.4.

Table 4.4: XRD results of AlPO-34 samples using TEAOH, TEA , DEA and Mor as SDAs. All samples were crystallized at 190°C for the specified amount of time. "Unknown mix" implies the presence of several different phases which are hard to distinguish.

Sample name	Cryst. time [h]	Topology	Phase-pure
AlPO-34/5	14	AFI+CHA	X
AlPO-34/6	24	AFI+CHA+Unknown mix	X
AlPO-34/7	96	AFI+CHA+Unknown mix	X
AlPO-34/8	168	AFI+CHA	X

AlPO-34 with hydrofluoric acid or ethylene glycol

The diffractogram of both calcined AlPO-34 with HF and calcined AlPO-34 with EG are shown in Figure 4.5, while the as-synthesized samples are shown in the appendix, Figure A.3.

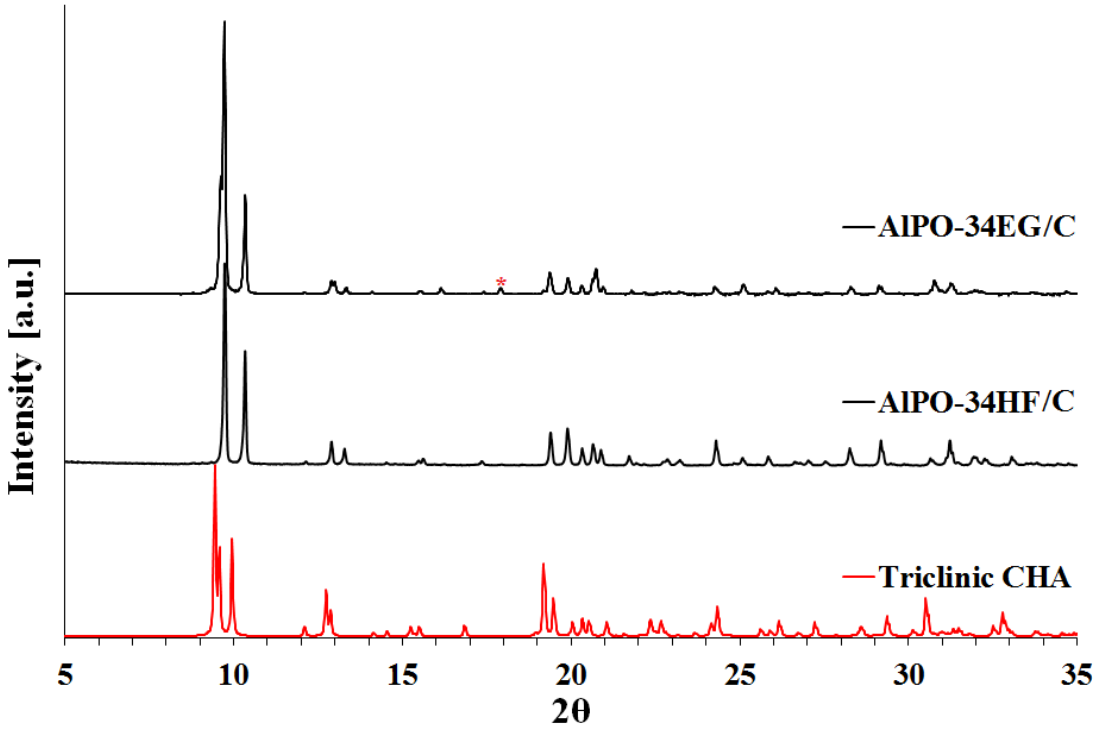

Figure 4.5: XRD diffractogram of calcined (C) AlPO-34 with HF and AlPO-34 with EG. Red asterisks indicate peaks not originating from triclinic CHA.

Both samples have a shift of roughly 0.5 2θ compared to that of triclinic CHA. AlPO-34EG/C contains one impurity peak, but otherwise the peaks for both samples correspond to the reference. The results are summarized in Table 4.5.

Table 4.5: XRD results of AlPO-34 samples with addition of HF or EG.

Sample name	Cryst. time [h]	Cryst. temp [°C]	Topology	Phase-pure
AlPO-34HF	192	190	tri-CHA	✓
AlPO-34EG	120	185	tri-CHA	✓

4.1.2 AlPO-5 and SAPO-5

In Figure 4.6 AFI and a secondary phase can be observed for AlPO-5/1C with 48 hours of crystallization time. This appears to be the dense phase T-$AlPO_4$, an AlPO analogue of the silica polymorph tridymite. [85] When the crystallization time was increased to 72 hours AlPO-34/2C, this phase was not present, and the result was phase-pure AFI. SAPO-5/1C with 48 hours of crystallization time was also phase-pure. Here, only the calcined samples are shown. The diffractogram of the as-synthesized AlPO-5 and SAPO-5 are shown in the appendix, Figure A.4

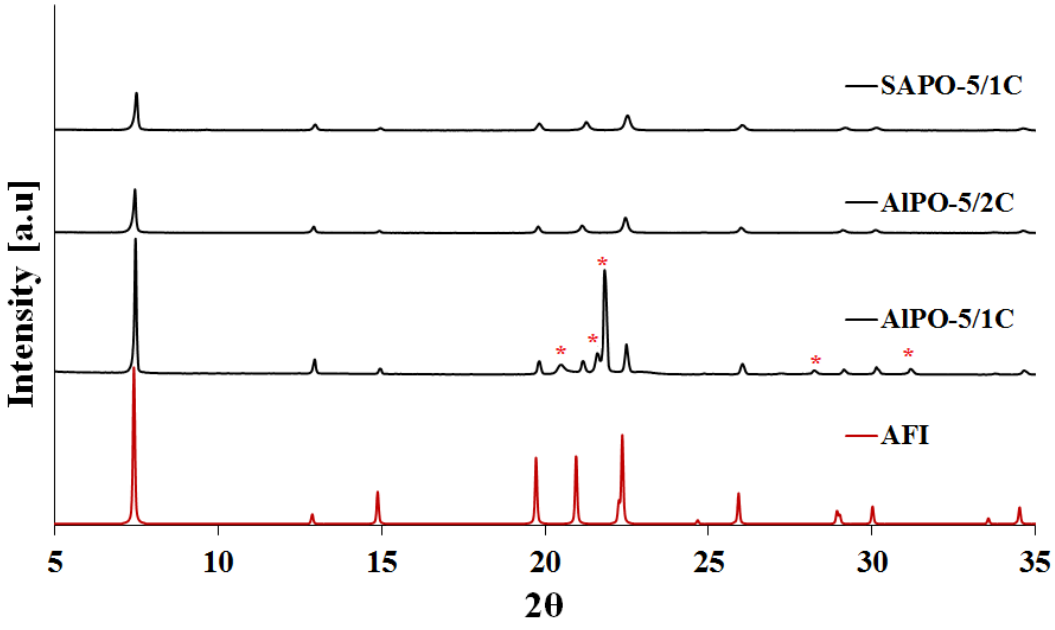

Figure 4.6: Diffraction pattern of calcined (C) AlPO-5 and SAPO-5. Red asterisks indicate peaks that do not originate from AFI.

A summary of all the synthesized zeotypes are listed in Table 4.6.

Table 4.6: Summary of XRD results for all zeotypes. Listed are short synthesis descriptions, crystallization times, topologies and evaluation of phase purities. ”Unknown mix” implies the presence of phases which are difficult to distinguish.

Sample name	Synthesis description	Crystallization time [h]	Topology	Phase-pure ✓/X
SAPO-34/1	1 SDA	72	CHA	✓
SAPO-34/2	1 SDA	72	CHA	✓
SAPO-34/3	1 SDA	72	CHA	✓
SAPO-34/4	1 SDA	72	CHA	✓
AlPO-34/1	1 SDA	72	Amorphous	X
AlPO-34/2	1 SDA	168	CHA+Unknown mix	X
AlPO-34/3	3 SDA	24	Unknown mix	X
AlPO-34/4	3 SDA	132	Unknown mix	X
AlPO-34/5	4 SDA	14	AFI+CHA	X
AlPO-34/6	4 SDA	24	AFI+CHA+Unknown mix	X
AlPO-34/7	4 SDA	96	AFI+CHA+Unknown mix	X
AlPO-34/8	4 SDA	168	AFI+CHA	X
AlPO-34HF	HF added	192	tri-CHA	✓
AlPO-34EG	EG added	120	tri-CHA	✓
SAPO-5/1	1 SDA	48	AFI	✓
AlPO-5/1	1 SDA	48	AFI + T-$AlPO_4$	X
AlPO-5/2	1 SDA	72	AFI	✓

4.2 Surface area measurements

All the SBA-15 samples and a selection of the phase-pure zeotypes samples had their surface area measured. Figure 4.7 illustrates the BET surface area and t-plot micropore area for these samples.

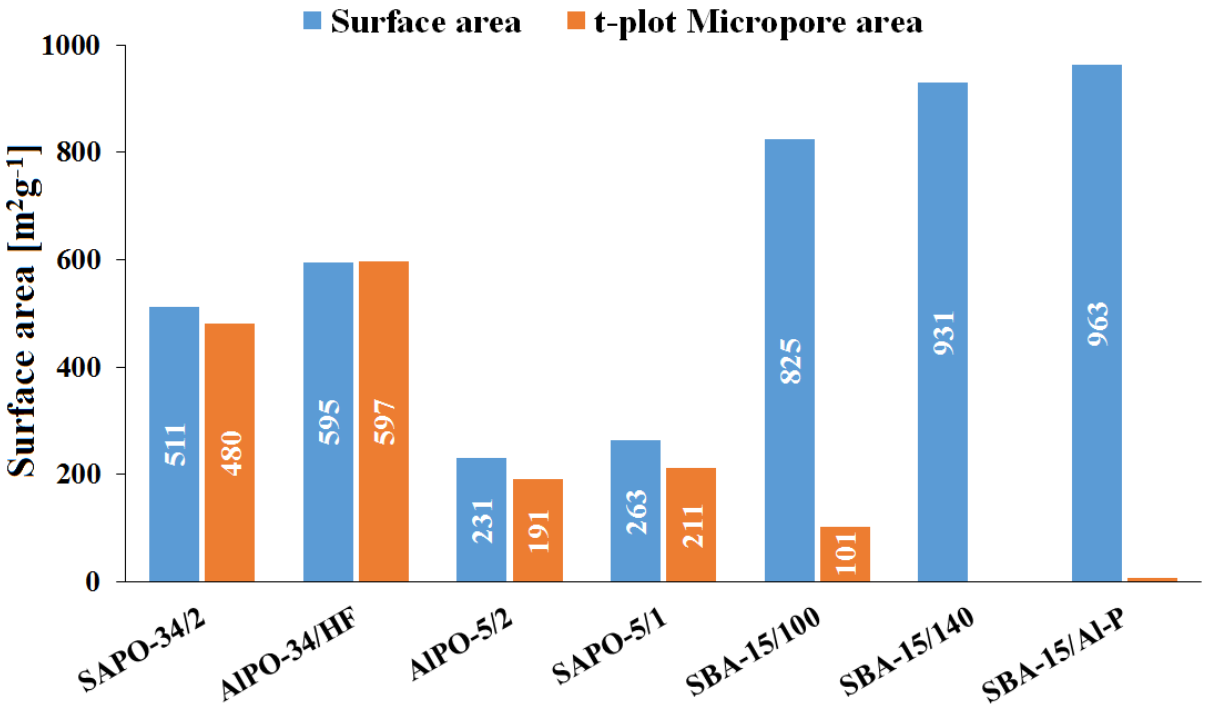

Figure 4.7: Surface areas and t-plot micropore area of selected supports calculated from the BET isotherm. No t-plot micropore area could be calculated for SBA-15/140.

The SAPO-34 and AlPO-34 are within the surface area range reported in literature, which is between 400 and 700 m^2g^{-1} [36]. AlPO-5/2 and SAPO-5/1 have a slightly lower surface area than reported in literature, which is ranging from 300 to 400 m^2g^{-1}. [51] For the zeotypes the t-plot micropore area is similar to the BET surface area, which indicates that most of the measured surface area is microporous, as expected. All the SBA-15 samples have surface areas within the reported values of 600-1050 m^2g^{-1} in literature. [39]

4.2.1 BET and BJH measurements for SBA-15

As low-angle XRD was not available for characterizing the SBA-15 samples, BET and BJH measurements were used to determine if the pores had sensible surface areas and pore size distributions. The criteria for SBA-15 are a type IV BET isotherm, type H1 hysteresis and a narrow pore distribution. [39] The SBA-15/100 sample will not be shown here as it did not meet any of these criteria, but the BET isotherm and pore distribution are found in the appendix, Figure B.1.

The BET isotherm of SBA-15/140 in Figure 4.8 has a type IV BET isotherm and a type H1 hysteresis, both which meet the criteria of SBA-15. The pore distribution is rather narrow and peaks at 72 Å, but due to the presence of some smaller mesopores the average pore size was calculated to 53 Å. The BET surface area of 931 m^2g^{-1} is in the high end of what is reported in literature. [39] Considering the previously stated criteria for the surface area measurements of SBA-15, this sample was deemed successful, and was therefore used in further experiments.

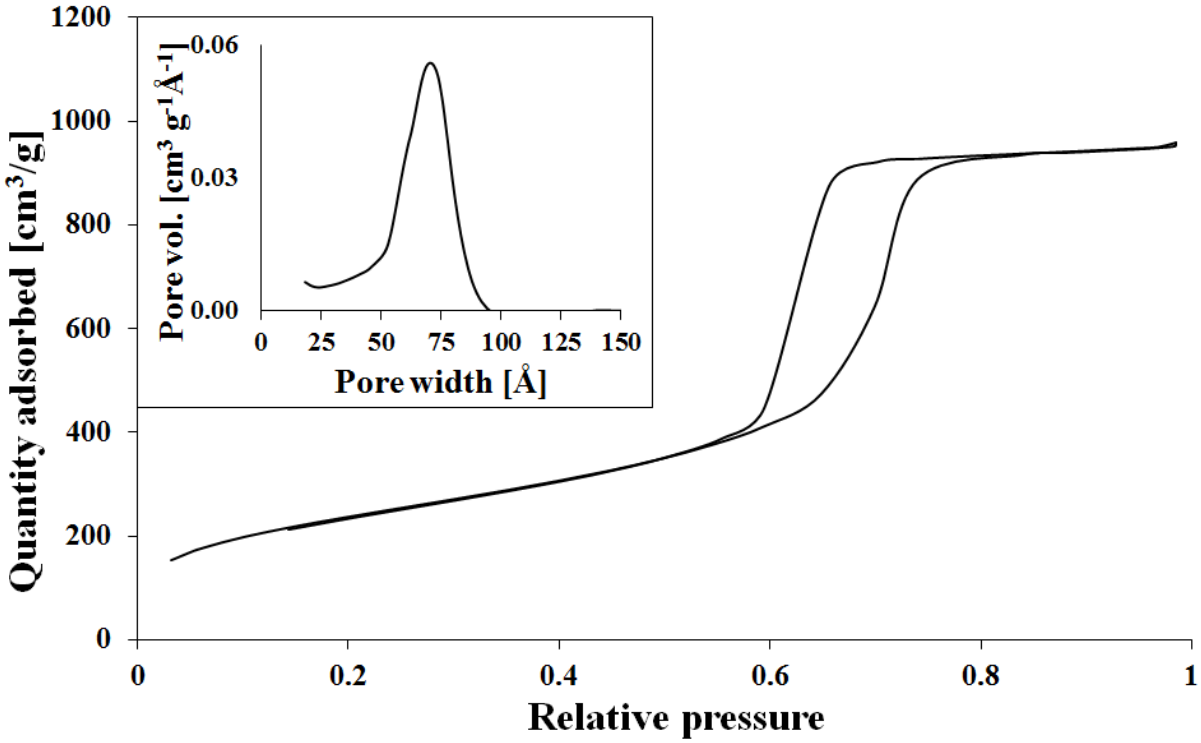

Figure 4.8: BET isotherm and pore distribution from BJH of SBA-15/140.

The BET isotherm of SBA-15/Al-P in Figure 4.9 is reminiscent of a type IV isotherm. The hysteresis appears to be a mixture of type H1 and H4, indicating a mixture of micro- and mesopores. This is supported by the broad pore distribution, which shows a peak at 90 Å, but a rising edge into the micropore domain. As a broad pore size distribution will make it difficult to assess the the success of growth limitations if rhenium were to be introduced, this sample was not used in further experiments.

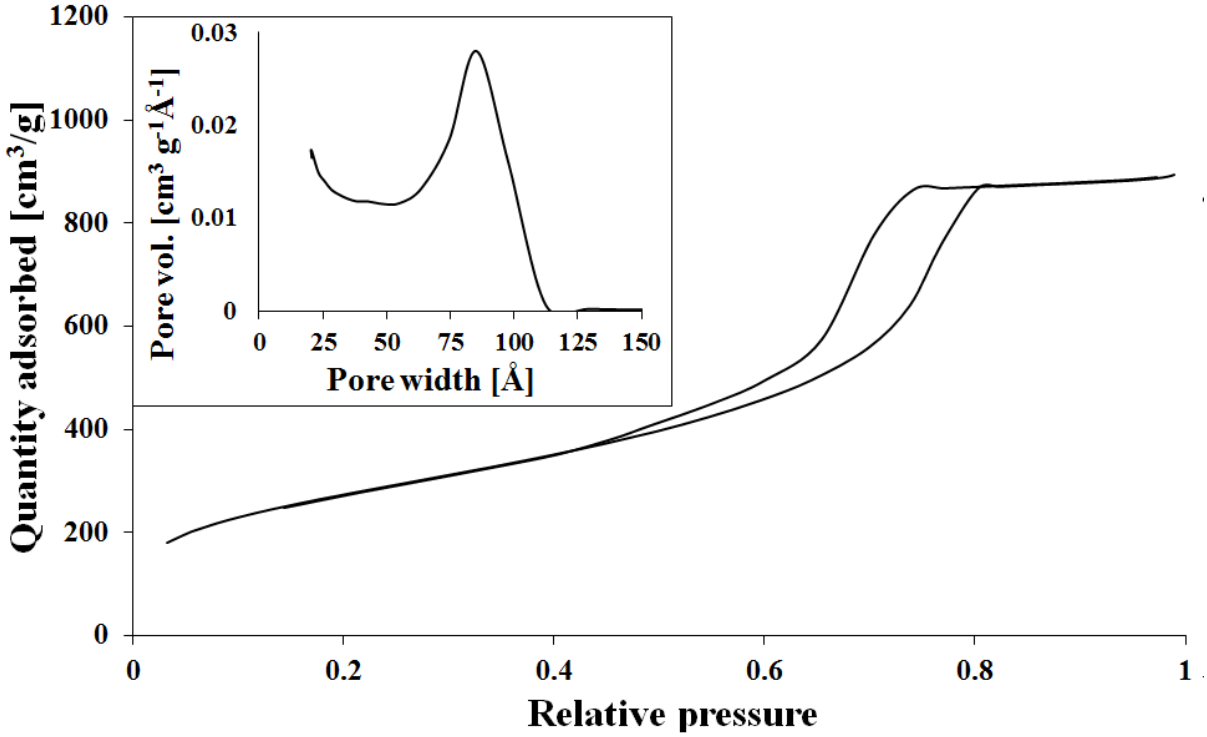

Figure 4.9: BET isotherm and pore distribution from BJH of SBA-15/Al-P.

The different SBA-15 samples that were synthesized and analyzed with BET/BJH are summarized in Table 4.7.

Table 4.7: Summary of surface area measurements of the SBA-15 samples, and evaluation of whether the criteria for the SBA-15 pore system were met.

Sample name	Description	Cryst. temp [°C]	BET surface area [m^2g^{-1}]	Pore width [a] [Å]	Criteria met
SBA-15/100	Conventional	100	825	29 Å	X
SBA-15/140	Conventional	140	931	53 Å	✓
SBA-15/Al-P	Halide-free	90	963	55 Å	X

[a] Average pore width calculated by BJH adsorption pore width (4V/A).

4.3 DRIFTS

The SBA-15/Al-P sample could potentially have Brønsted acidity if aluminum was incorporated into the silica network. In that case, OH-stretching from an OH-group attached to a silicon and an aluminum (Si-OH-Al) should be the detected, and if not, only OH-stretching from silanols (-Si-OH) should be present. In Figure 4.10 the DRIFTS spectrum of SBA-15/Al-P is shown, where the only silanols, around 3750 cm^{-1}, could be detected. This indicates that there are is no Brønsted acidity, and that aluminum was not incorporated into the structure.

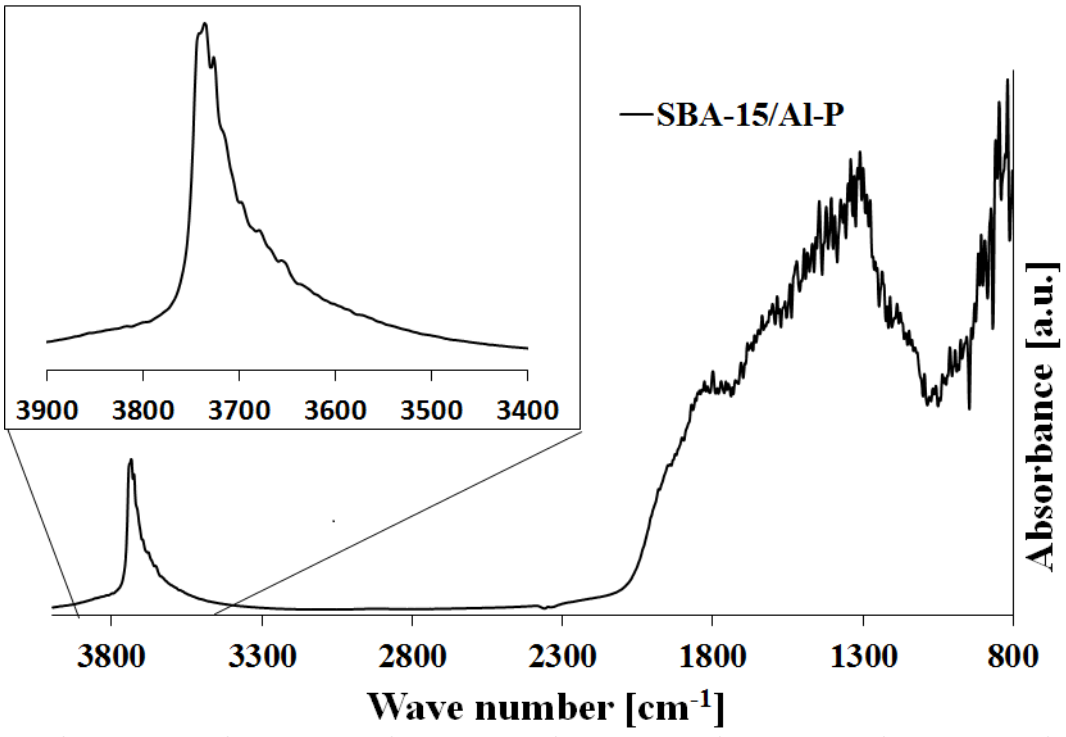

Figure 4.10: DRIFTS spectrum of SBA-15/Al-P at 550°C in synthetic air.

4.4 ICP-MS

The elemental compositions of selected calcined and phase-pure supports that were ultimately used for metal introduction are found in Table 4.8. Based on the the theoretical Si/Al ratios of 0.3 and 0.2 for SAPO-34/2 and SAPO-5/1 respectively, the measured Si/Al ratios are slightly lower. For the AlPO-34HF and AlPO-5/3 no Si was added during the syntheses and its presence must therefore be due to contaminants.

Table 4.8: Elemental composition of calcined porous supports that were used for metal introduction, along with theoretical and analyzed Si/Al molar ratios for the zeotypes.

Sample name	Al [wt.%]	P [wt.%]	Si [wt.%]	Theoretical Si/Al ratio	Actual Si/Al ratio
SAPO-34/2	17.24	17.09	4.413	0.30	0.24
AlPO-34HF	19.19	23.76	0.133	0.00	0.01
SAPO-5/1	18.42	21.51	2.380	0.20	0.13
AlPO-5/3	17.61	21.96	0.127	0.00	0.01
SBA-15/140	0.008	0.003	46.41	-	-

Ion-exchange with water as solvent

The Re loading after the ion-exchange procedures performed in water on as-synthesized and calcined SAPO-34/2 are listed in Table 4.9. These loadings are very low, and both methods are unsuccessful at introducing sufficient amounts of rhenium.

Table 4.9: Re content after ion-exchange in 0.1 M Re-solution with 0.3 g as-synthesized and calcined SAPO-34/2.

Support	Re [wt.%]
As-synthesized SAPO-34/2	0.004
Calcined SAPO-34/2	0.010

Partial calcination

The Re content after ion-exchange in water on the partially calcined samples are shown in Table 4.10. As with the as-synthesized and calcined samples, these samples have very low loadings of rhenium. The SAPO-34 samples were fully calcined after the ion-exchange, in order to remove the SDAs, which might have lead to loss of rhenium. The SBA-15 sample was not calcined after ion-exchange, but this did not result in an improved loading compared to the SAPO-34 samples shown here.

Table 4.10: Re content after 0.4 g SAPO-34/2 and SBA-15/140 had been partially calcined at different temperatures before being ion-exchanged with 25 mL 0.03 M Re solution. The SAPO-34/2 samples were then calcined for 6 hours at 550 °C to completely remove SDAs before elemental composition analysis.

Support	Partial calcination temperature [°C]	Re [wt.%]
SAPO-34/2	200	0.003
SAPO-34/2	300	0.001
SAPO-34/2	400	0.001
SAPO-34/2	500	0.002
SBA-15/140	350	0.001

Ion-exchange with ethanol and acetone as solvent

For SAPO-34 with ethanol and acetone as solvent, the concentration of the rhenium solution and stirring time was varied. The stirring time was varied in order to see if these solvents required longer diffusion times, but as seen in Figure 4.11 this does not seem to affect the loading particularly. With ethanol as solvent, the uptake increased along with increase in concentration, but with acetone as solvent this was not the case.

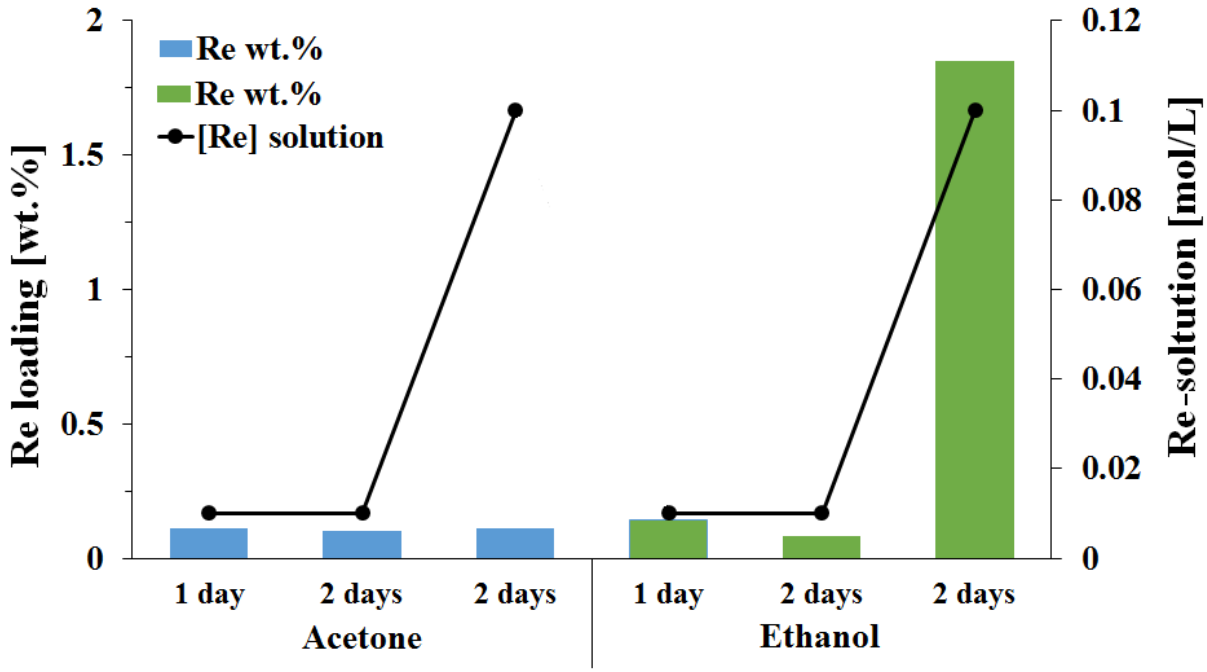

Figure 4.11: SAPO-34/2 ion-exchanged with a acetone- or ethanol-rhenium solutions of 0.01M or 0.1 M. In all experiments 0.3 g calcined SAPO-34 were added and stirred for 1 or 2 days.

Based on the relatively good uptake of rhenium when using ethanol as solvent, the procedure was performed on the other supports as well. All experiments in Figure 4.12 used 0.3 g support and 0.1 M Re ethanol solution. However, none of the other supports achieved rhenium uptake close to that of SAPO-34. AlPO-5 and SAPO-5 approached 0.2 wt% Re, but this is relatively far from the desired loading of 1.0 wt.% rhenium.

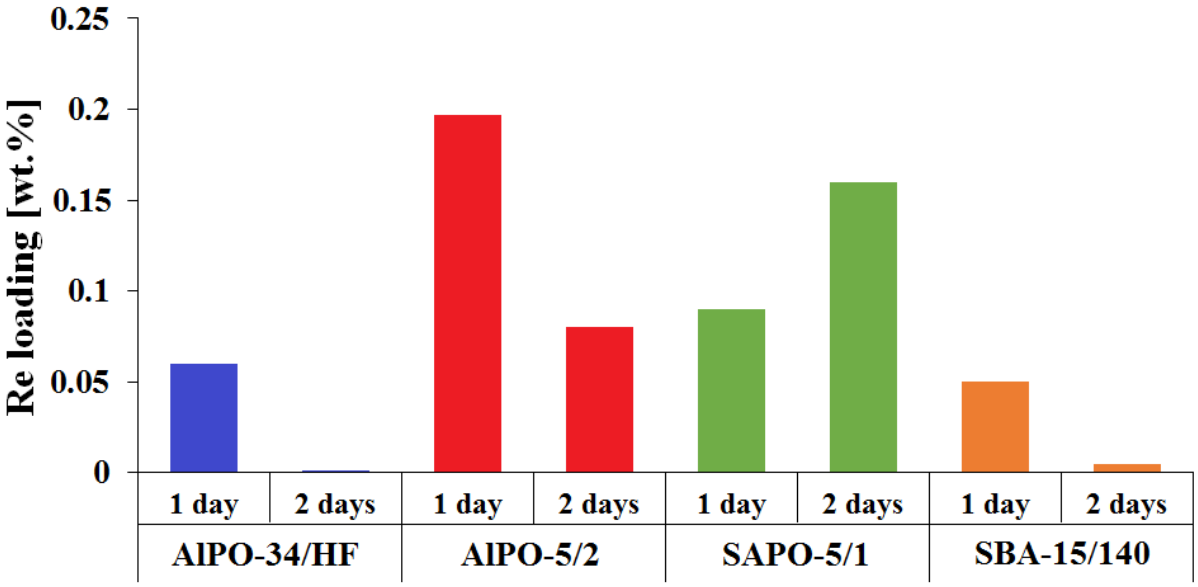

Figure 4.12: Different porous supports ion-exchanged in ethanol. In all experiments 0.3 g support was stirred in 20 mL 0.1 M ethanol-rhenium solution for 1 or 2 days

Incipient Wetness

Due to time limitations prior to the XAS analysis the incipient wetness method was only performed on three supports: SAPO-34, SAPO-5 and SBA-15. This resulted in a support from each of the three different pore systems, but no neutral analogies for the zeotypes. Based on the amount of rhenium added and the amount of support that was impregnated in the experiment, the introduced amount of rhenium was calculated to be 3.0 wt.%. In Figure 4.13 the rhenium loadings from the ICP-MS are illustrated, where all samples have a slightly lower loading than expected.

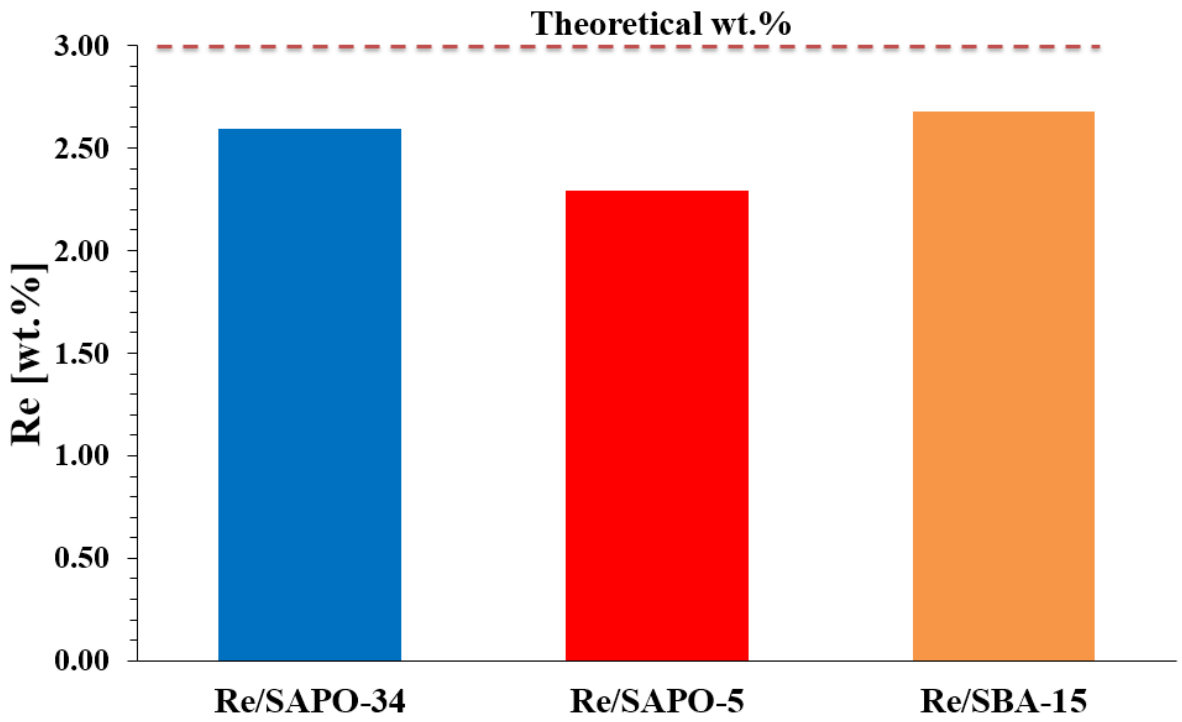

Figure 4.13: Rhenium content in supports with rhenium introduced through the incipient wetness method. The theoretical wt.% based on the experiment is illustrated with the dashed line.

The samples with a rhenium loading over 1.0 wt.% will be renamed for the rest of this thesis. First, the as prepared samples, which means that rhenium has been introduced but no heat treatment has been performed, will be given new names. The names are listed in Table 4.11, which contains information of support material, the method of introduction and the resulting rhenium loading as measured by ICP-MS.

Table 4.11: New names of as prepared samples, along with the original name of the support, rhenium introduction method and resulting rhenium loading.

New name	Support name	Introduction method	Re loading [wt.%]
Re:SAPO-34/AP_1.9	SAPO-34/2	Ion-exchange in ethanol (0.1M, 2 days)	1.9
Re/SAPO-34/AP_2.6	SAPO-34/2	Incipient wetness	2.6
Re/SAPO-5/AP_2.3	SAPO-5/1	Incipient wetness	2.3
Re/SBA-15/AP_2.7	SBA-15/140	Incipient wetness	2.7

Effect of heat treatment on rhenium loading

There were two approaches for reduction of the rhenium: direct reduction or calcination followed by reduction. The rhenium content for as prepared (AP), after direct reduction (R), calcination (C) and calcination followed by reduction (CR) samples are illustrated in Figure 4.14.

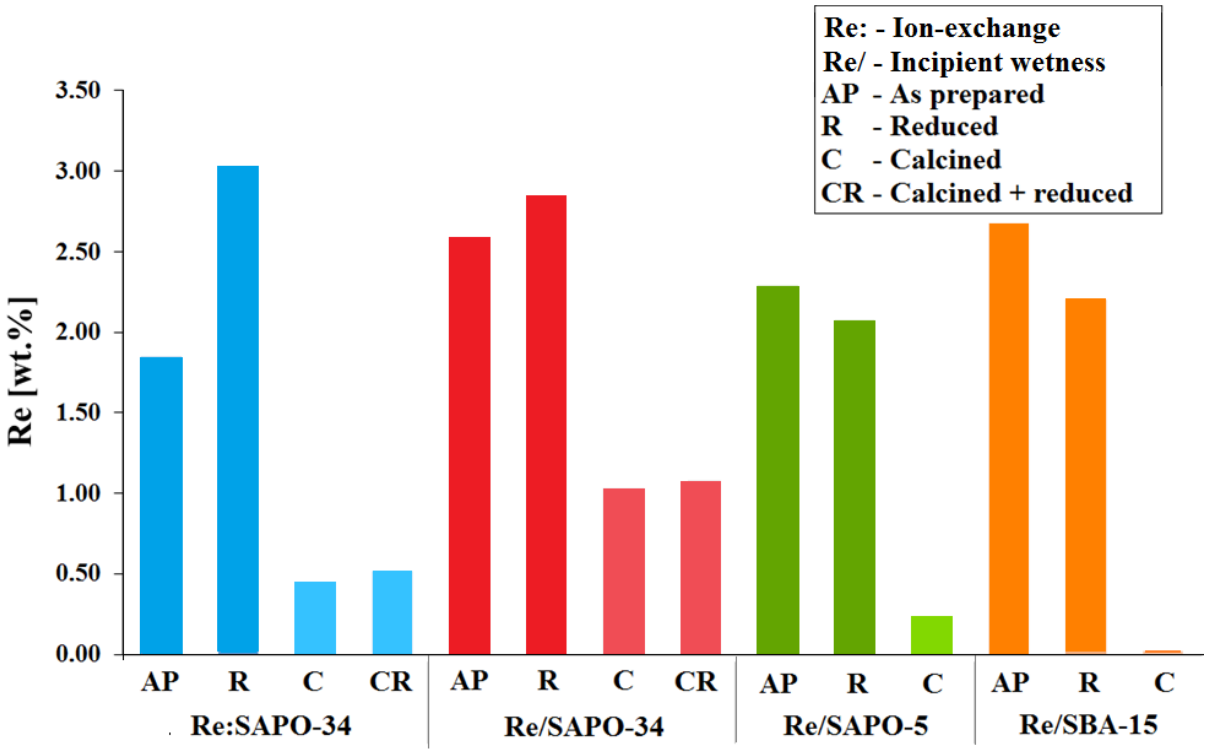

Figure 4.14: Rhenium content in supports with samples being as prepared, directly reduced, calcined and calcined followed by reduction.

In Figure 4.14 it is apparent that there is a large mass loss of rhenium when the samples are calcined. The mass loss percentage of rhenium due to calcination was calculated by:

$$\text{Re loss} = \frac{\text{wt.\% Re Calcined sample}}{\text{wt.\% Re Directly reduced sample}} \times 100\% \tag{4.1}$$

The rhenium content of the calcined sample, and not calcined then reduced, was used as basis of mass loss, as the calcination had been performed for all samples. The resulting rhenium mass losses are illustrated in Figure 4.15.

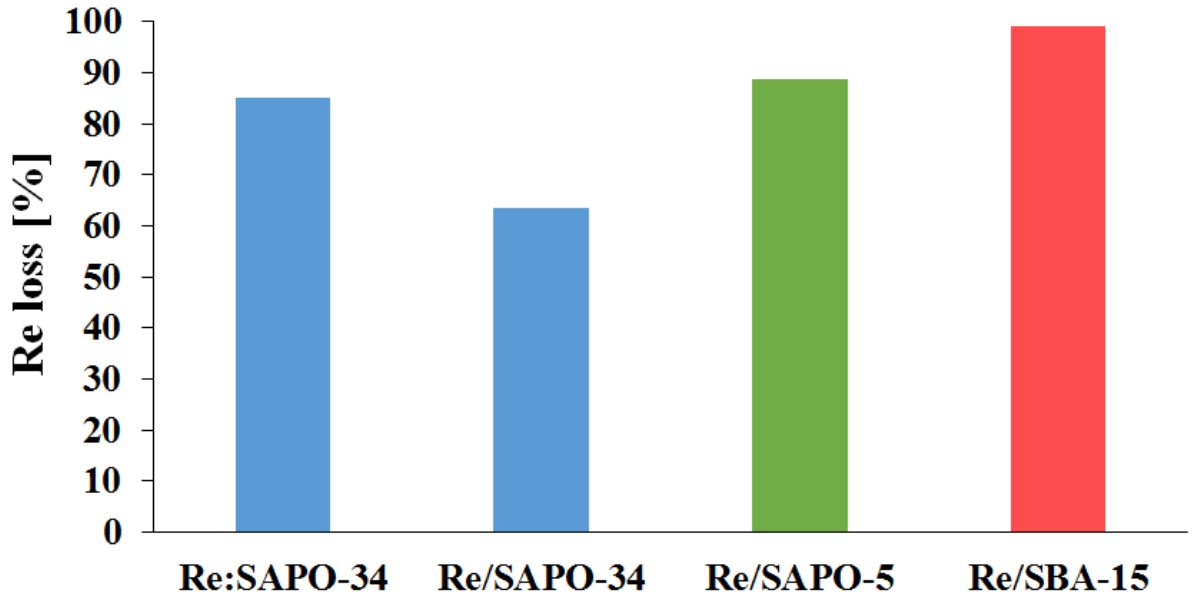

Figure 4.15: Mass loss of rhenium calculated by diving the rhenium content after calcination by rhenium content after direct reduction. Here for ion-exchanged SAPO-34, incipient wetness SAPO-34, incipient wetness SAPO-5 and incipient wetness SBA-15.

In Table 4.12 the names after all the different heat treatments are listed. The first part of the name contain the method of rhenium introduction, either by ion-exchange (Re:) or incipient wetness (Re/), followed by the support material. Next is the heat treatment, which was as prepared (AP), direct reduction (R), calcined (C) or calcined followed by reduction (CR). The weight percentage of rhenium is stated at the end of the name.

Table 4.12: The sample names for different heat treatments, containing information of introduction method, heat treatment and the resulting rhenium loading.

New name	Introduction method	Heat treatment	Re loading [wt.%]
Re:SAPO-34/AP_1.9	Ion-exchange ethanol	As prepared	1.9
Re:SAPO-34/R_3.0	Ion-exchange ethanol	Directly reduced	3.0
Re:SAPO-34/C_0.5	Ion-exchange ethanol	Calcined	0.5
Re:SAPO-34/CR_0.5	Ion-exchange ethanol	Calcined & reduced	0.5
Re/SAPO-34/AP_2.6	Incipient wetness	As prepared	2.6
Re/SAPO-34/R_2.8	Incipient wetness	Directly reduced	2.8
Re/SAPO-34/C_1.0	Incipient wetness	Calcined	1.0
Re/SAPO-34/CR_1.1	Incipient wetness	Calcined & reduced	1.1
Re/SAPO-5/AP_2.3	Incipient wetness	As prepared	2.3
Re/SAPO-5/R_2.1	Incipient wetness	Directly reduced	2.1
Re/SAPO-5/C_0.2	Incipient wetness	Calcined	0.2
Re/SBA-15/AP_2.7	Incipient wetness	As prepared	2.7
Re/SBA-15/R_2.2	Incipient wetness	Directly reduced	2.2
Re/SBA-15/C_0.0	Incipient wetness	Calcined	0.0

4.5 Rhenium detection with XRD

As previously mentioned, the lower limit for detecting crystalline nanoparticles when using XRD are roughly 20 Å. Thus, if the long-range ordering is high enough, metallic rhenium particles above 20 Å can be detected. This does not mean that all rhenium particles are above 20 Å, but that a high enough fraction of larger particles are present, and can therefore be detected. The diffractogram of the SAPO-34 calcined followed by reduction, are shown in the appendix, Figure A.5.

Figure 4.16 shows the diffractogram of the as prepared samples, meaning after metal introduction, but before any heat treatment. For these samples only the SAPO-34 prepared by incipient wetness and ion-exchange in ethanol had a peak corresponding to a different phase than the crystalline support. This peak is positioned at 17 2θ, and among the rhenium references in Figure 2.7, $KReO_4$ had the best fit with this peak. Therefore, the four most intense peaks of $KReO_4$ in this range are shown as the reference in Figure 4.16. The peak indicates the presence of rhenium oxide particles larger than 20 Å for both SAPO-34 samples.

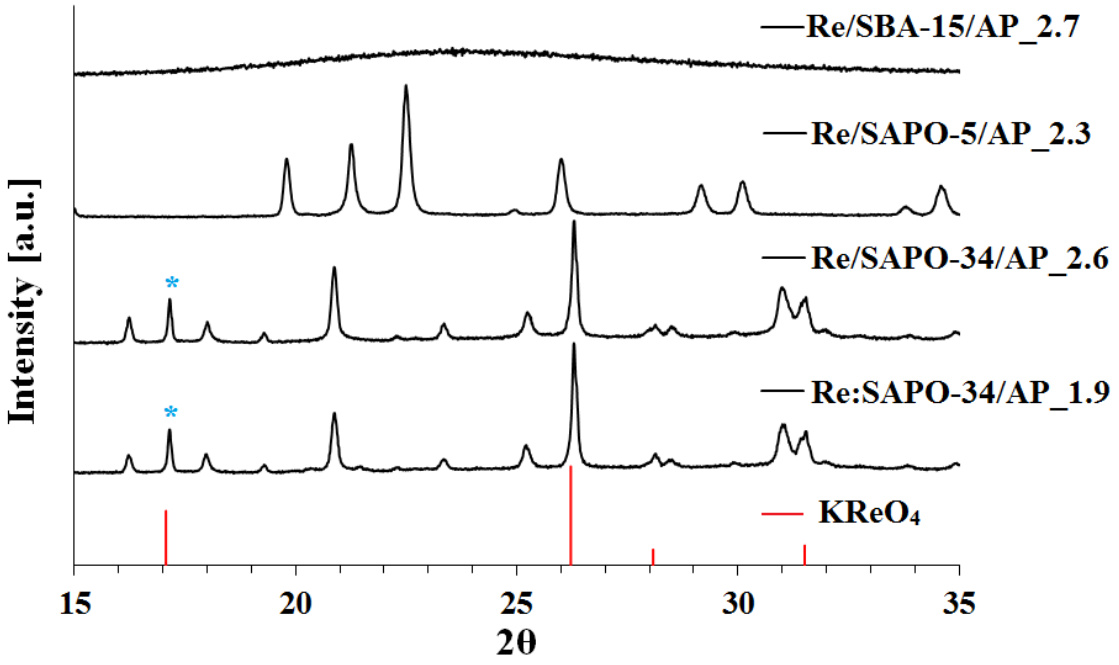

Figure 4.16: XRD diffractogram of as prepared samples, with the four most intense $KReO_4$ peaks in this range. [46] A blue asterisk indicate a peak that corresponds to $KReO_4$.

Figure 4.17 shows the diffractogram of the directly reduced samples, with the three most intense peaks of metallic rhenium as reference. Not surprisingly, the SAPO-34 samples with rhenium oxide in the as prepared samples, show clear peaks of metallic rhenium after reduction. However, the presence of rhenium oxide could not be detected in the as prepared SBA-15 sample, but after reduction low intensity metallic peaks are discernible. This indicates that there has been growth of the rhenium particles during reduction. For Re/SAPO-5/R_2.1 no peaks corresponding to metallic rhenium could be detected.

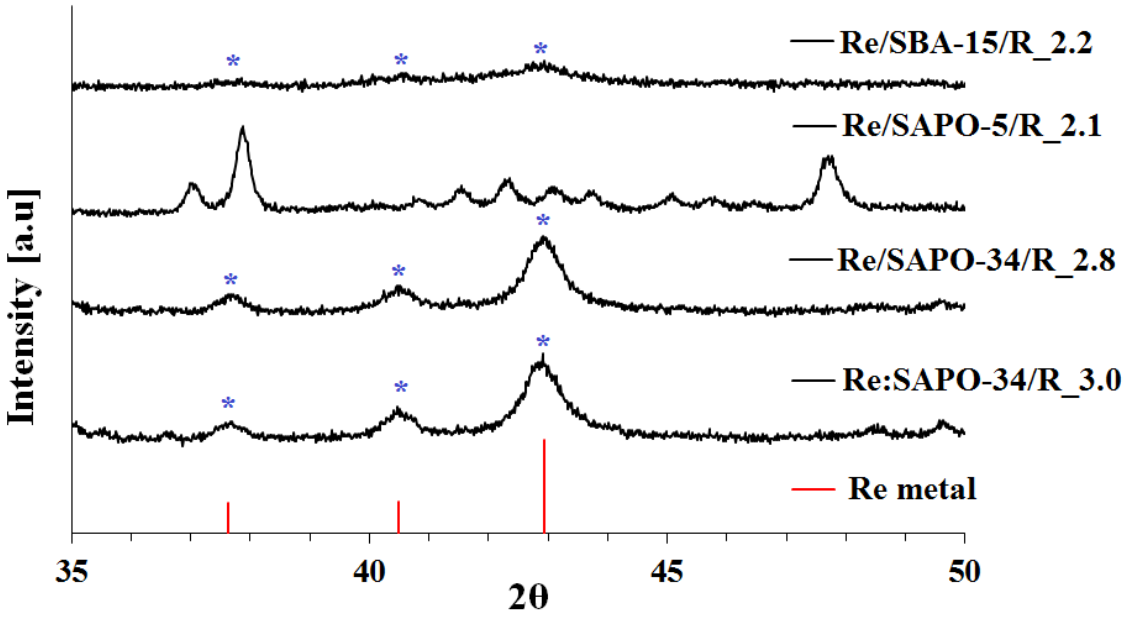

Figure 4.17: XRD diffractogram of samples that were directly reduced, with the three most intense metallic rhenium peaks in this range. [49] A blue asterisk indicate a peak that corresponds to the metallic Re.

4.6 SEM

The SAPO-34/2 sample was imaged by SEM before and after ion-exchange in ethanol, Re:SAPO-34/AP_1.9, as shown in Figure 4.18a and Figure 4.18b respectively. The SAPO-34 particles are cubic before and after introduction. Other than the morphology and particle size of SAPO-34 it is difficult to extract valuable information from these images.

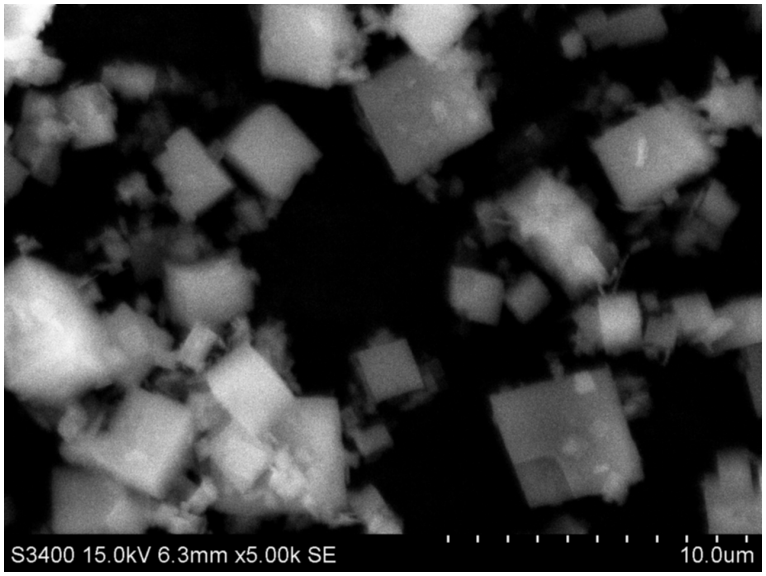

(a)

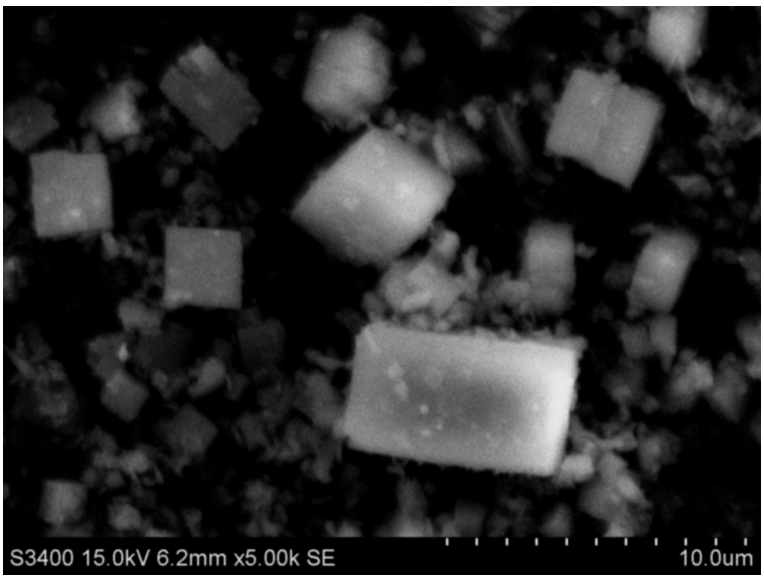

(b)

Figure 4.18: SEM images with magnification of 5k. (a) SAPO-34/2, (b) Re:SAPO-34/AP_2.9

4.7 XAS

4.7.1 Reference compounds

The XANES of the reference compounds Re-foil, ReO_3 and $KReO_4$ are shown in Figure 4.19. The white line of the Re foil is not resolved due to low counts, but the rest of the spectrum can be used.

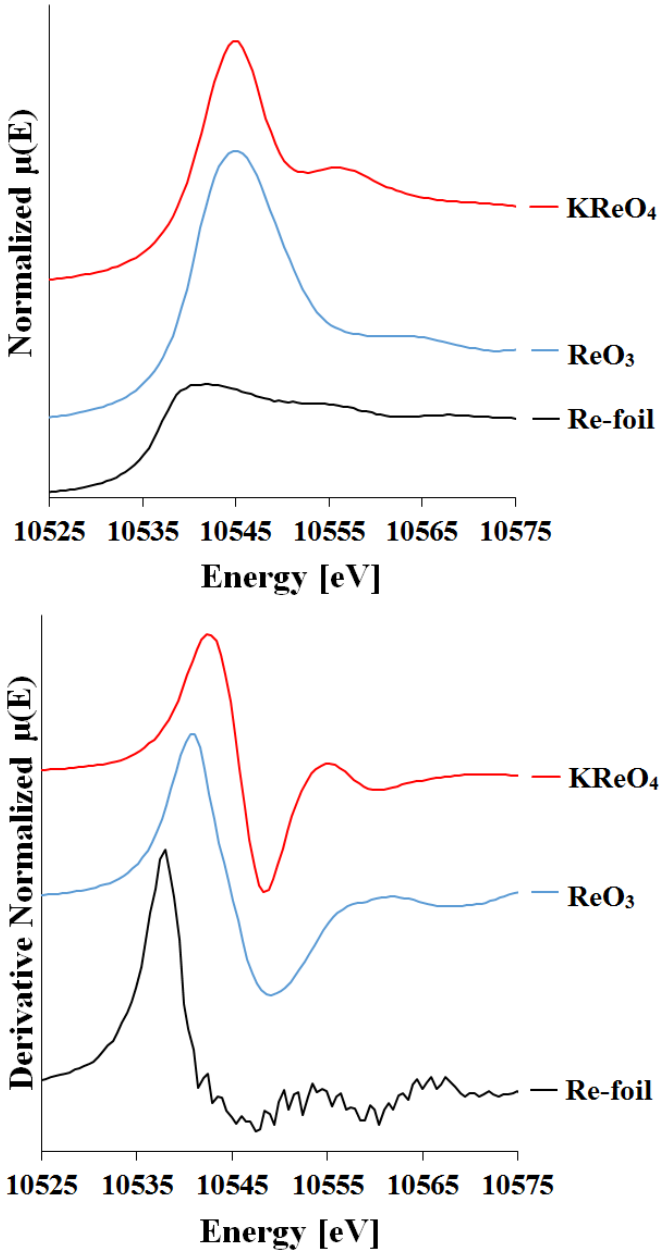

Figure 4.19: The XANES plots of the references Re foil, ReO_3 and $KReO_4$. The top graph shows the normalized μ(E), while the bottom shows derivative normalized μ(E)-plot.

The references in the EXAFS refinements were the Re-foil and NH_4ReO_4, shown in Figure 4.20 and Figure 4.21 respectively. The multiplicity, N, was held constant, while E_F, R, $2\sigma^2$ and the AFAC value were refined for the first coordination shell for both compounds. The resulting refinement values are shown in Table 4.13

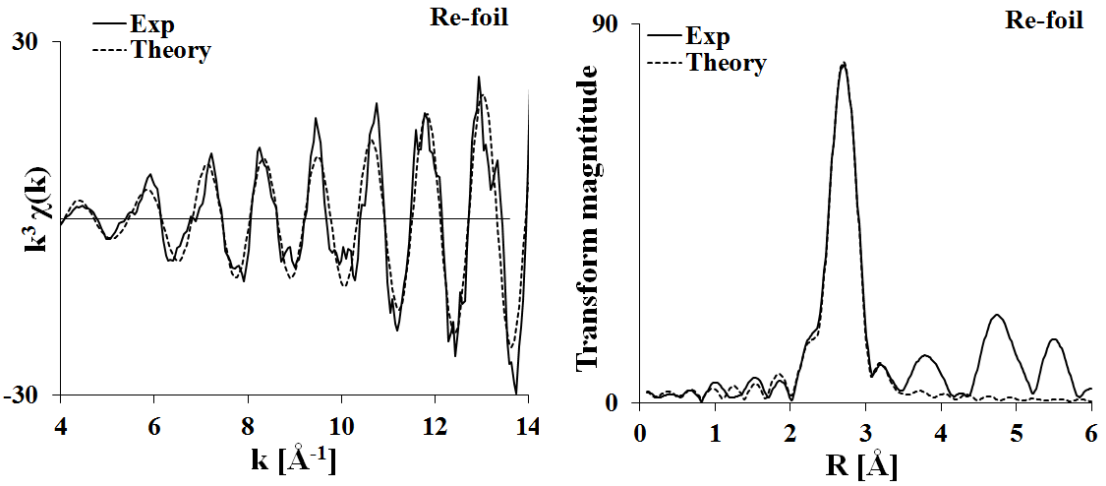

Figure 4.20: EXAFS refinement of AFAC, R, E_F and $2\sigma^2$ for the Re foil, with N = 12.

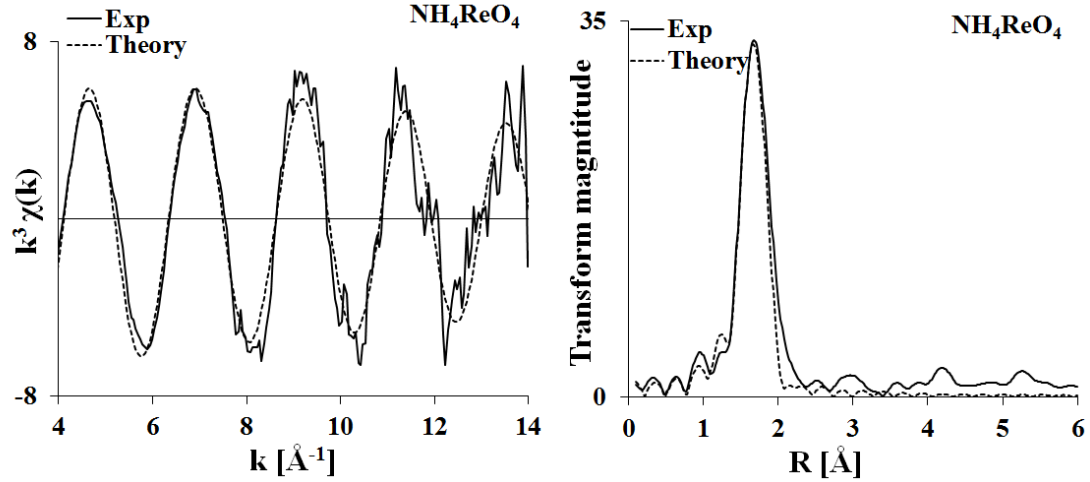

Figure 4.21: EXAFS refinement of AFAC, R, E_F and $2\sigma^2$ for NH_4ReO_4, with N = 4.

Table 4.13: EXAFS refinements for the reference compounds with scatter, interatomic distances, $2\sigma^2$, ΔE_0, k-range and R%. The multiplicity was fixed at theoretical values.

Sample	Scatterer	N	R[Å]	$2\sigma^2$[Å^2]	ΔE_0[eV]	Δk[Å^{-1}]	S_0^2	R(%)
Re-foil	Re	12(-)	2.751(5)	0.007(3)	-15(2)	4-14	0.80	27
NH_4ReO_4	O	4(-)	1.728(5)	0.0017(5)	-17(1)	4-14	0.67	26

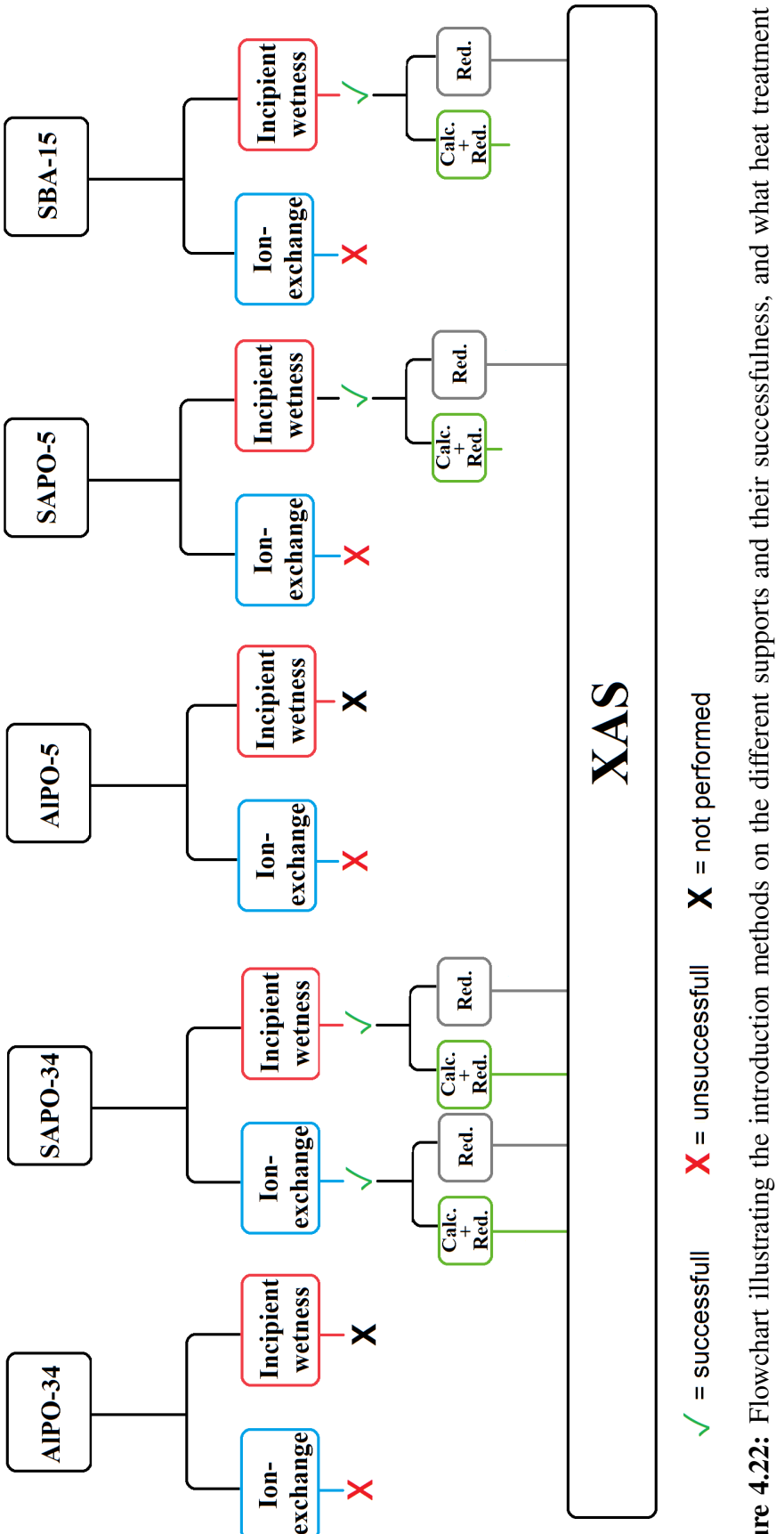

Figure 4.22: Flowchart illustrating the introduction methods on the different supports and their successfulness, and what heat treatment was performed before XAS analysis.

A flowchart illustrating how the different support materials were treated is shown in Figure 4.22. Samples that do not connect with the XAS box were not analyzed with XAS, while the samples that do connect will be regarded in the next subsections.

4.7.2 XANES

The XANES was used in an attempt to determine the oxidation state of the sample based on the references in the previous section. Due to the low resolution of the Re foil over the white line, the fully reduced sample, Re:SAPO-34/R_3.0, was used as the Re(0) reference. The XANES, represented by normalized μ(E) and first derivative normalized μ(E), is shown in Figure 4.23 for samples resembling the metallic sample, and in Figure 4.24 for samples that resembled $KReO_4$.

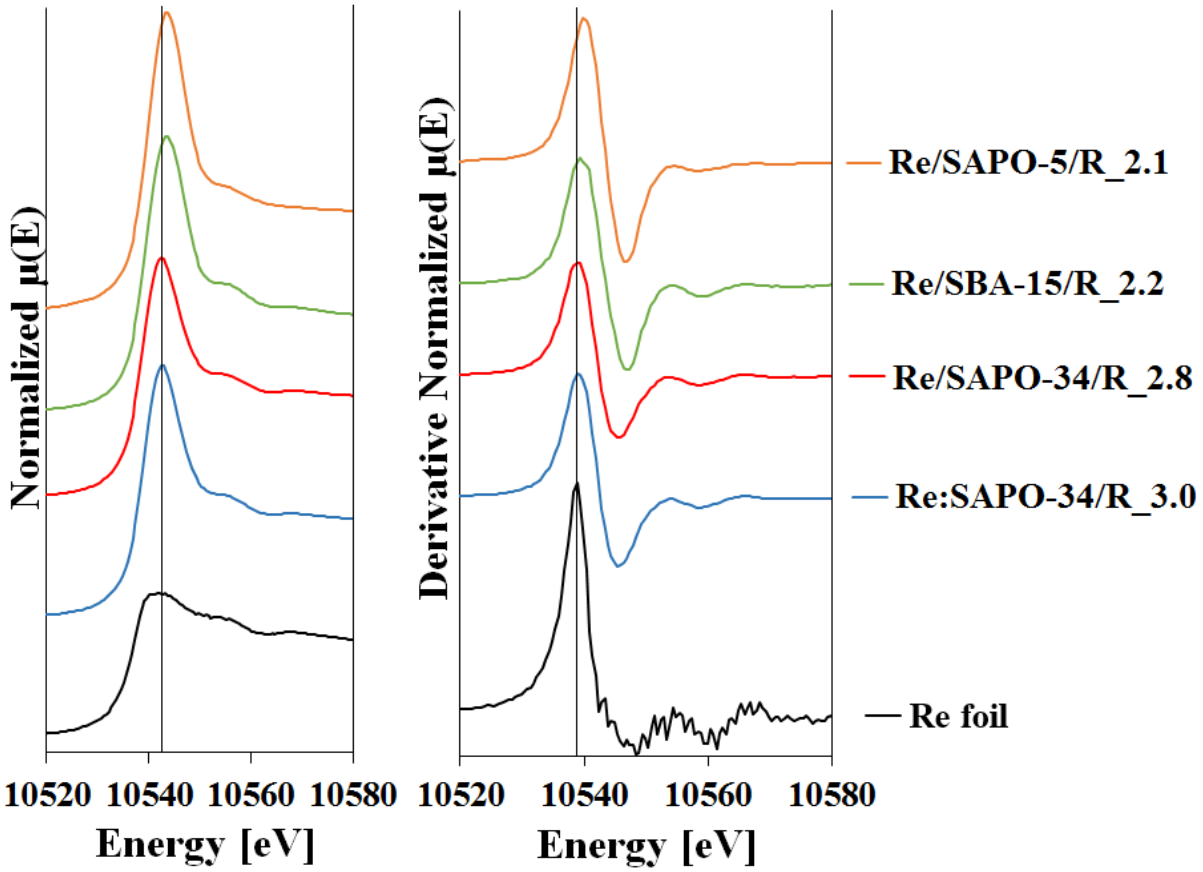

Figure 4.23: The XANES of normalized and first derivative normalized μ(E) for metallic samples and the Re foil. A line is drawn through the peak of the metallic sample, Re:SAPO-34/R_3.0, in both plots, in order to see the relative position to the reference more clearly.

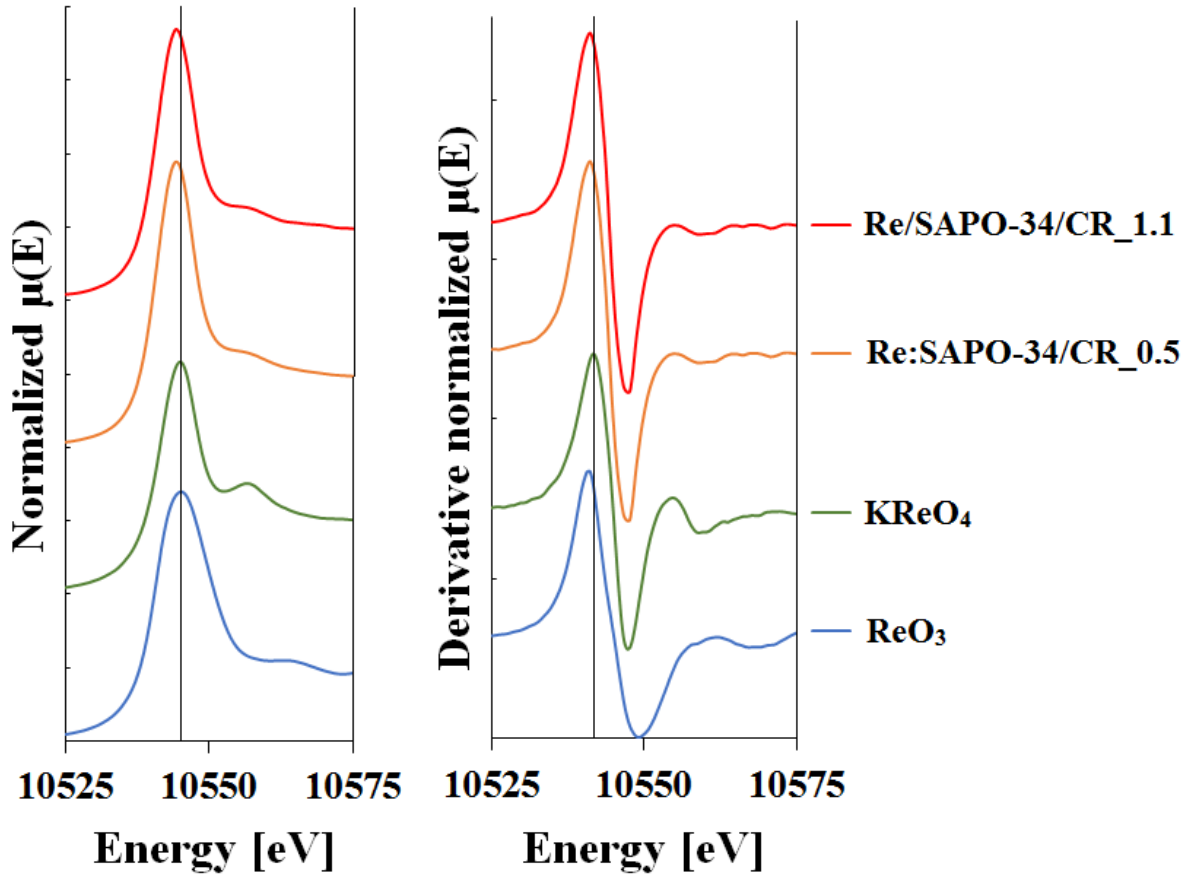

Figure 4.24: The XANES of normalized and first derivative normalized μ(E) for oxide samples and oxide references ReO_3 and $KReO_4$. A line is drawn through the peak of $KReO_4$ in both plots, in order to see the relative position to the standard more clearly.

Literature reports that the intensity of the white line is an indication of the oxidation state of the sample. [74] However, both samples in Figure 4.24 has higher intensity and area under the white line than $KReO_4$. Thus a method using the area under the white line is difficult to use for quantitative determination of the reduced fraction.

Figure 4.25 shows the E_0 value for the samples, with Re:SAPO-34/R_3.0 as metallic reference, and $KReO_4$. The samples are plotted on the trend line between the two references. The samples does not necessarily have the oxidation state of their position in the plot, as they might be a mixture between metallic and oxide species, which can give intermediate E_0 values. The reduced fraction calculated from this data is shown in Figure 4.26. The energy of the top of the white line data was used was also used for a similar trend line plot in Figure 4.27, whereas the reduced fraction based on these values are shown in Figure 4.28.

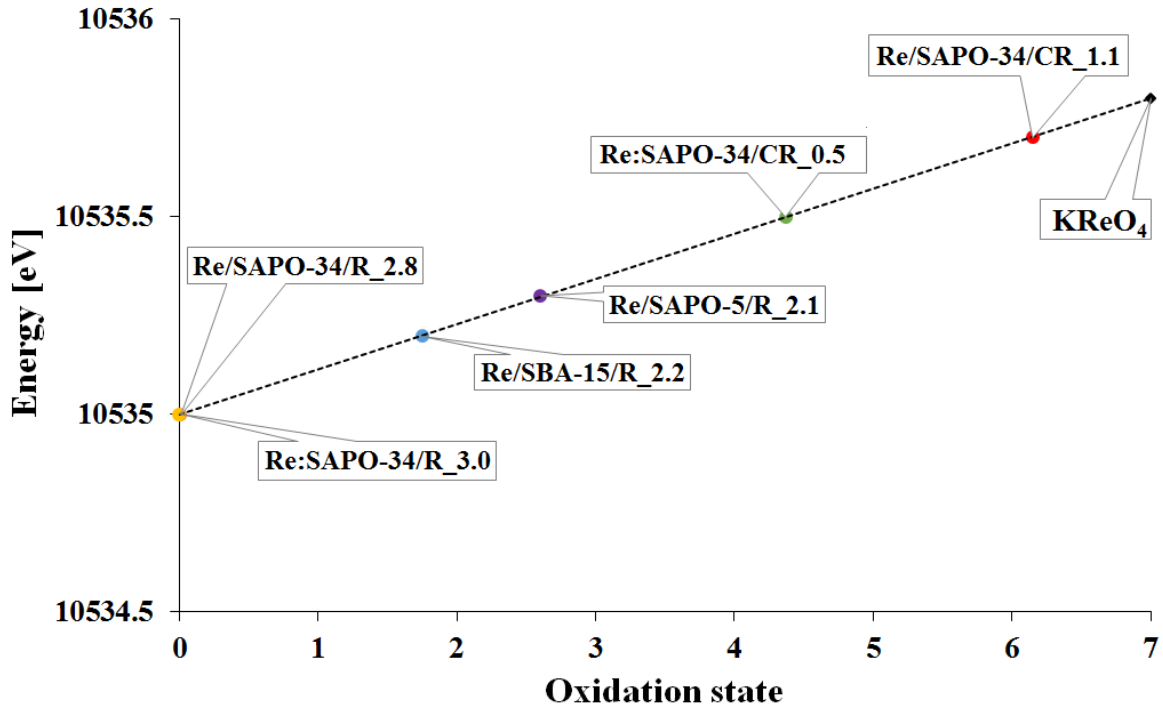

Figure 4.25: The E_0 values for samples and references chosen at 0.5 up the normalized μ(E). A trend line is set between the metallic Re:SAPO-34/R_3.0 and $KReO_4$, and the samples are plotted on this line based on their E_0.

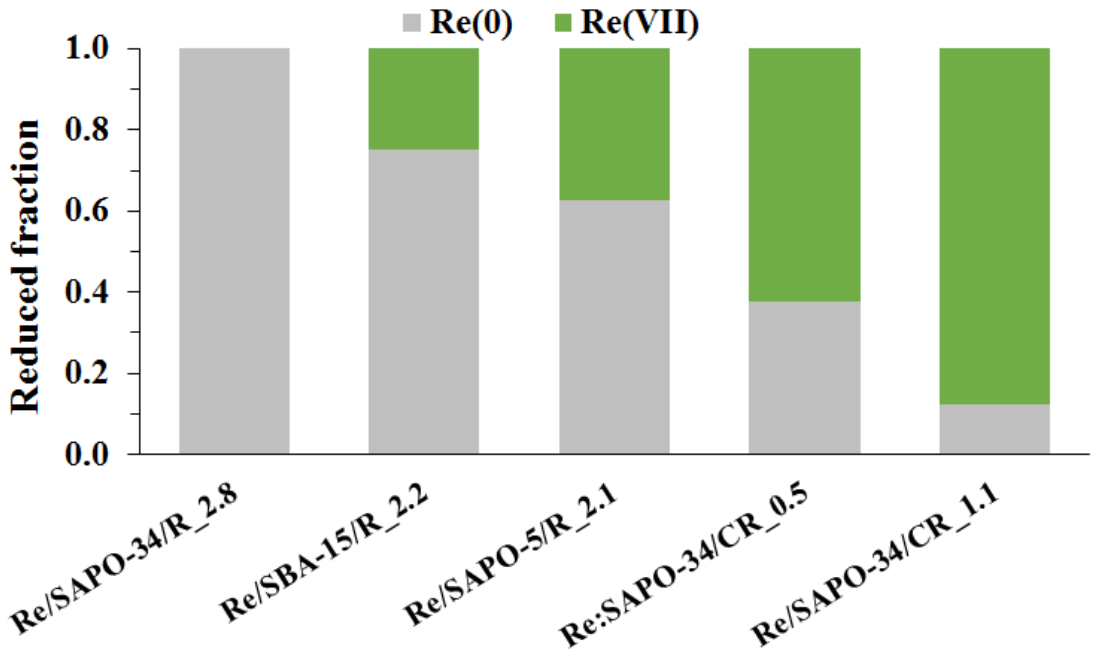

Figure 4.26: The reduced fraction of samples based on the E_0 value. The reference for Re(0) was Re:SAPO-34/R_3.0, and $KReO_4$ for Re(VII).

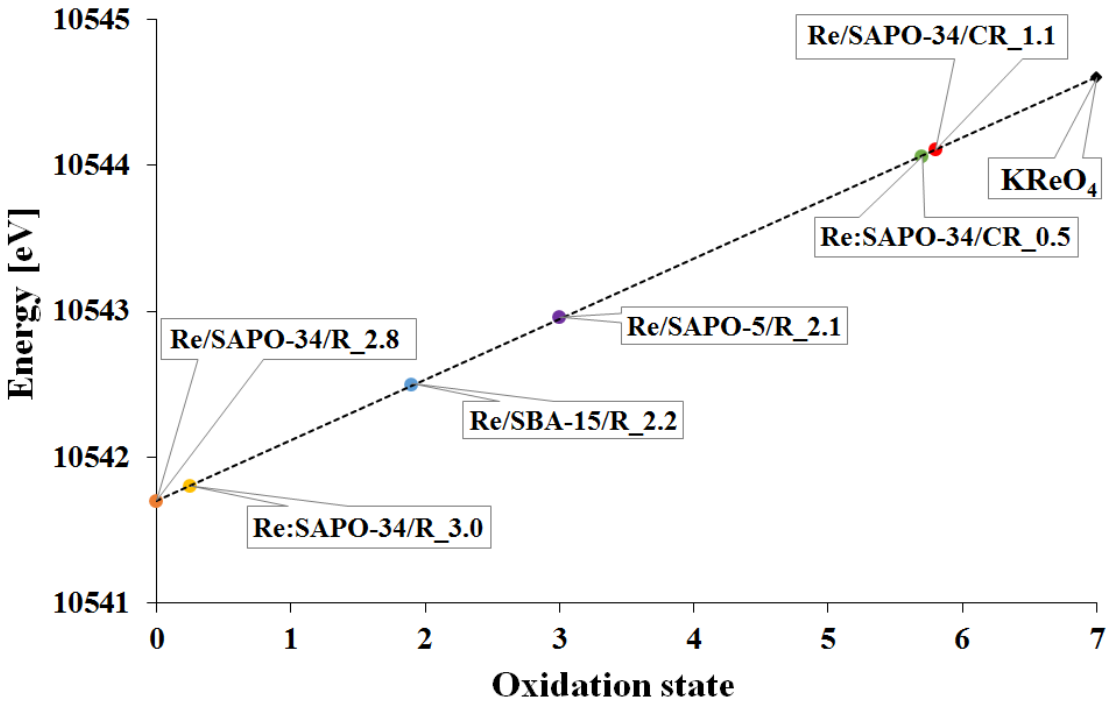

Figure 4.27: The energy values for samples and references chosen at the top of the white line of the normalized μ(E). A trend line is set between the metallic Re:SAPO-34/R_3.0 and $KReO_4$, and the samples are plotted on this line based on the energy at the top of the white line.

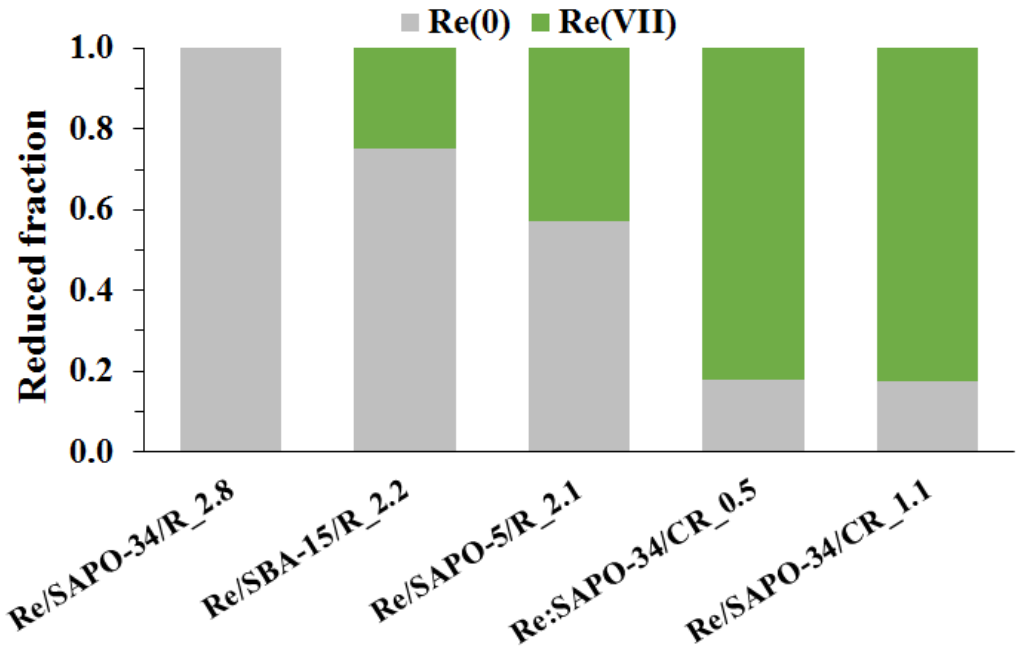

Figure 4.28: The reduced fraction of samples based on the energy value at the top of the white line. The reference for Re(0) was Re:SAPO-34/R_3.0, and $KReO_4$ for Re(VII).

An example of the linear combination of references to make the best fit with Re/SBA-15/R_2.2 is shown in Figure 4.29, and the results for all linear combined samples are summarized in Table 4.14. The fit was performed in the area between the two dotted lines, which was from 5 eV below to 35 eV past E_0.

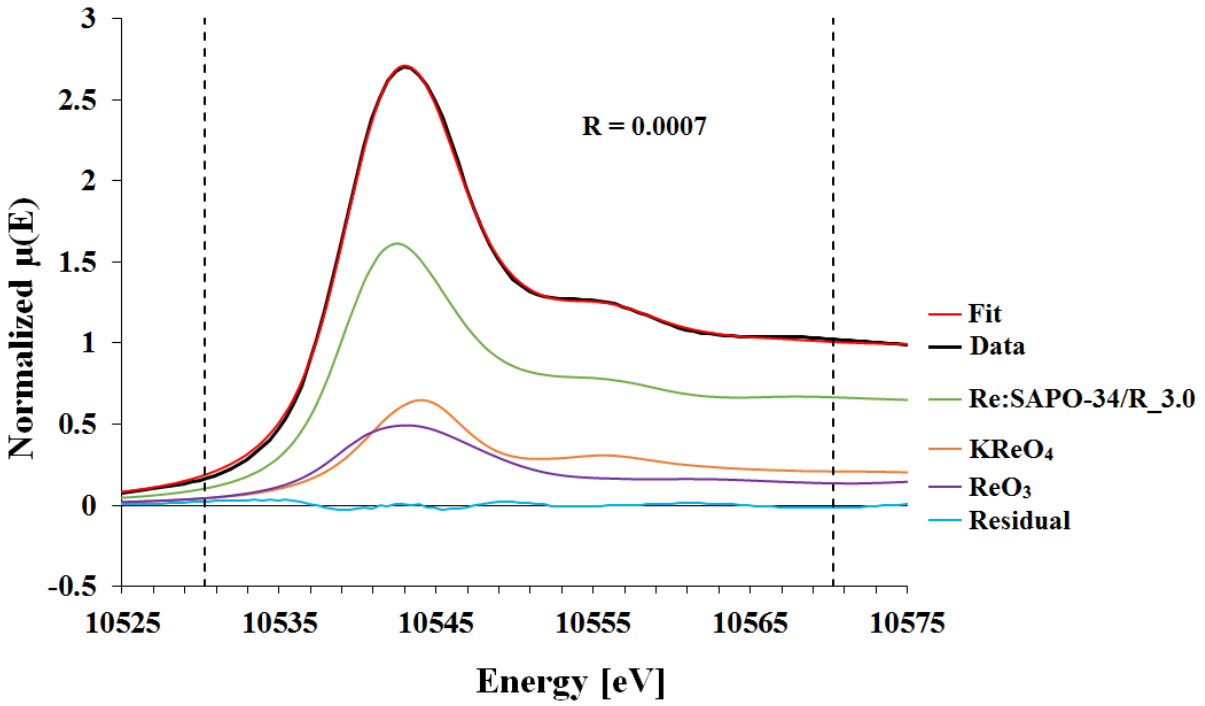

Figure 4.29: Linear combination of the metallic sample Re:SAPO-34/R_3.0, ReO_3 and $KReO_4$ to form the best fit for Re/SBA-15/R_2.2. The plot shows the contribution from each reference, the linear combination (fit) and the residual, which is the difference between data and fit. The fit was performed in the area between the two vertical dotted lines.

Table 4.14: Resulting contribution as fractions for the different from the linear combination of the metallic reference Re:SAPO-34/R_3.0 , ReO_3 and $KReO_4$ to form the best fit for the sample, with the R-factor indicating the goodness of the fit.

Sample name	Fraction Re(0)	Fraction Re(VI)	Fraction Re(VII)	R-factor [10^{-4}]
Re/SAPO-34/R_2.8	1.00	0.00	0.00	125
Re/SBA-15/R_2.2	0.65	0.14	0.21	7
Re/SAPO-5/R_2.1	0.55	0.24	0.21	43
Re:SAPO-34/CR_0.5	0.00	0.52	0.48	391
Re/SAPO-34/CR_1.1	0.00	0.44	0.56	248

The results from all three methods are illustrated in Figure 4.30.

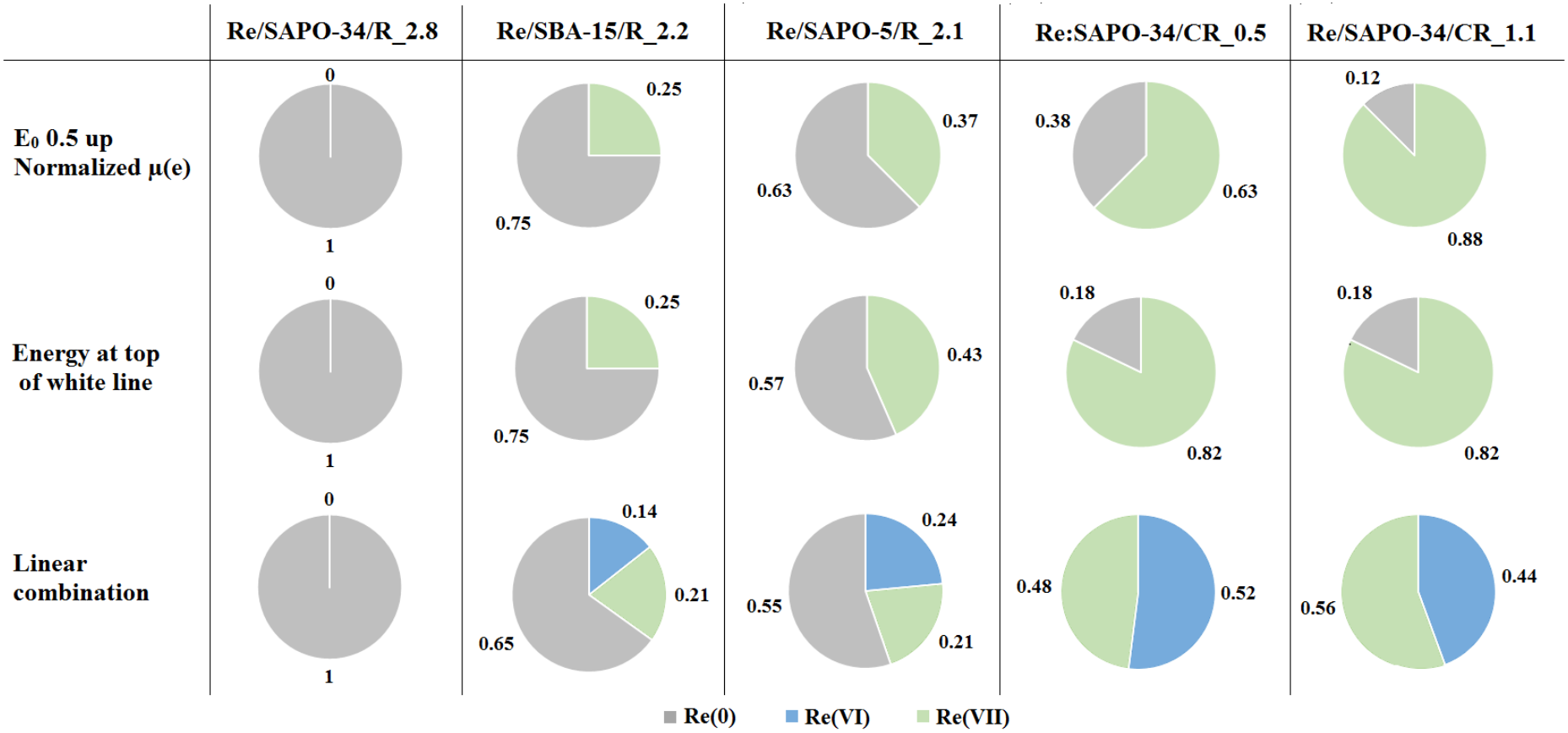

Figure 4.30: Illustration of the reduced fraction based on E_0, top of white line and the linear combinations.

4.7.3 Extended X-ray Absorption Fine Structure (EXAFS)

SAPO-34

The SAPO-34 samples that were analyzed with XAS had rhenium introduced by ion-exchange in ethanol and incipient wetness. For both these methods of introduction, the samples were subject to the two different heat treatments. The EXAFS refinements for the ion-exchanged and directly reduced SAPO-34, Re:SAPO-34/R_3.0, are shown in Figure 4.31. The refinement values are listed in Table 4.15. Only a Re-Re shell was fitted and the resulting fit value was good, which indicates that the sample is metallic. With a multiplicity of 10, the metallic particles are fairly large, and the Re-Re distance is close to that of the bulk metallic rhenium reference. [62]

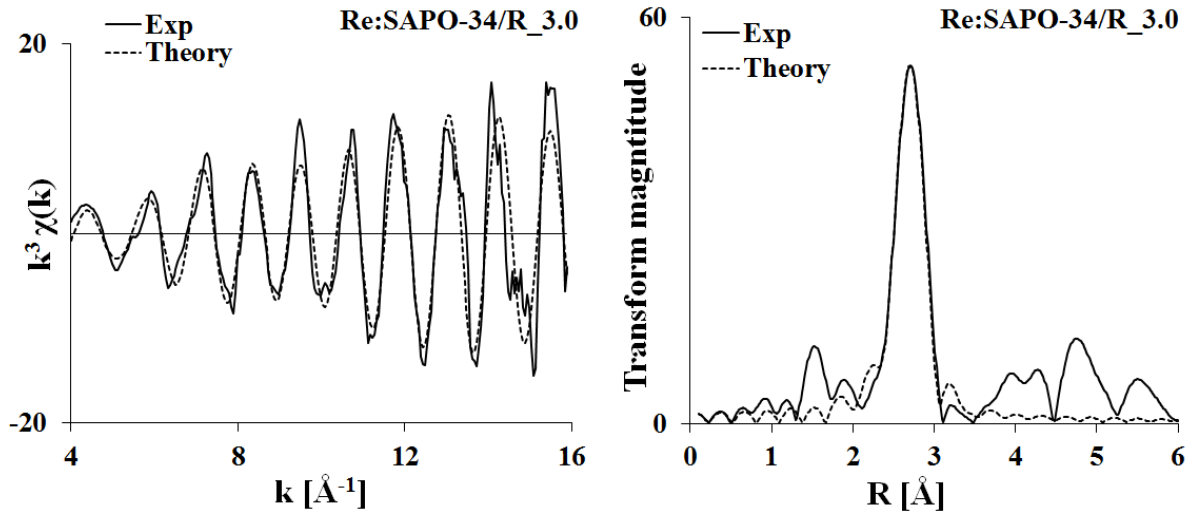

Figure 4.31: EXAFS refinements for SAPO-34 ion-exchanged in ethanol and directly reduced, Re:SAPO-34/R_3.0, in k-space (k^3-weighting) and R-space.

Table 4.15: EXAFS refinements for Re:SAPO-34/R_3.0 with type of scatter, multiplicity, interatomic distance, Debye-Waller factor, shift in E_0, k-range and goodness of fit, R%. The AFAC value was fixed at 0.80

Sample	Scatterer	N	R[Å]	$2\sigma^2$[Å^2]	ΔE_0[eV]	Δk[Å^{-1}]	R[%]
Re:SAPO-34/R_3.0	Re	10(2)	2.748(5)	0.009(1)	-17(2)	4-16	31

The EXAFS refinements for the ion-exchanged SAPO-34, which calcined then subsequently reduced, Re:SAPO-34/CR_0.5, are shown in Figure 4.32. Refinement values are listed in Table 4.16. A good signal was not expected with a rhenium loading of 0.5 wt.%, but a fit value of 37% is decent. The Debye-Waller factor should be positive, but no fits where this value was positive could be made. Different k-weightings, a lower k-range, fixed Debye Waller-factors while refining the other values were attempted, without success. The signal in k-space should be a dampened sine-wave, but in this case it is increasing, which might be why the Debye-Waller factor attempted to improve the fit by decreasing. The other refined values support the presence of ReO_4^-, with approximately 4 coordinating oxygens, but has slightly shorter Re-O distances than for the rhenium oxide references. [62]

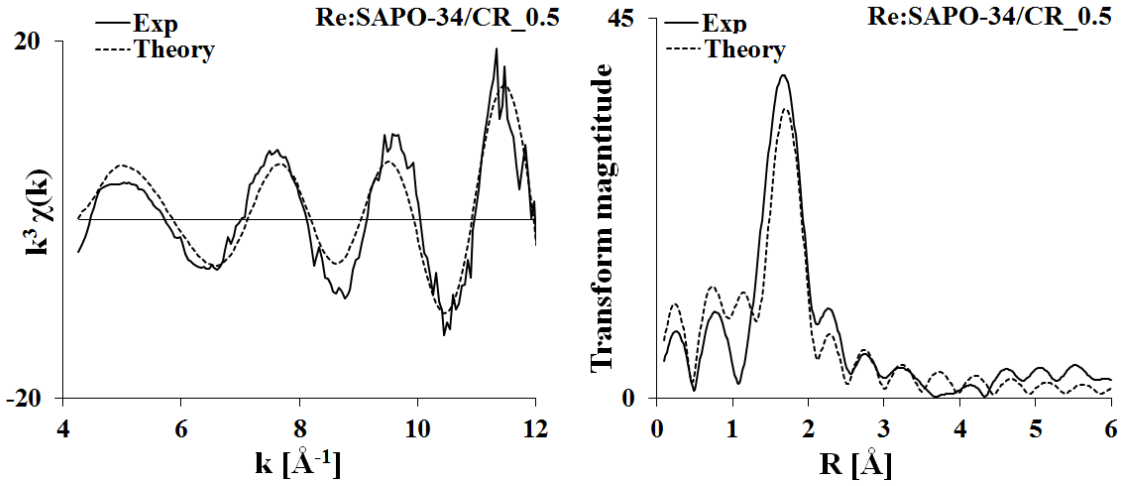

Figure 4.32: EXAFS refinements for SAPO-34 ion-exchanged in ethanol which was calcined and subsequently reduced, Re:SAPO-34/CR_0.5, in k-space (k^3-weighting) and R-space.

Table 4.16: EXAFS refinements for Re:SAPO-34/CR_0.5 with type of scatter, multiplicity, interatomic distance, Debye-Waller factor, shift in E_0, k-range and goodness of fit, R%. The AFAC value was fixed at 0.67.

Sample	Scatterer	N	R[Å]	$2\sigma^2$[Å^2]	ΔE_0[eV]	Δk[Å^{-1}]	R[%]
Re:SAPO-34/CR_0.5	O	4.5(6)	1.704(9)	-0.016(2)	9(3)	4-12	37

The EXAFS refinement for the ion-exchanged and directly reduced SAPO-34, Re/SAPO-34/R_2.8, is shown in Figure 4.33. The refinement values are listed in Table 4.17. The R-factor is high. Attempts were made to fit a Re-O shell, but this resulted with multiplicity close to 0. Reducing the k-range did not lower the R-factor, instead it lead to an increase. Thus it appears that the EXAFS results concurs with the XANES, the sample is metallic. The multiplicity of the Re shell is very low, indicating small rhenium particles, with the Re-Re distance being slightly longer than the bulk reference.

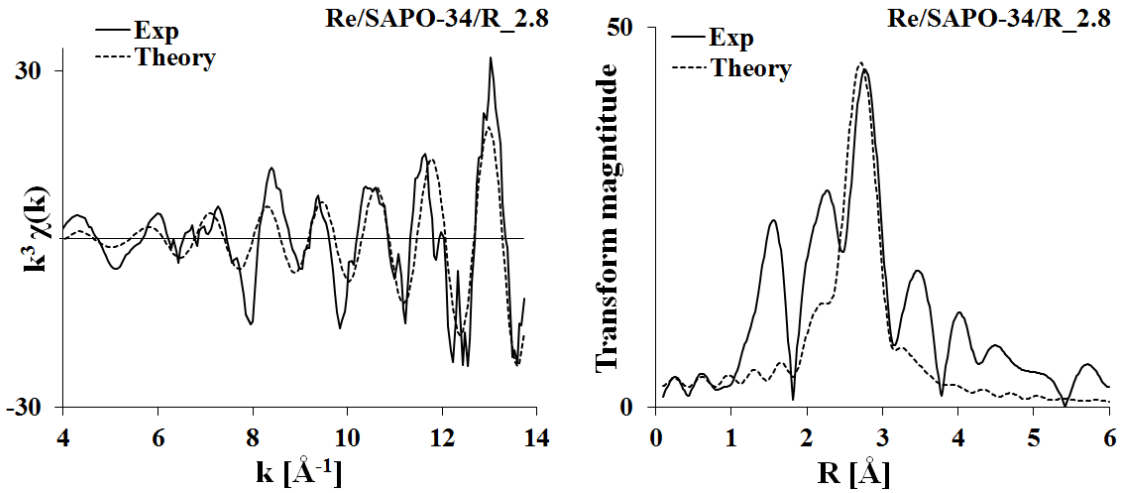

Figure 4.33: EXAFS refinements for incipient wetness and directly reduced SAPO-34, Re/SAPO-34/R_2.8, in k-space (k^3-weighting) and R-space.

Table 4.17: EXAFS refinements for Re/SAPO-34/R_2.8 with type of scatter, multiplicity, interatomic distance, Debye-Waller factor, shift in E_0, k-range and goodness of fit, R%. The AFAC value was fixed at 0.80.

Sample	Scatterer	N	R[Å]	$2\sigma^2$[Å^2]	ΔE_0[eV]	Δk[Å^{-1}]	R[%]
Re/SAPO-34/R_2.8	Re	5(2)	2.76(1)	0.002(2)	-16(5)	4-14	61

The EXAFS refinement for the incipient wetness SAPO-34, which was calcined then subsequently reduced, Re/SAPO-34/CR_1.1, is shown in Figure 4.34. Refinement values are listed in Table 4.18. Despite having a higher loading than Re:SAPO-34/CR_0.5, the signal was poorer for this sample and all refinements resulted in Debye-Waller factors that were negative. The attempts to improve it, the same as with Re:SAPO-34/CR_0.5, were unsuccessful. The multiplicity and the Re-O length is lower than expected for both ReO_3 and ReO_4^{-1}

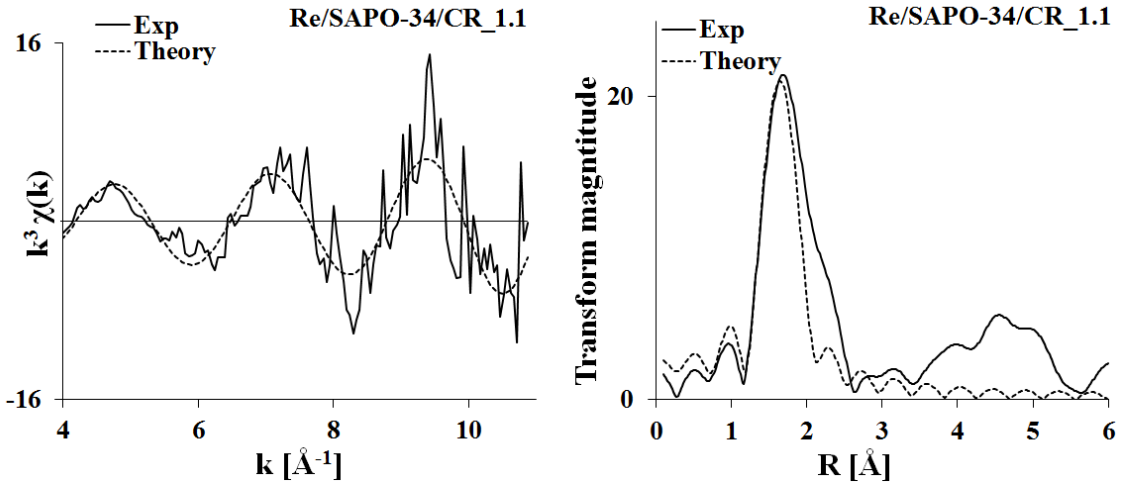

Figure 4.34: EXAFS refinements for incipient wetness, calcined and then reduced SAPO-34, Re/SAPO-34/CR_1.1, in k-space (k^3-weighting) and R-space.

Table 4.18: EXAFS refinements for Re/SAPO-34/R_1.1 with type of scatter, multiplicity, interatomic distance, Debye-Waller factor, shift in E_0, k-range and goodness of fit, R%. The AFAC value was fixed at 0.67.

Sample	Scatterer	N	R[Å]	$2\sigma^2$[Å^2]	ΔE_0[eV]	Δk[Å^{-1}]	R[%]
Re/SAPO-34/CR_1.1	O	1.8(5)	1.69(5)	-0.005(5)	-6(4)	4-11	59

SBA-15

The EXAFS refinement for the incipient wetness SBA-15 which was directly reduced, Re/SBA-15/R_2.2, is shown in Figure 4.35. Refinement values are listed in Table 4.19. Here both a Re-Re and Re-O shell could be fitted with positive Debye-Waller factors and a decent R-factor. The presence of both shells implies that the sample was only partially reduced. Therefore, the multiplicity of Re-Re shell must be corrected in order to evaluate the particle size of the metallic rhenium.

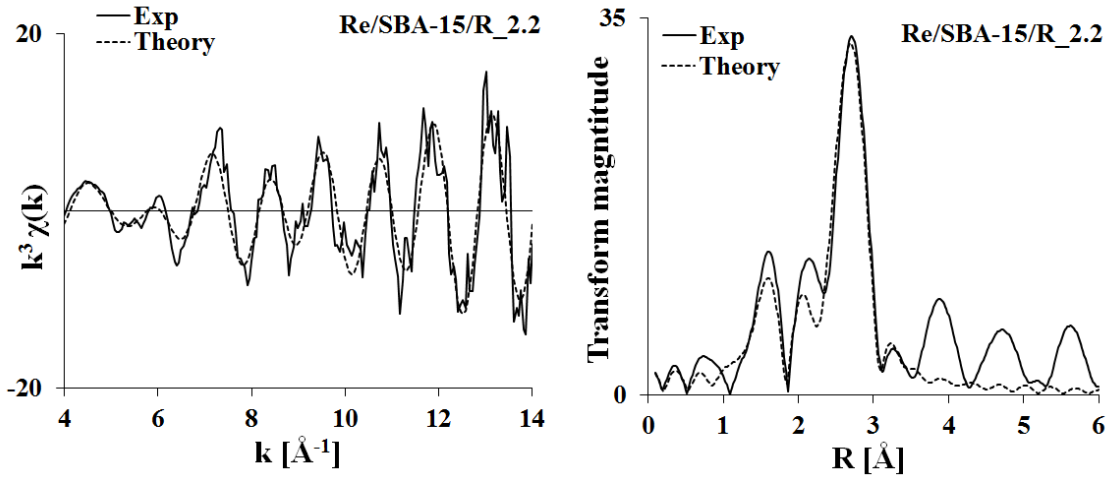

Figure 4.35: EXAFS refinements for incipient wetness and directly reduced SBA-15, Re/SBA-15/R_2.2, in k-space (k^3-weighting) and R-space.

Table 4.19: EXAFS refinements for Re/SBA-15/R_2.2 with type of scatter, multiplicity, interatomic distance, Debye-Waller factor, shift in E_0, k-range and goodness of fit, R%. The AFAC value was fixed at 0.80.

Sample	Scatterer	N	R[Å]	$2\sigma^2$[Å^2]	ΔE_0[eV]	Δk[Å^{-1}]	R[%]
Re/SBA-15/R_2.2	Re	6(1)	2.729(8)	0.007(2)	-8(3)	4-14	43
	O	1.3(7)	1.72(4)	0.003(6)			

For SAPO-5 where rhenium was introduced by incipient wetness, Re/SAPO-5/R_2.3, the resulting EXAFS signal was very poor, as shown in the appendix, Figure D.1. Due to all attempted refinements resulting in very high R-factors, the results were not used for particle size calculations.

4.7.4 Corrected coordination numbers and rhenium particle size

The multiplicities from the EXAFS refinements are the basis for approximating the metallic rhenium particle sizes. The multiplicity of Re-Re shells in samples which are partially oxidized needs to be corrected, but first the methods used to find the reduced fraction of the samples must be evaluated.

E_0 and energy at top of the white line both use the metallic reference and Re(VII) as the reference points, but the E_0 values of Re(IV) and Re(VI) lies below the metallic reference. Thus for the E_0 method, presence of Re(IV) or Re(VI) will skew the result towards metallic Re. The linear combination method can consider several references, and due to being able to fit E_0 within a reasonable range it reduces possible errors in energy corrections, which the two other methods can be heavily affected by.

The linear combination R-factor Re:SAPO-34/CR_0.5 and Re/SAPO-34/CR_1.1 is high, but with no fitted Re-Re shells, there is no metallic particle size to calculate. For Re/SAPO-34/R_2.8 all the 3 methods indicate that the sample is fully reduced. The Re/SAPO-5/R_2.1 had EXAFS data of poor quality, therefore the multiplicity was not used for calculating the metallic rhenium particle size. Thus remains Re/SBA-15/R_2.2, where both a Re-O and Re-Re shell could be fitted in the EXAFS. This sample had an very good fit with the linear combination method, and is the only sample that will have its Re-Re multiplicity corrected, which is why the reduced fraction from this method was used.

The corrected multiplicities and the resulting particle size are shown in Table 4.20.

Table 4.20: Corrected multiplicities for Re-Re shells based on reduced fraction calculated by least-square linear combination of references. [a] The multiplicity is outside the range where the polynomial fit is valid, which results in underestimated particle sizes. [78]

Sample name	Reduced fraction	N	N_{corr}	Particle size [Å]
Re:SAPO-34/R_3.0	1.00	10(2)	10(2)	22[a]
Re/SAPO-34/R_2.8	1.00	5(2)	5(2)	7
Re/SBA-15/R_2.2	0.65	7(2)	9(2)	19

Chapter 5

Discussion

AlPO-34 with HF and EG, SAPO-34, AlPO-5, SAPO-5 and SBA-15 were successfully synthesized. No novel route for synthesizing AlPO-34 without HF was discovered. In theory SAPO-34 and AlPO-34 should have the same pore system, but after calcination AlPO-34 exhibits the triclinic CHA due loss of fluorine which causes hydration of the structure at room temperature.

5.1 Introduction of rhenium through novel routes

Introduction of rhenium into porous supports has previously been performed through methods such as incipient wetness, CVD and physical mixing. In this work a goal was to introduce rhenium through a new method that allows size control of rhenium, but was this successful?

Conventional ion-exchange in aqueous solutions with calcined SAPO-34 was not successful. Based on the anionic state of perrhenate in aqueous solution, no ion-exchange at Brønsted sites was expected. In order to anchor rhenium inside the pores of the support, attempts were made on utilizing rhenium's affinity for amine and quaternary ammonium groups, in this case the SDAs. Performing ion-exchange on as-synthesized SAPO-34 was unsuccessful, which was likely due to the pores being blocked, not allowing the solution to diffuse through the pores. To decrease the degree of blocking and to make the SDAs more fragmented, SAPO-34's were partially calcined at temperatures between 200 and 500°C prior to introduction. Neither this, nor using a SBA-15 sample that was partially calcined at 350°C, was successful.

The second novel route for introduction of rhenium was performed by changing the solvent of the ion-exchange procedure. For acetone a loading of 0.1 wt.% appeared to be the limit when performed on SAPO-34. With ion-exchange in ethanol performed on SAPO-34, a loading of 1.9 wt.% was measured for the as-prepared sample, which further increased to 3.0 wt.% after direct reduction. This appears to be the first successful method with a washing step to introduce rhenium into a porous material. Unfortunately, the same procedure could not be transferred to the other support materials, as the resulting rhenium loading for these samples were around 0.2 wt.% or less.

If the pore system of SAPO-34 was the cause of the high rhenium retention when using ethanol, AlPO-34 would be expected to yield a similar loading with the same procedure. As this was not the case, either the pore system is not the cause of retention, or perhaps the pore system of CHA and triclinic CHA does not have similar behaviour during ion-exchange in ethanol. Brønsted acidity could also explain the rhenium retention in SAPO-34, but then SAPO-5 would be expected to have retained more rhenium than AlPO-5, which was not the case.

Table 5.1 shows the different methods used in an attempt to introduce rhenium into the porous support material in this work, and evaluation of successful loading.

Table 5.1: Summary of the methods of rhenium introduction. Successful introduction was defined as a loading of rhenium above 1 wt.%.

Method	Support	Successful loading
Ion-exchange in water	SAPO-34	X
Partially calcined &	SAPO-34	X
ion-exchange in water	SBA-15	X
Ion-exchange in acetone	SAPO-34	X
Ion-exchange in ethanol	SAPO-34	✓
	AlPO-34, AlPO-5, SAPO-5, SBA-15	X
Incipient wetness	SAPO-34, SAPO-5, SBA-15	✓

5.2 Growth limitations of rhenium

While the rhenium loading was the first measure of success, the success of introduction into the pores has not been evaluated. The size control in the metal introduction step will be reflected by the particle size after reduction. Even though the metallic rhenium particle size is a measure of growth limitations, it also reflects the success of introduction. So far samples have been loaded with an appreciable amount of rhenium, but how does the method of introduction and the pore system of the support affect the metallic rhenium particle sizes?

For the Re:SAPO-34/R_3.0, where rhenium was introduced by ion-exchange in ethanol, the rhenium particles were concluded to be metallic, based on the XANES, EXAFS and XRD results. The observed increase in rhenium loading from as-prepared (1.9 wt.%) to directly reduced (3.0 wt.%) was likely due to loss of residual ethanol from the ion-exchange. Based on the refined multiplicity of 10, the resulting size of the rhenium particles were calculated to be 22 Å. However, the polynomial function used to approximate the particle sizes are only valid for multiplicities between 4.0 and 9.1, thus the particle size is likely underestimated. The metallic rhenium phase was identified in the XRD, which supports the presence of particles larger than 20 Å. The SAPO-34 cages have a diameter of 7.3x10 Å, thus the metallic clusters must mainly be located on the external surface of the support. However, particles around 20 Å is still of interest in terms of catalysis, and thus should not be dismissed as a potential catalyst.

Re/SAPO-34/R_2.8, where rhenium was introduced by incipient wetness, was also determined to contain metallic rhenium. The multiplicity from EXAFS resulted in particle sizes of 7 Å, while rhenium particles above 20 Å were detected with XRD. The multiplicity from EXAFS presents the average coordination of the Re-Re shell, which implies that the size of the average particle is very small and is likely inside the pores or cages of SAPO-34. However, as metallic rhenium could be detected in the XRD, larger particles must be present, which is not surprising when incipient wetness does not ensure size control. Metallic rhenium particles of 7 Å or smaller has not previously been reported for support rhenium. It does therefore appear that incipient wetness is more successful at introducing rhenium into the pores than ion-exchange in ethanol, despite the latter having a washing step. In Figure 5.1 the correlation between metallic particle size after direct reduction and the mass loss caused by calcination is shown for the two

introduction methods on SAPO-34. As the support material is the same, the only variable is the method of introduction. Incipient wetness has smaller particles than ion-exchange in ethanol, and a lower loss of rhenium during calcination. This correlation suggest that rhenium particles introduced into the pore system of SAPO-34 is retained during calcination, while particles on the external surface are removed to a larger extent.

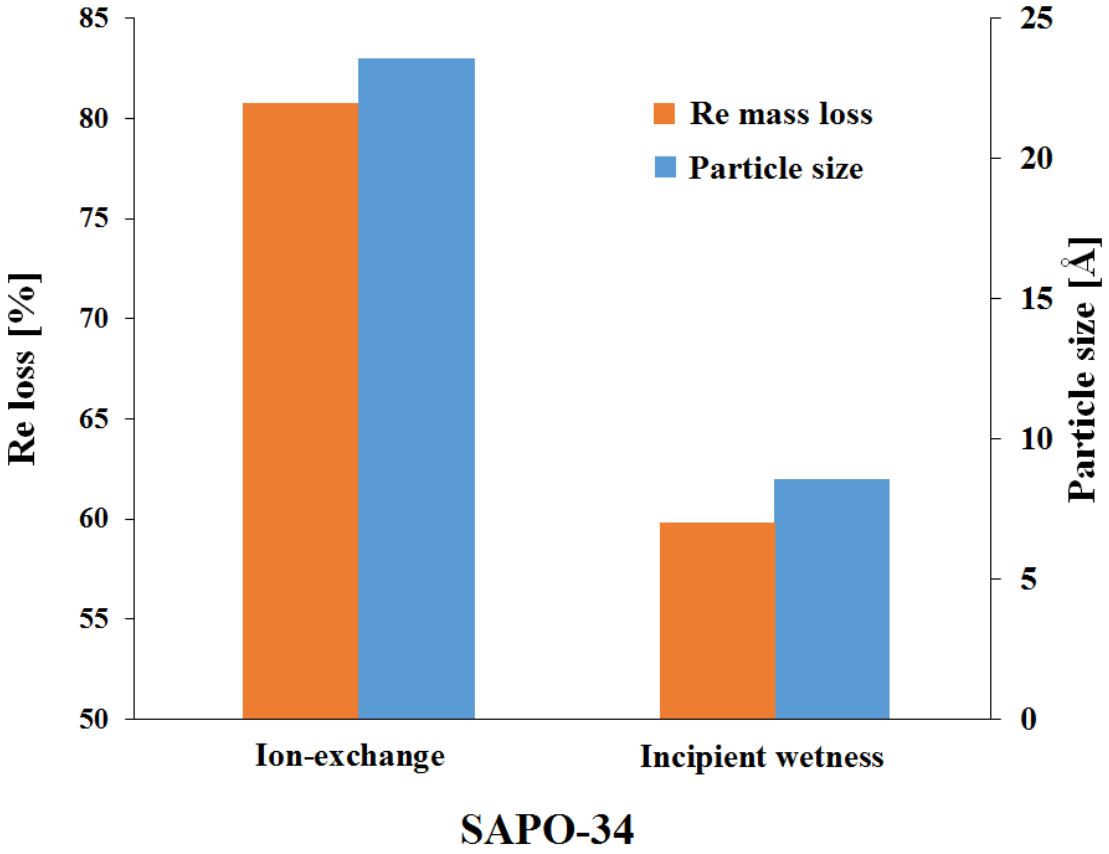

Figure 5.1: Comparison of rhenium mass loss when calcination is performed instead of direct reduction, and the resulting metallic rhenium particle size after reduction for SAPO-34 samples for the two different introduction methods.

Re/SAPO-5/R_2.1 appears to be a mixture of metallic and oxide rhenium particles, with a reduced fraction of 0.55 from the linear combination of the references in XANES. While the EXAFS data was too poor to be used for particle size approximation, no peaks corresponding to metallic rhenium could be discerned in the XRD. The latter implies that there are few metallic particles above 20 Å, as the long-range ordering is not high enough for detection. Unfortunately this is not sufficient to evaluate the growth limitations. Re/SBA-15/R_2.2 was also a mixture of metallic and oxide rhenium, with a reduced fraction of 0.65 and a Re-O shell which could be fitted in EXAFS. Correcting the multiplicity of the Re-Re shell resulted in

approximated metallic rhenium particles of 19 Å. The XRD results yielded very low intensity peaks of metallic rhenium, and as the detection limit is approximately 20 Å, both methods seem to be in agreement. With an average pore size of 53 Å, and an average metallic rhenium particle size of roughly 19 Å, the size control of rhenium appears to be successful.

The mass loss of rhenium during calcination is also interesting when comparing all the supports that were subject to incipient wetness. The three different support materials suffer from a correlation between increasing pore-size and decreasing Brønsted acidity, which makes it difficult to attribute the mass loss to just one of these properties. When comparing the two introduction methods in Figure 5.1 it seemed like the pore system was aiding the retention of rhenium, but this does not mean that Brønsted acidity can be dismissed in this case. Figure 5.2 shows the mass loss due to calcination for the three supports that were subject to incipient wetness, with an indication of increase in acidity and pore size of the support materials. Comparison with the neutral analogies AlPO-34 and AlPO-5 could have given information about the retention of rhenium without Brønsted acidity, but unfortunately no data were collected for these.

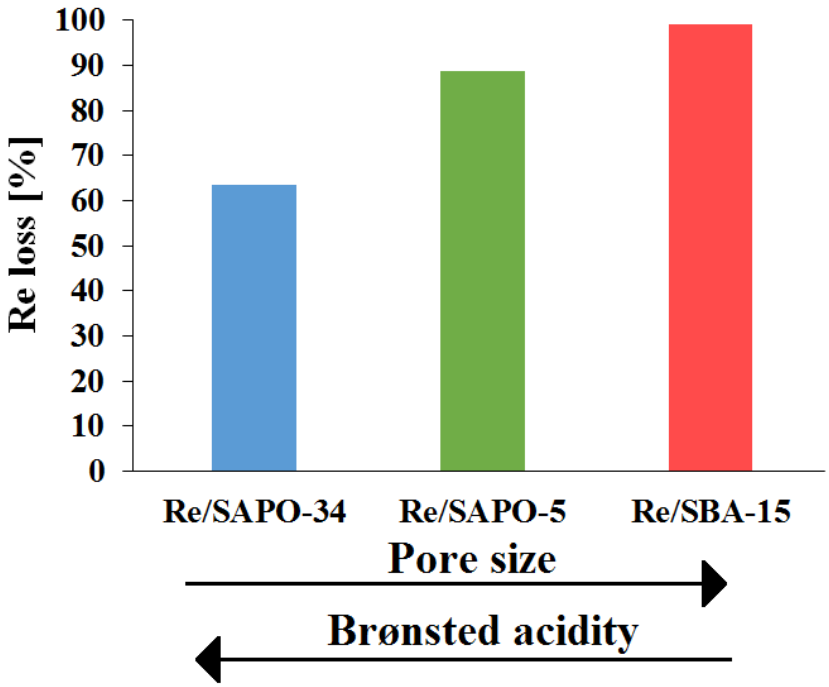

Figure 5.2: Rhenium mass loss when calcination is performed instead of direct reduction in SAPO-34, SAPO-5 and SBA-15 with rhenium introduced by incipient wetness. Increase in pore size and Brønsted acidity among the three support materials is indicated.

The calcined then reduced samples, Re:SAPO-34/CR_0.5 and Re/SAPO-34/CR_1.1, does not appear to be reduced at all, and according to the XANES and EXAFS results they contain only rhenium oxides, and there are two probable explanations for this. Either the samples were not reduced at all, or the samples were reduced then reoxidized in the time period before *ex situ* XAS was performed. The latter option could have been verified by *in situ* XAS reduction, or temperature programmed reduction (TPR). Unfortunately *in situ* XAS was not performed, and the TPR apparatus was unavailable in the time period after the analysis of the XAS data. The growth limitations of these samples cannot be evaluated, but *in situ* XAS reduction should be performed in order to solve similar problems in the future.

Table 5.2 is a summary of the samples containing metallic rhenium. The pore size of the support material is compared to the particle size of the metallic rhenium, in order to evaluate the success of growth limitations.

Table 5.2: Summary of pore (cage) sizes, metallic rhenium particle size approximated from EXAFS and successfulness of growth limitations. All samples detected metallic Re in the XRD.

Sample	Pore (cage) size [Å]	Particle size EXAFS [Å]	Successful growth limitations
Re:SAPO-34/R_3.0	3.8 (6.7x10)	22	X
Re/SAPO-34/R_2.8	3.8 (6.7x10)	7	✓
Re/SBA-15/R_2.2	53	19	✓

Chapter 6

Conclusion

No novel route for synthesizing phase-pure AlPO-34 without HF was discovered, but all other support materials were synthesized successfully. Re_2O_7 was loaded into these supports by two different procedures, ion-exchange in ethanol and incipient wetness impregnation.

The two heat treatments lead to very different results. The direct reduction resulted in metallic rhenium particles for ion-exchange and incipient wetness impregnated SAPO-34. The success of loading rhenium by ion-exchange in ethanol is promising for future experiments. However, the rhenium particles are not growth limited by the pore system, but it still has potential as a catalyst. Incipient wetness performed on SAPO-34 resulted in an average particle size of 7 Å, which suggests that growth limitations were successful, and has not previously been achieved for SAPO-34. The metallic rhenium particles in SBA-15 were approximated to be half that of the average pore size, indicating that growth limitations were successful. For the incipient wetness introduced SAPO-5 and SBA-15, the direct reduction lead to a mixture of metallic rhenium and rhenium oxides. Calcination resulted in a large mass loss of rhenium for all samples, and is not required for the formation of metallic rhenium particles.

The most exciting result of this work is the introduction of metallic rhenium into SAPO-34, which has not previously been achieved. Incipient wetness resulted in very small metallic rhenium particles, which is very promising for future rhenium-containing catalysts.

Chapter 7

Further work

Introducing Re and Co in porous support materials to create $CoRe_4$ nanoparticles is a potential future experiment. Introduction of cobalt in porous materials is much more established in literature than rhenium is. Based on the results of this work, incipient wetness should be used rather than ion-exchange in ethanol, where incipient wetness can be used to co-introduce cobalt and rhenium. Another option is to ion-exchange a cationic cobalt precursor, followed by incipient wetness of rhenium.

The calcination step prior to reduction should be investigated more closely to see if it can be used to selectively remove large rhenium oxide crystals, and leave only nanoparticles in the pores. Economically this is not a good option due to the loss of rhenium, but it would possibly allow study of the nanoparticle properties. This could investigate if nanoparticles of $CoRe_4$ exhibit the same catalytic activity as the bulk analogy.

In order to elucidate the reducibility of rhenium in the different supports, *in situ* XAS and TPR should be performed. Both methods can tell whether the rhenium is reducible at all, but *in situ* XAS can also investigate if rhenium remains reduced in N_2 and H_2 used in the ammonia synthesis.

The incipient wetness on AlPO-34 and AlPO-5, which were not analyzed with XAS in this work, should be prepared and analyzed as they could help decorrelate pore size and Brønsted acidity.

When investigating rhenium samples with XAS, the L_I-edge should also be considered, as the edge contains features which, along with the L_{III}-edge, can give better answers as to what oxidation states rhenium exhibit. Features in the Re L_I-edge can also give information of the rhenium oxide particle size.

Bibliography

[1] J. R. McNeill and W. H. McNeill. *The Human Web: A Bird's-eye View of World History*. W. W. Norton Company, 2003.

[2] A. K. De. *A Text Book of Inorganic Chemistry*. New Age International Publisher, 2003.

[3] V.Smil. *Enriching the Earth: Fritz Haber, Carl Bosch, and the Transformation of World Food Production*. MIT Press, 2004.

[4] H. Bielawa, O. Hinrichsen, A. Birkner, and M. Muhler. The ammonia-synthesis catalyst of the next generation: Barium-promoted oxide-supported ruthenium. *Angewandte Chemie International Edition*, 40(6):1061–1063, 2001.

[5] M. Appl. *Ullmann's Encyclopedia for Industrial Chemistry, Volume 3*. Wiley-VCH, 2011.

[6] K. McAulay, J.S.J. Hargreaves, A.R. McFarlane, D.J. Price, N.A. Spencer, N. Bion, F. Can, M. Richard, H.F. Greer, and W.Z. Zhou. The influence of pre-treatment gas mixture upon the ammonia synthesis activity of Co–Re catalysts. *Catalysis Communications*, 68:53 – 57, 2015.

[7] R. Kojima and K-i. Aika. Rhenium containing binary catalysts for ammonia synthesis. *Applied Catalysis A: General*, 209(1–2):317 – 325, 2001.

[8] J. Emsley. *Nature's Building Blocks, An A-Z Guide to the Elements, New Edition*. Oxford University Press, 2011.

[9] J.C. Mol. Olefin metathesis over supported Rhenium Oxide catalysts. *Catalysis Today*, 51(2):289–299, 1999.

[10] T. Kusakari, T. Sasaki, and Y. Iwasawa. Selective oxidation of benzene to phenol with molecular oxygen on rhenium/zeolite catalysts. *Chem. Commun.*, pages 992–993, 2004.

[11] William M. Haynes. *CRC Handbook of Chemistry and Physics, 93rd Edition*. RC Press, 2013.

[12] M. Asscher, J. Carrazza, M.M. Khan, K.B. Lewis, and G.A. Somorjai. The ammonia synthesis over rhenium single-crystal catalysts: Kinetics, structure sensitivity, and effect of potassium and oxygen. *Journal of Catalysis*, 98(2):277 – 287, 1986.

[13] C. Bréchignac, P. Houdy, and M. Lahmani. *Nanomaterials and Nanochemistry*. Springe-Verlag Berlin Heidelberg, 2006.

[14] R. Kojima, H. Enomoto, M. Muhler, and K-i.. Aika. Cesium-promoted rhenium catalysts supported on alumina for ammonia synthesis. *Applied Catalysis A: General*, 246:311–322, 2003.

[15] I. Chorkendorff and J. W. Niemantsverdriet. *Concepts of Modern Catalysis and Kinetics, 2nd, Revised and Enlarged Edition*. Wiley-VCH, 2007.

[16] J W. Richardson and E.T.C. Vogt. Structure determination and Rietveld refinement of aluminophosphate molecular sieve $ALPO_4$-8. *Zeolites*, 12(1):13 – 19, 1992.

[17] A. Corma and A. Martinez. Zeolites and zeotypes as catalysts. *Advanced Materials*, 7(2):137–144, 1995.

[18] W. Loewenstein. The distribution of aluminum in the tetrahedra of silicates and aluminates. *American Mineralogist*, 39(1-2):92–96, 1954.

[19] A. Corma, F. Rey, S. Valencia, J. L. Jordá, and J. Rius. A zeolite with interconnected 8-, 10- and 12-ring pores and its unique catalytic selectivity. *Nature Materials*, (4):493–497, 2003.

[20] L. Wang, Y. Xu, Y. Weig, J. Duan, A. Chen, B. Wangn, H. Ma, Z. Tian, and L. Lin. Structure-directing role of amines in the ionothermal synthesis. *Journal of the American Chemical Society*, 128(23):7432–7433, 2006.

[21] Definitions of terms relating to the structure and processing of sols, gels, networks, and inorganic-organic hybrid materials (iupac recommendations 2007). *IUPAC. Compendium of Chemical Terminology, 2nd ed. (the*.

[22] G. Sastre and D.W. Lewis. Modelling of bronsted acidity in afi and cha zeotypes. *J. Chem. Soc., Faraday Trans.*, 94:3049–3058, 1998.

[23] J.A. Rabo and G.J. Gajda. Acid function in zeolites: Recent progress. *Catalysis Reviews*, 31(4):385–430, 1989.

[24] E.G. Derouane, F. Lemos, C. Naccache, and F.R. Ribeiro. *Zeolite Microporous Solids: Synthesis, Structure and Reactivity*. Springer Science Business Media, 2012.

[25] M. Harding. and B.M. Kariuki. A multinuclear NMR study of six forms of $AlPO_4$-34: Structure and motional broadening. *Acta Crystallogr.*, page 852, 1994.

[26] B.M. Lok, C.A. Messina, R.L. Patton, R.T. Gajek, T.R. Cannan, and E.M. Flanigen. Silicoaluminophosphate molecular sieves: another new class of microporous crystalline inorganic solids. *Journal of the American Chemical Society*, 106(20):6092–6093, 1984.

[27] S. Ernst. *Advances in Nanoporous Materials, Volume 1*. Elsevier, 2009.

[28] P.B. Weisz. Molecular shape selective catalysis. *Pure and Applied Chemistry*, 52:2091–2103, 1980.

[29] S.M. Csicsery. Catalysis by shape selective zeolites - science and technology. *Pure and Applied Chemistry*, 58(6):841–856, 1986.

[30] De Chen, K.Moljord, T.Fuglerud, and A.Holmen. The effect of crystal size of sapo-34 on the selectivity and deactivation of the MTO reaction. *Microporous and Mesoporous Materials*, 29(1–2):191 – 203, 1999.

[31] Y. Watanabe, A. Koiwai, H. Takeuchi, S.A. Hyodo, and S. Noda. Multinuclear NMR studies on the thermal stability of SAPO-34. *Journal of Catalysis*, 143(2):430 – 436, 1993.

[32] A. Tuel, S. Caldarelli, A. Meden, L.B. McCusker, C. Baerlocher, A. Ristic, N. Rajic, G. Mali, and V. Kaucic. NMR characterization and Rietveld refinement of the structure of rehydrated $AlPO_4$-34. *The Journal of Physical Chemistry B*, 104(24):5697–5705, 2000.

[33] M. Kumar, G.B. Hammond, and B. Xu. Cationic gold catalyst poisoning and reactivation. *Organic Letters*, 16(13):3452–3455, 2014.

[34] I. Bull, G.S. Koermer, A. Moini, and S. Unverricht. Catalysts, systems and methods utilizing non-zeolitic metal-containing molecular sieves having the CHA crystal structure, 08 2009, PCT WO 2009/099937 A1.

[35] S. Masoumi, J. Towfighi, A. Mohamadalizadeh, Z. Kooshki, and K. Rahimi. Tri-templates synthesis of SAPO-34 and its performance in MTO reaction by statistical design of experiments. *Applied Catalysis A: General*, 493:103 – 111, 2015.

[36] N. Najafi, S. Askari, and R. Halladj. Hydrothermal synthesis of nanosized SAPO-34 molecular sieves by different combinations of multi templates. *Powder Technology*, 254:324 – 330, 2014.

[37] J. Wu, H. Zhao, N. Li, Q. Luo, C. He, N. Guan, and S. Xiang. Fluorine-free crystallization of triclinic $AlPO_4$-34. *Cryst.Eng.Comm*, 14:8671–8676, 2012.

[38] D. Li, J. Yao, and H. Wang. Hydrothermal synthesis of $AlPO_4$-5: Effect of precursor gel preparation on the morphology of crystals. *Progress in Natural Science: Materials International*, 22(6):684 – 692, 2012.

[39] D. Zhao, J. Feng, Q. Huo, N. Melosh, G. H. Fredrickson, B.F. Chmelka, and G. D. Stucky. Triblock copolymer syntheses of mesoporous silica with periodic 50 to 300 Ångstrom pores. 279(5350):548–552, 1998.

[40] J.P. Thielemann, F. Girgsdies, R. Schlögl, and C. Hess. Pore structure and surface area of silica SBA-15: influence of washing and scale-up. *Beilstein Journal of Nanotechnology*, (2):110–118, 2011.

[41] L.T. Gibson. Mesosilica materials and organic pollutant adsorption: part a removal from air. *Chem. Soc. Rev.*, 43:5163–5172, 2014.

[42] B.M. Lok, C.A Messina, R.L. Patton, R.T. Gajek, T.R. Cannan, and E.M. Flanigen. Crystal structure of tetrapropylammonium hydroxide-aluminum phosphate number 5. *US Pat. 4 440 871*, 1984.

[43] J.M. Bennet, J.P. Cohen, , J.J Pluth, and J.V. Smith. Crystal structure of tetrapropylammonium hydroxide-aluminum phosphate number 5. *ACS Sym. Ser*, pages 109–118, 1983.

[44] C. Baerlocher, L.B. Mccusker, D. Olson, and W.M. Meier. *Atlas of zeolite framework types*. Published on behalf of the Sturcture Commision of the Internation Zeolite Association by Elseviser, Amsterdam, 2007.

[45] N. Hüsing and U. Schubert. Aerogele – luftige materialien: Chemie, struktur und eigenschaften. *Angewandte Chemie*, 110(1-2), 1998.

[46] H.E. Swanson R.K. Fuyat. U.S. National Bureau of Standards 1. standard X-ray Diffraction Powder Patterns, Vol. 8, 41, 1959.

[47] H.E. Swanson R.K. Fuyat. U.S. National Bureau of Standards 1. standard X-ray Diffraction Powder Patterns, Vol. 9, 7, 1960.

[48] N. Skosyrev, M. Spivak, and I. Sapukov. *Russ. J. Inorg. Chem. (Engl. transl.)*, page 1695, 1985.

[49] H.E. Swanson R.K. Fuyat. U.S. National Bureau of Standards 1. standard X-ray Diffraction Powder Patterns, Vol. 2, 13, 1953.

[50] K.S.W. Sing. Reporting physisorption data for gas/solid systems with special reference to the determination of surface area and porosity. *Pure and Applied Chemistry*, 57(4):603–619, 2009.

[51] N. Murayama, N. Okajima, S. Yamaoka, H. Yamamoto, and J. Shibata. Hydrothermal synthesis of $AlPO_4$-5 type zeolitic materials by using aluminum dross as a raw material. *Journal of the European Ceramic Society*, 26(4–5):459 – 462, 2006.

[52] E.P. Barret, L. G. Joyner, and P.P. Halenda. The determination of pore volume and area distributions in porous substances. i. computations from nitrogen isotherms. *Journal of the American Chemical Society*, 73(1):373–380, 1951.

[53] B. H. Stuart. *Infrared Spectroscopy: Fundamentals and Applications*. Wiley, 2004.

[54] W. R. Moser, C-C. Chiang, and R.W. Thompson. Infrared diffuse reflectance study of the silicon-rich h-zsm-5 catalysis of ethanol conversion. *Journal of Catalysis*, 115(2):532 – 541, 1989.

[55] H.G. Karge and E. Boldingh. Spectroscopic investigations on deactivation of zeolite catalysts during reactions of olefins. *Catalysis Today*, 3(5):379 – 386, 1988.

[56] G. Ertl, H. Knözinger, and J. Weitkamp. *Preparation of Solid Catalysts*. Wiley-VCH Verlag GmbH Co. KGaA, 2008.

[57] L. Guczia and I. Kiricsib. Zeolite supported mono- and bimetallic systems: structure and performance as {CO} hydrogenation catalysts. *Applied Catalysis A: General*, 186(1–2):375 – 394, 1999.

[58] K. Mathisen, M.N. Hellner, C. Nordhei, and D.G. Nicholson. Irreversible silver(i) interconversion in ag:zsm-5 and Ag:SAPO-5 by propene and hydrogen. *The Journal of Physical Chemistry C*, 116(1):171–184, 2012.

[59] E. Marceau, X. Carrier, and M. Che. *Synthesis of Solid Catalysts*. Wiley-VCH Verlag GmbH Co. KGaA, Weinheim, Germany, 2009.

[60] J. Xie, J. Yang, A.I. Dugulan, A. Holmen, De Chen, K.P de Jong, and M.J Louwerse. Size and promoter effects in supported iron fischer–tropsch catalysts: Insights from experiment and theory. *ACS Catalysis*, 6(5):3147–3157, 2016.

[61] N. Viswanadham, T. Shido, and Y. Iwasawa. Performances of rhenium oxide-encapsulated ZSM-5 catalysts in propene selective oxidation/ammoxidation. *Applied Catalysis A: General*, 219(1–2):223 – 233, 2001.

[62] M. Rønning, T. Gjervan, R. Prestvik, D. G. Nicholson, and A. Holmen. Influence of pretreatment temperature on the bimetallic interactions in Pt-Re/Al_2O_3 reforming catalysts studied by X-Ray Absorption Spectroscopy. *Journal of Catalysis*, 204(2):292 – 304, 2001.

[63] B. Mitra, X. Gao, I.E. Wachs, A.M. Hirt, and G. Deo. Characterization of supported rhenium oxide catalysts: effect of loading, support and additives. *Phys. Chem. Chem. Phys.*, 3:1144–1152, 2001.

[64] R.R. Srivastava, J c. Lee, and M s. Kim. Complexation chemistry in liquid–liquid extraction of rhenium. *Journal of Chemical Technology Biotechnology*, 90(10), 2015.

[65] P. Arnoldy, J.A.M. van den Heijkant, V.H.J. de Beer, and J.A. Moulijn. Temperature-programmed sulfiding of Re_2o_7/Al_2O_3 catalysts. *Applied Catalysis*, 23(1):81 – 99, 1986.

[66] E. Kim, M. F. Benedetti, and J. Boulègue. Removal of dissolved rhenium by sorption onto organic polymers: study of rhenium as an analogue of radioactive technetium. *Water Research*, 38(2):448 – 454, 2004.

[67] F.D. Hardcastle and I.E. Wachs. The structure of surface rhenium oxide on alumina from laser Raman spectroscopy and X-ray Absorption Near-edge Spectroscopy. *Journal of Molecular Catalysis*, 46(1):15 – 36, 1988.

[68] A. Montaser. *Inductively Coupled Plasma Mass Spectrometry*. Wiley-VCH, 1998.

[69] J.I. Goldstein, D.E. Newbury, P. Echelin, D.C. Joy, A.D. Romig Jr., C.E. Lyman, C. Fiori, and E. Lifshin. *Scanning Electron Microscopy and X-ray Microanalysis, Second Edition*. Plenum Press, New York, 1992.

[70] M. Newville. Fundamentals of XAFS. `http://www.xafs.org/Tutorials`. Accessed: 2017-02-28.

[71] J.H. Hubbell and S.M. Seltzer. Tables of X-ray mass attenuation coefficients and mass energy-absorption coefficients from 1 keV to 20 MeV for elements Z = 1 to 92 and 48 additional substances of dosimetric interest. `https://www.nist.gov/pml/x-ray-mass-attenuation-coefficients`. Accessed: 2017-01-02.

[72] J.A. Bearden and A.F. Burr. Reevaluation of x-ray atomic energy levels. *Rev. Mod. Phys.*, 39:125–142, 1967.

[73] A. Tougerti, S. Cristol, E. Berrier, V. Briois, C. La Fontaine, F. Villain, and Y. Joly. XANES study of rhenium oxide compounds at the L_1 and L_3 absorption edges. *Phys. Rev. B*, 85:125–136, 2012.

[74] T. Ebashi, Y. Ishida, Y. Nakagawa, S-i. Ito, T. Kubota, and K. Tomishige. Preferential CO oxidation in a H_2-rich stream on Pt-ReOx/SiO_2: Catalyst structure and reaction mechanism. *The Journal of Physical Chemistry C*, 114(14):6518–6526, 2010.

[75] S.R. Bare, S.D. Kelly, F.D. Vila, E. Boldingh, E. Karapetrova, J. Kas, G.E. Mickelson, F.S. Modica, N. Yang, and J.J. Rehr. Experimental (XAS, STEM, TPR, and XPS) and theoretical (DFT) characterization of supported rhenium catalysts. *The Journal of Physical Chemistry C*, 115(13):5740–5755, 2011.

[76] B.K. Teo. *EXAFS: Basic principles and data analysis*. Springer-Verlag Berlin Heidelberg, 1986.

[77] S. Bordiga, E. Groppo, G. Agostini, J. A. van Bokhoven, and C. Lamberti. Reactivity of surface species in heterogeneous catalysts probed by in situ X-ray absorption techniques. *Chemical Reviews*, 113(3):1736–1850, 2013.

[78] J. de Graaf, A.J. van Dillen, K.P. de Jong, and D.C. Koningsberger. Preparation of highly dispersed Pt particles in Zeolite Y with a narrow particle size distribution: Characterization by hydrogen chemisorption, TEM, EXAFS spectroscopy, and particle modeling. *Journal of Catalysis*, 203(2):307 – 321, 2001.

[79] C. Wang, J. Wu, Mi. Hu, N. Li, N. Guan, and S. Xiang. Synthesis of $AlPO_4$-34 and its large single crystal by partially substituting framework fluorine with oxygen species. *Journal of Porous Materials*, 19(5):751–759, 2012.

[80] A.P. Giaquinto. Synthesis, modification, and characterization of spherical SBA-15 ordered mesoporous silica and evaluation in high performance liquid chromatography. *Seton Hall University Dissertations and Theses (ETDs), Paper 1803.*, 2012.

[81] L. Wang, A. Kong, B. Chen, H. Ding, Y. Shan, and M. He.

[82] S. Brunauer, P.H. Emmett, and E. Teller. Adsorption of gases in multimolecular layers. *Journal of the American Chemical Society*, 60(2):309–319, 1938.

[83] B. Ravel and M. Newville. *ATHENA*, *ARTEMIS*, *HEPHAESTUS*: data analysis for X-ray absorption spectroscopy using *IFEFFIT*. *Journal of Synchrotron Radiation*, 12(4):537–541, 2005.

[84] S. Tomic, B.G. Searle, A. Wander, N.M. Harrison, A.J. Dent, J.F.W. Mosselmans, and J.E. Inglesfield. New tools for the analysis of EXAFS: The DL EXCURV package. *Council for the Central Laboratory of the Research Councils*.

[85] M. Ganschowand, G. Schulz-Ekloff, M. Wark, M. Wendschuh-Josties, and D. Wohrle. Microwave-assisted preparation of uniform pure and dye-loaded $AlPO_4$-5 crystals with different morphologies for use as microlaser systems. *J. Mater. Chem.*, 11:1823–1827, 2001.

Appendix

A XRD

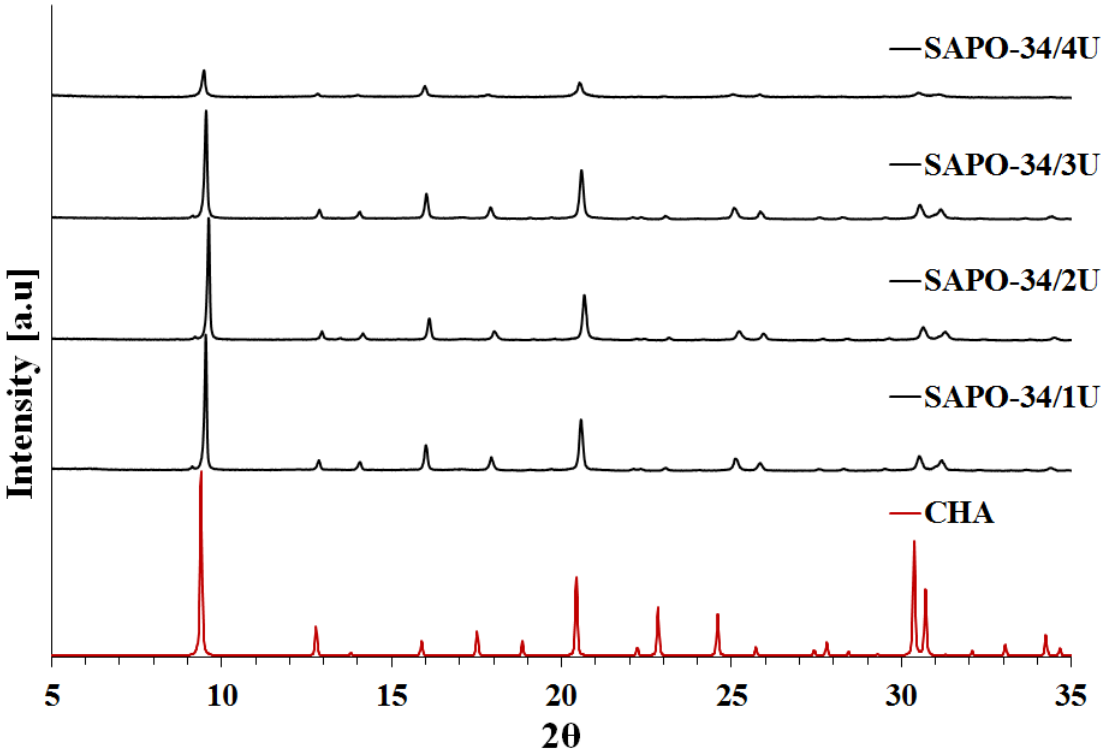

Figure A.1: XRD diffratogram of as-synthesized (U) SAPO-34 samples synthesized with TEAOH as SDA.

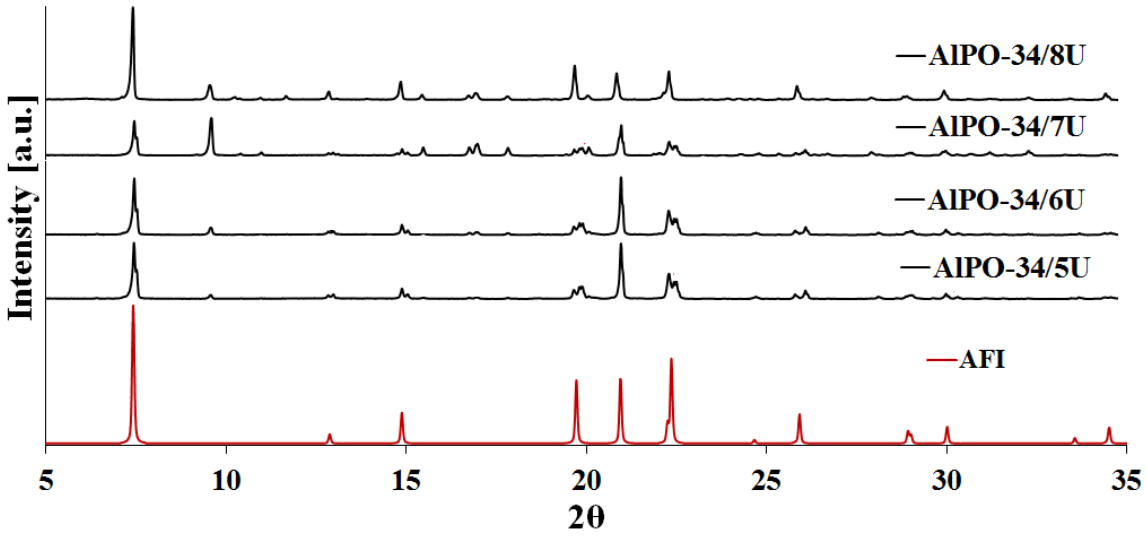

Figure A.2: XRD diffratogram of as-synthesized (U) AlPO-34 samples synthesized with TEAOH, TEA, DEA and Mor as SDAs.

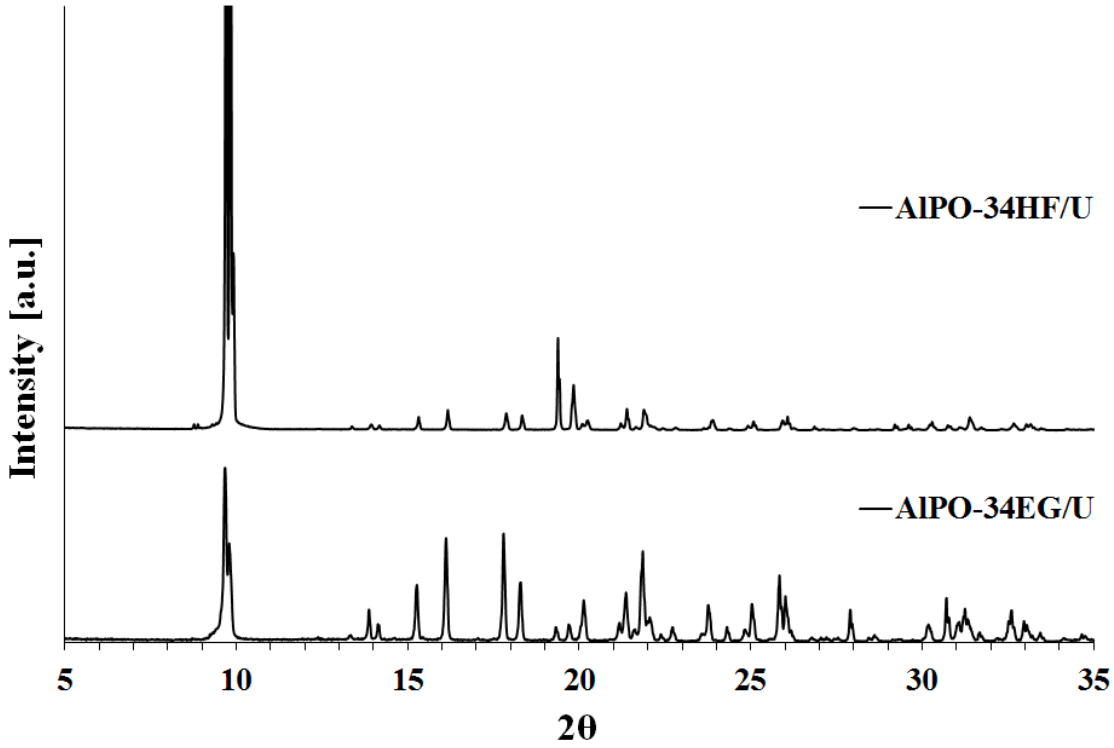

Figure A.3: XRD diffractogram of calcined (U) AlPO-34 samples using HF and EG.

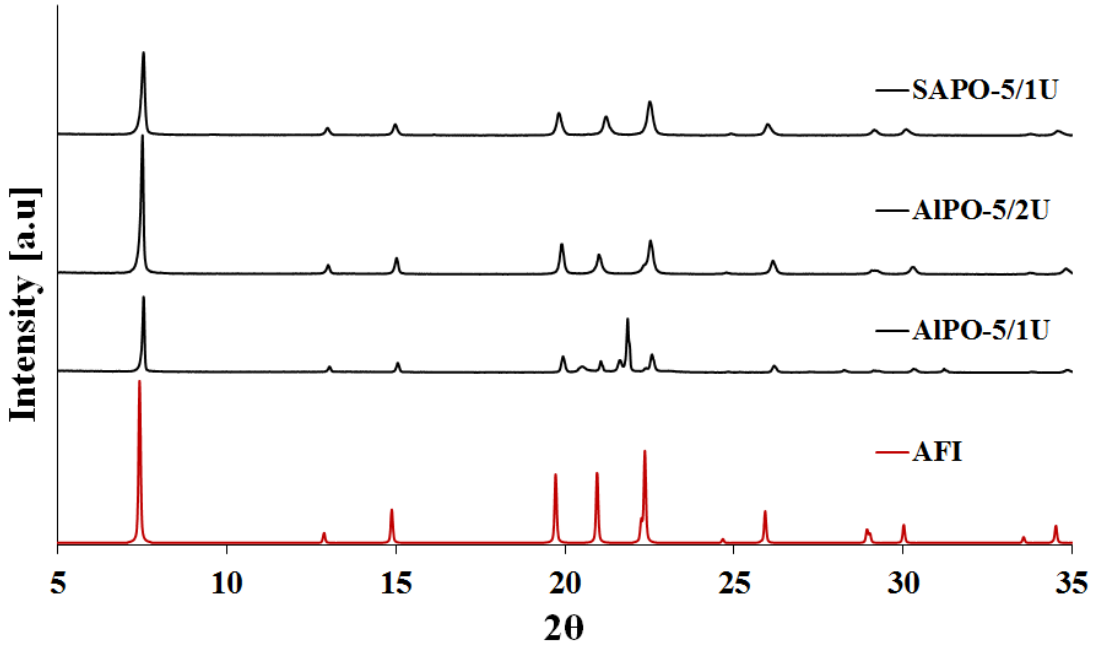

Figure A.4: Diffraction pattern of as-synthesized(U) AlPO-5 and SAPO-5.

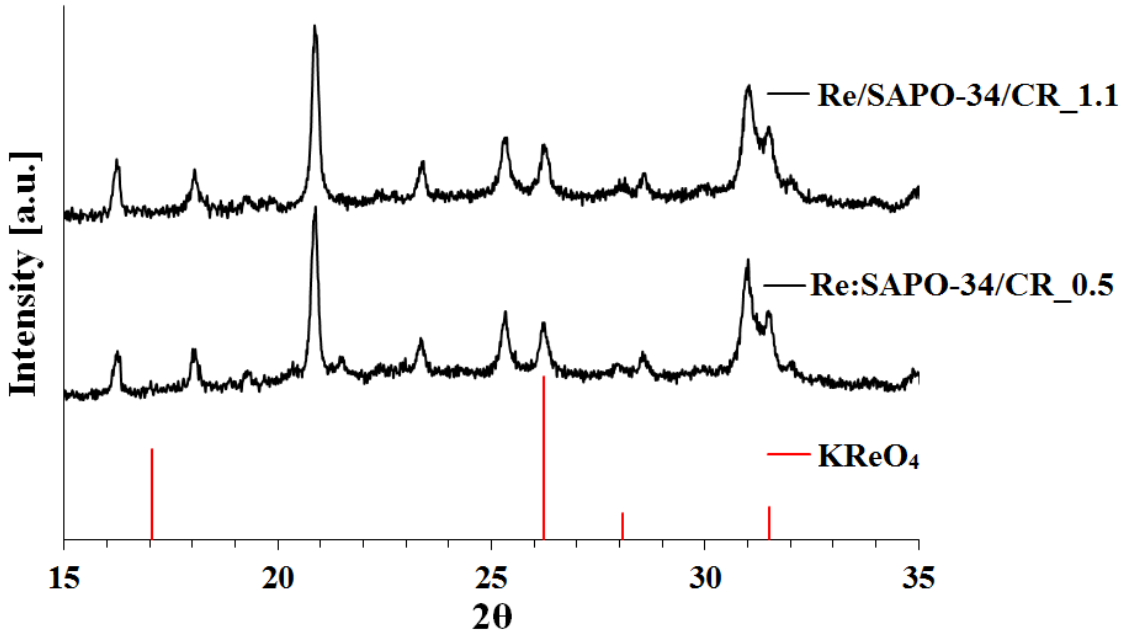

Figure A.5: XRD diffractogram of samples that were calcined followed by reduction, with the four most intense $KReO_4$ peaks in this range. [46] A blue asterisk indicate a peak that arises due to the $KReO_4$.

B Surface area measurements

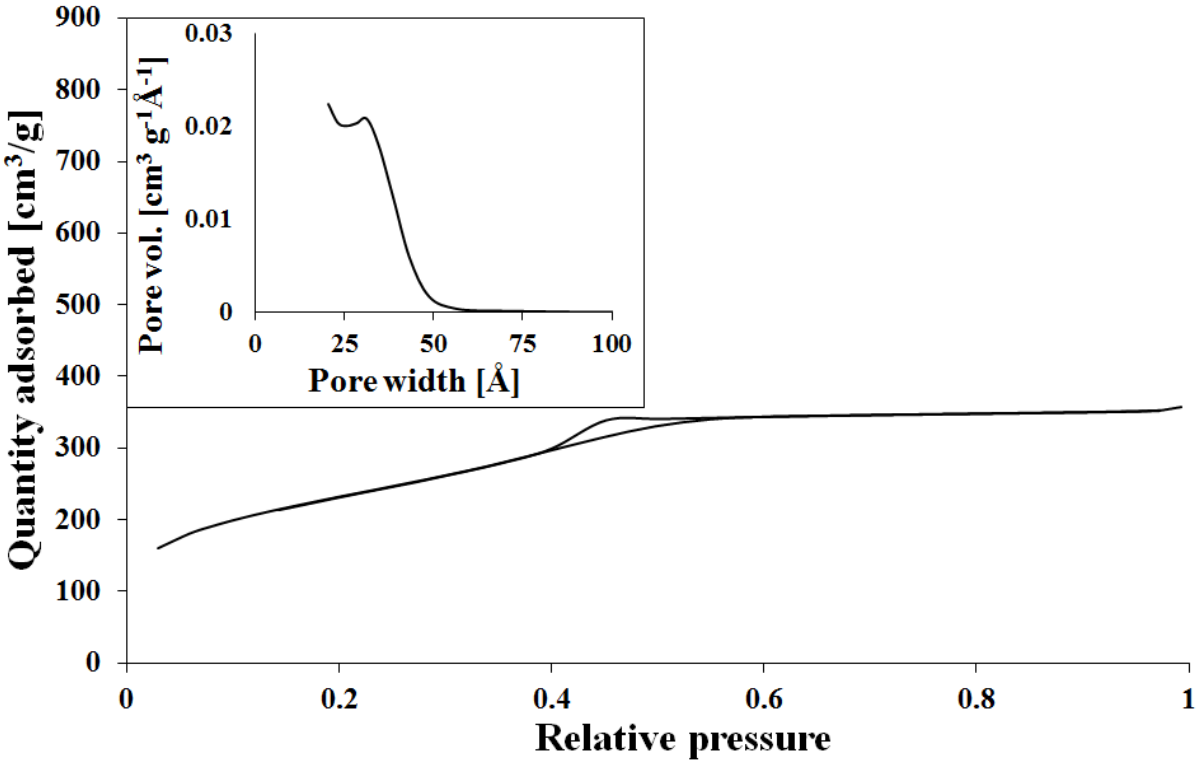

Figure B.1: BET isotherm and pore distribution from BJH of SBA-15/100.

C ICP-MS

Table C.1: Elemental composition after ion-exchange in 0.1 M Re-solution with 0.3 g as-synthesized and calcined SAPO-34/2.

Support	Al [wt.%]	P [wt.%]	Si [wt.%]	Re
SAPO-34/2 as-synthesized	18.6	16.5	5.3	0.004
SAPO-34/2 calcined	18.0	15.5	5.1	0.010

Table C.2: Elemental composition after SAPO-34/2 and SBA-15/140 had been partially calcined at different temperatures and ion-exchanged with 0.03 M Re solution. The SAPO-34/2 samples were calcined for 6 hours at 550 °C to completely remove SDAs before elemental composition analysis.

Support	Partial calcination temperature [°C]	Al [wt.%]	P [wt.%]	Si [wt.%]	Re [wt.%]
SAPO-34/2	200	18.6	16.4	4.0	0.002
SAPO-34/2	300	17.5	15.8	4.2	0.001
SAPO-34/2	400	17.2	15.2	4.0	0.001
SAPO-34/2	500	17.4	15.4	4.1	0.002
SBA-15/140	350	0.00	0.00	44	0.001

Table C.3: Elemental composition after 0.3 g calcined SAPO-34/2 had been added to 20 mL of a specified concentration of ethanol or acetone solution, and stirred for 1 or 2 days.

Solvent	[Re] [mol/L]	Ion-exchange duration [days]	Al [wt.%]	P [wt.%]	Si [wt.%]	Re [wt.%]
Ethanol	0.01	1	16.2	14.8	3.2	0.1
Ethanol	0.01	2	16.5	15.3	3.6	0.1
Ethanol	0.10	2	14.3	13.3	2.9	1.9
Acetone	0.01	1	17.3	15.6	3.3	0.1
Acetone	0.01	2	16.3	15.0	3.2	0.1
Acetone	0.10	2	15.3	13.9	3.1	0.1

Table C.4: Elemental composition after ion-exchange in 20 mL 0.1 M Re ethanol solution, with 0.3 g of various support materials. The ion-exchange duration was 1 or 2 days.

Support	Ion-exchange duration [days]	Al [wt.%]	P [wt.%]	Si [wt.%]	Re [wt.%]
AlPO-34HF	1	16.3	20.4	0.1	0.00
AlPO-34HF	2	19.2	24.0	0.6	0.07
SAPO-5/1	1	18.3	21.2	2.4	0.09
SAPO-5/1	2	17.7	20.8	2.2	0.16
AlPO-5/2	1	16.4	21.4	0.0	0.19
AlPO-5/2	2	16.7	21.0	0.0	0.08
SBA-15/140	1	0.00	0.00	44.6	0.05
SBA-15/140	2	0.00	0.00	40.4	0.01

Table C.5: Elemental composition of samples with names containing information of introduction method, heat treatment and resulting rhenium loading.

Sample	Al [wt.%]	P [wt.%]	Si [wt.%]	Re [wt.%]
Re:SAPO-34/AP_1.9	14.3	13.3	3.0	1.9
Re:SAPO-34/R_3.0	16.7	16.9	4.7	3.0
Re:SAPO-34/C_0.5	15.7	14.6	3.5	0.5
Re:SAPO-34/CR_0.5	17.6	16.4	6.6	0.5
Re/SAPO-34/AP_2.6	18.1	16.2	3.9	2.6
Re/SAPO-34/R_2.8	18.6	16.9	6.6	2.8
Re/SAPO-34/C_1.0	16.9	15.2	3.6	1.0
Re/SAPO-34/CR_1.1	18.3	16.5	4.6	1.1
Re/SAPO-5/AP_2.3	21.2	22.8	2.2	2.3
Re/SAPO-5/R_2.1	20.4	22.1	4.8	2.1
Re/SAPO-5/C_0.2	19.6	21.3	2.0	0.2
Re/SBA-15/AP_2.7	48.3	0.0	0.0	2.7
Re/SBA-15/R_2.2	45.3	0.0	0.0	2.2
Re/SBA-15/C_0.0	50.1	0.0	0.0	0.0

D EXAFS refinements

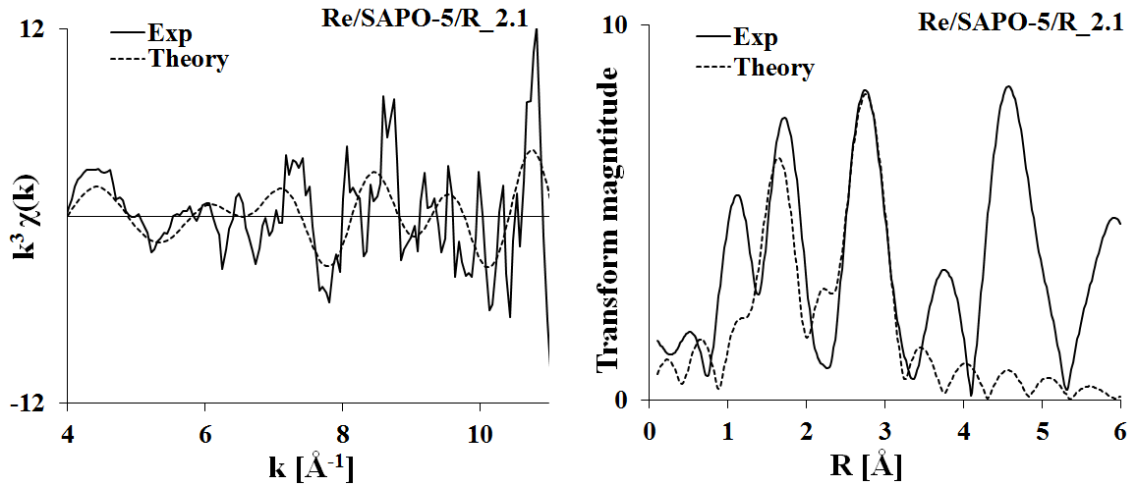

Figure D.1: EXAFS refinements for incipient wetness and reduced SAPO-5, Re/SAPO-5/R_2.1, in k-space (k^3-weighting) and R-space.

Table D.1: EXAFS refinements for Re/SAPO-5/R_2.1. The type of scatter, multiplicity, interatomic distance, Debye-Waller factor, shift in E_0, k-range and goodness of fit, R[%]. The AFAC value was fixed at 0.80.

Sample	Scatterer	N	R[Å]	$2\sigma^2$[Å^2]	ΔE_0[eV]	Δk[Å^{-1}]	R[%]
Re/SAPO-5/R_2.1	Re	2(2)	2.71(4)	0.004(4)	-8(8)	4-11	83
	O	1(1)	1.80(4)	0.03(3)			